energies

MDPI

Article

Core-Scale Experimental Evaluation of Low-Salinity Waterflooding, AOS Surfactant Flooding and N_2-WAG for Controlling Capillary Hysteresis and Enhancing Oil Displacement in Porous Media

Inglab Aliyev [1], Bayram Gasimov [1], Nargiz Akhundova [1,*] and Raikhan Suleimenova [2]

[1] Department of Oil and Gas Engineering, Azerbaijan State Oil and Industry University, Azadliq Avenue, Baku AZ1010, Azerbaijan; inqilab.aliyev@asoiu.edu.az (I.A.); gasimov.bayram.gb@gmail.com (B.G.)
[2] Faculty of Oil and Gas, Atyrau University of Oil and Gas Named After Safi Utebayev, Baimukhanov st., 45a, Atyrau 060027, Kazakhstan; raikhan.suleimenova@aogu.edu.kz
* Correspondence: nargiz.axundova@asoiu.edu.az; Tel.: +994-555157013

Abstract

Capillary hysteresis significantly affects oil displacement efficiency in porous media by influencing residual oil trapping, relative permeability scanning behavior, and saturation history-dependent flow resistance. This paper evaluates core-scale EOR strategies designed to influence capillary trapping and saturation-history-dependent displacement behavior, with the aim of increasing displacement efficiency using sandstone core samples representing seven parent-core materials. Reservoir conditions were simulated through conventional high-salinity brine flooding, low-salinity waterflooding (LSWF), chemical EOR using alpha olefin sulfonate (AOS) surfactant, and low-salinity water-alternating-gas (WAG) flooding with nitrogen. After LSWF, separate batches of core samples were retrieved from the remaining material of the respective parent cores C1 to C7. Thus, the CEOR and N_2-WAG operations were conducted on different core samples that were separately processed and initialized. HSWF recovered an average of 53.15 ± 5.42% of OOIP at 56,300 ppm salinity and left a residual oil saturation of 34.57 ± 2.99% pore volume (PV). Among the brines examined, 7600 ppm provided the highest recovery of 61.31 ± 5.69% OOIP and left a residual oil saturation of 28.52 ± 3.36% PV. With further dilution of the brine solutions, performance decreased to 54.50 ± 5.96% OOIP recovery at 3000 ppm and 49.00 ± 6.24% OOIP at 1000 ppm. Further tests showed even worse results due to increasing solid content in the effluent, permeability impairment, and swelling of cores. Volume-weighted mean effluent solids content was 13.99 mg/L at 7600 ppm, 95.01 mg/L at 3000 ppm, and 225.00 mg/L at 1000 ppm. Micro-CT imaging of C1 for 3000 ppm pre- and post-flood cores indicated localized restriction of the resolved pore space. These results show that swelling and migration of fines contributed to the adverse responses at the lowest salinity. In contrast, a 0.5 wt% AOS formulation on a commercial-product basis (0.195 wt% active AOS) recovered 69.30 ± 6.32% OOIP with a residual oil saturation of 22.60 ± 4.00% PV, while N_2-WAG recovered 73.06 ± 6.23% OOIP with a residual oil saturation of 19.82 ± 4.01% PV. Consequently, the overall outcomes correlate with less residual trapping and better displacement under salinity control, interfacial-tension reduction, and cyclic gas–water saturation changes.

Keywords: capillary hysteresis; low-salinity waterflooding; AOS surfactant; chemical EOR; WAG; residual oil saturation; sandstone; relative permeability

Check for updates

Academic Editor: Dameng Liu

Received: 28 August 2026
Revised: 8 October 2026
Accepted: 9 October 2026
Published: 26 October 2026

Copyright: © 2026 by the authors. Licensee MDPI, Basel, Switzerland. This article is an open access article distributed under the terms and conditions of the Creative Commons Attribution (CC BY) license.

1. Introduction

Oil displacement in porous rocks is not only driven by pressure gradients and fluid mobility but also depends significantly on the rock–fluid saturation history [1–4]. Capillary forces define the distribution, connectivity, and trapping of the non-wetting oil phase during drainage and imbibition in porous media [1,2]. Therefore, the values of residual oil saturation, relative permeability, capillary pressure, and mobility are not one-to-one functions of saturation; these quantities depend heavily on the saturation history as well [1,3,4]. This so-called "capillary hysteresis" is characterized by the differences between the drainage, imbibition, and scanning curves [1,4,5]. For reservoir engineering applications, the effect of capillary hysteresis directly impacts residual oil trapping, water-cut production, gas trapping, sweep efficiency, and the prediction of recoverable oil in secondary or enhanced oil recovery (EOR) scenarios [3,5,6]. Conventional waterflooding remains the most widely applied method for secondary recovery due to its operational simplicity and favorable economics [7,8]. In porous media, however, high-salinity waterflooding can cause a significant amount of residual oil to be trapped by capillary forces after the passage of the primary displacement front. Residual oil is commonly held as disconnected ganglia, films, and pore clusters, depending on pore-throat geometry, wettability, interfacial tension, and saturation history [1–4]. Under these circumstances, additional water injection does not result in considerable incremental oil and mostly leads to an unfavorable increase in water production [7,8]. Therefore, improving oil recovery from sandstone reservoirs requires the application of techniques capable of reducing capillary trapping, modifying wettability, improving microscopic displacement, or altering the saturation history to mobilize the remaining oil after conventional waterflooding [8–14]. Salinity reduction in clay-bearing sandstone systems is known to affect surface charge, ion exchange, electric double layer dynamics, and shift wettability toward more favorable conditions. These factors can collectively help reduce capillary trapping and improve oil displacement. Nevertheless, the effect of salinity reduction is not necessarily monotonic. Excessive salinity reduction can lead to the destabilization of clay minerals, fines migration, an increased pressure drop, and a decrease in effective permeability. Therefore, the major challenge in low-salinity waterflooding (LSWF) is not merely to achieve the lowest possible salinity, but to determine the best-performing salinity among those tested that yields maximum oil displacement while minimizing clay-related impairment [8–11]. In addition, surfactant-assisted chemical enhanced oil recovery offers another way to alleviate the capillary trapping effects in porous media [12–16]. This reflects a more general principle of reservoir fluid injection, namely that the in situ performance of an injected fluid depends on the deliberate design of its properties, as also demonstrated for CO_2-based fracturing fluids, in which fluid rheology and fluid–particle interactions govern particle settling, sedimentation, and fracturing capacity. Surfactants can adsorb on the oil–water interface and lower the interfacial tension, which in turn increases the capillary number and facilitates the deformation, reconnection and mobilization of the disconnected oil ganglia left after the waterflooding process [12–16]. In order to explore the application of AOS for the sandstone EOR process, the interfacial activity and the compatibility of AOS with properly designed injection brines have been investigated. However, it is also important to note that the concentration of the surfactant must be carefully controlled. If the surfactant concentration is insufficient, the interfacial effects required for effective residual-oil mobilization may not be fully developed, which can limit displacement efficiency and oil recovery [12–18]. On the other hand, if the surfactant concentration is too high, it may result in high chemical consumption, higher adsorption and retention of the surfactant, higher flow resistance due to emulsion formation and possible injectivity problems. In order to properly characterize the performance of the chemical EOR processes, we use factors such as recovery factor, residual oil saturation,

pressure response and displacement dynamics to determine the best-performing operating condition among those tested rather than the surfactant concentration itself [12–16]. The Water-Alternating-Gas (WAG) method serves as another effective tool for modifying saturation-history-dependent displacement behavior by actively altering the saturation history of the gas and water phases. Cyclic injection of water and gas slugs results in alternating drainage and imbibition cycles, modifying three-phase relative permeability, entrapping part of the gas phase, and increasing contact between bypassed oil and the gas slug. N_2-WAG is particularly attractive when nitrogen is readily available and can improve sweep efficiency without a strict requirement for miscibility. Combining low-salinity brine injection with nitrogen injection allows for simultaneous modifications of rock–brine–oil interactions and saturation history, a process termed low-salinity N_2-WAG. Hence, WAG can influence capillary-hysteresis-related displacement behavior through deliberate alteration of the saturation history [5,6,19–22]. While there is a vast body of literature on waterflooding, low-salinity waterflooding, surfactant flooding, and WAG, relatively few comparative investigations have evaluated these methods within a shared experimental context using separate core specimens. A comparative analysis of different mechanisms of residual oil entrapment and saturation history dependence is crucial in the study of capillary hysteresis, since each EOR method targets a specific aspect: LSWF modifies rock–brine–oil interactions, surfactant flooding lowers interfacial tension and capillary trapping, while N_2-WAG induces saturation history changes and three-phase flow hysteresis. The main aim of this work is the experimental evaluation and comparison of multi-mechanism EOR treatments used to investigate capillary-hysteresis-related displacement effects and improve oil displacement in sandstone cores. The experimental program evaluated sandstone core samples under representative reservoir conditions using: (a) high-salinity waterflood, (b) low-salinity waterflood, (c) AOS-enhanced chemical EOR, and (d) low-salinity N_2-WAG [23–28]. This research compares HSWF, LSWF, AOS-assisted CEOR, and N_2-WAG by implementing all of them within a common coreflood framework. All methods were evaluated in separate experiments. For the CEOR and N_2-WAG programs conducted after the LSWF study, additional core samples were taken from the remaining material of the relevant parent cores C1–C7. Specimens were allocated separately to the two programs and prepared as described in Section 2.4. The aims are: (i) to determine the best-performing salinity and AOS concentration, (ii) to compare the results of flooding at 2.0 pore volumes (PV), (iii) to analyze the adverse low-salinity response using effluent-solids analysis, permeability sensitivity, swelling tests, and micro-CT images, and (iv) to determine the recovery response achieved via the cyclic injection of low-salinity WAG with nitrogen. The overall analysis of the treatment is focused on the efficiency of displacement and compatibility with evidence related to changes in capillary trapping, whereas the separate P_c-S_w drainage-imbibition directly demonstrates path-dependent capillary-pressure behavior in the representative C1-parent rock–fluid system. The experimental program investigated recovery efficiency, residual oil saturation, pressure behavior, water cut, saturation-history-dependent displacement responses, and normalized phase-flow behavior. The novelty of this project lies in the direct experimental comparison of these three approaches—salinity control, interfacial tension reduction, and cyclic gas–water saturation changes—within a common experimental framework rather than as isolated EOR techniques for capillary hysteresis management [29–31].

These treatment effects are analyzed in terms of treatment-dependent displacement responses and as data that are consistent with changes in capillary trapping and saturation history effects. Furthermore, direct capillary-pressure hysteresis was assessed for one C1-parent sample using a $P_c - S_w$ curve obtained via a scanning path generated through a

reverse method. This test is not a comprehensive set of hysteresis curves of P_c or relative permeability for any of the parent cores or any EOR treatment applied to them [32–34].

2. Materials and Methods

2.1. Core Samples and Petrophysical Properties

The original sandstone specimen set had seven core samples denoted by C1–C7 with absolute permeabilities between 95 and 380 mD and effective porosities between 17.8 and 22.2%. The nominal dimensions of the core samples were 2 inches in diameter and 12 inches in length, resulting in a bulk volume of 617.78 cm^3. Table 1 summarizes information on the porosity, effective porosity, absolute permeability, pore volume, initial water saturation, initial oil saturation, and geological designations of the original C1–C7 samples. For the experimental programs carried out after the LSWF process, new cores of similar nominal dimensions were extracted from the rest of the material left from the corresponding C1–C7 core samples. To distinguish these fresh cuts from the original cores, the samples are denoted as C1-AOS–C7-AOS and C1-WAG–C7-WAG, whereby C1-AOS and C1-WAG are from the same parent core as C1, C2-AOS and C2-WAG are from the same parent core as C2, and so on through to C7-AOS and C7-WAG. The C1-AOS–C7-AOS and C1-WAG–C7-WAG samples were new physical cores and therefore went through an individual characterization before being used for the experiment. The petrophysical properties of the C1-AOS–C7-AOS and C1-WAG–C7-WAG cores were similar to those of the corresponding C1–C7 samples. The new cores were then prepared as indicated in Section 2.4 before using them in the post-LSWF experimental programs. Because the measured petrophysical properties of the freshly prepared C1-AOS–C7-AOS and C1-WAG–C7-WAG specimens were similar to those of the corresponding original C1–C7 specimens, Table 1 reports the properties of the original set to avoid redundant presentation.

Table 1. The original C1–C7 sandstone core samples' initial saturation conditions and petrophysical characteristics.

Core ID	k, mD	φ, %	φ_e, %	PV (cm^3)	S_{wi}, %	S_{oi}, %	Zone
C1	320	22.0	21.5	132.82	24.0	76.0	Bal. X
C2	180	18.5	17.8	109.96	27.0	73.0	Per. B
C3	95	20.0	19.0	117.38	29.0	71.0	Bal. IX
C4	110	20.5	20.0	123.56	28.0	72.0	Bal. IX
C5	210	19.0	18.3	113.05	26.0	74.0	Per. B
C6	380	23.0	22.2	137.15	23.0	77.0	Bal. X
C7	270	21.0	20.1	124.17	25.0	75.0	Per. D

The effect of these parameters on recovery factors, pressure response, capillary trapping, residual oil saturation, and normalized phase-flow indices was evaluated through different EOR methods.

2.2. Fluids, Brines, Surfactant, and Gas

The crude oil had an API gravity of 35 and a viscosity of 0.69 cP under the experimental pressure and temperature conditions. Synthetic brines with variable total dissolved solids (TDS) concentrations were used for the aqueous phase. Base case high-salinity waterflood experiments were conducted with a brine salinity of 56,300 ppm, which is representative of a typical high-salinity formation brine. Low-salinity brines were prepared by decreasing

brine salinity in steps to study the oil recovery, residual oil saturation and pressure changes as a function of salinity.

The mineral composition observed in the previous laboratory study on the sandstone core samples, along with the possible implications for low-salinity response, clay or fines sensitivity, wettability alteration, and mineral/brine interactions, is shown in Table 2. The mineralogy provided in the above report is only qualitative information that does not represent the amounts of these minerals. Clay minerals, which include illite/mica, illite-smectite, chlorite, and kaolinite, could affect ion exchange properties, surface charge, wettability, swelling, and fines mobility in low-salinity floods. However, the presence of these minerals alone does not necessarily indicate the dominant mechanism involved in a particular flooding experiment.

Table 2. Rock mineralogy and relevance to low-salinity and capillary-hysteresis behavior.

Mineral Name	Chemical Formula	Related Ions	Relevance to LSWF and Hysteresis Behavior
Quartz	SiO_2	Si^{4+}, O^{2-}	Surface charge and wettability behavior.
Feldspar	$KAlSi_3O_8$, $aAlSi_3O_8$, $CaAl_2Si_2O_8$	K^+, Na^+, Ca^{2+}, Al^{3+}	Ion exchange and surface-charge modification.
Illite/mica	$KAl_2(AlSi_3O_{10})(OH)_2$	K^+, Al^{3+}, Si^{4+}	Wettability alteration and fines sensitivity.
Illite–smectite	Mixed-layer (I/S) clay	Na^+, Ca^{2+}, Mg^{2+}, K^+	Swelling or fines migration.
Chlorite	$(Mg,Fe,Al)_6(Si,Al)_4O_{10}(OH)_8$	Mg^{2+}, Fe^{2+}, Fe^{3+}, Al^{3+}	Brine compatibility and pressure response.
Kaolinite	$Al_2\ Si_2\ O_5\ (OH)_4$	Al^{3+}, Si^{4+}	Fines migration under LS brine conditions.
Calcite	$CaCO_3$	Ca^{2+}, CO_3^{2-}	Divalent-ion exchange and brine compatibility.
Dolomite	$CaMg(CO_3)_2$	Ca^{2+}, Mg^{2+}, CO_3^{2-}	Ca/Mg surface reactions.
Siderite	$FeCO_3$	Fe^{2+}, CO_3^{2-}	Iron-related brine reactions.
Halite	NaCl	Na^+, Cl^-	Ionic strength of formation brine.

Synthetic brines were prepared by dissolving NaCl, KCl, $CaCl_2$, $MgCl_2$, Na_2SO_4, and $NaHCO_3$ in deionized water. The salinities used were 56,300; 28,700; 15,000; 10,000; 7600; 5000; 3000; and 1000 ppm, with salinities being stated nominally in terms of total dissolved salts (TDS) in mg/L. Brines of 56,300 and 28,700 ppm were prepared using the salt compositions given, and the 28,700 ppm brine was used as the stock brine in order to make brines of lower salinities through proportional dilution with deionized water. To prepare 1 L of 15,000, 10,000, 7600, 5000, 3000, and 1000 ppm brines, about 520, 350, 265, 175, 105, and 35 mL of the 28,700 ppm mother brine were mixed with deionized water to yield 1 L. This dilution process was based on the principle $C_1V_1 = C_2V_2$, with some small variations from the desired concentrations due to practical volumetric differences. The final TDS was determined using a conductivity/TDS meter before injection. Nominal salt compositions and the brine preparation procedure are summarized in Table 3. After screening for salinity effects, 7600 ppm was chosen as the best-performing low-salinity condition of all the salinities examined. This brine was used as the carrier brine in the AOS formulation and as the aqueous phase in the nitrogen water-alternating-gas (N_2-WAG) process.

Table 3. Nominal salt formulations, experimental roles, and purposes of the synthetic brine series.

TDS (ppm)	NaCl, g/L	KCl, g/L	$CaCl_2$, g/L	$MgCl_2$, g/L	Na_2SO_4, g/L	$NaHCO_3$, g/L	Experimental Role	Purpose
56,300	47.08	0.98	2.94	2.94	1.96	0.39	Baseline high-salinity brine	Reference HSWF condition
28,700	24.00	0.50	1.50	1.50	1.00	0.20	Intermediate-salinity brine	Intermediate-salinity comparison
15,000	12.50	0.26	0.78	0.78	0.50	0.10	Intermediate low-salinity brine	Evaluate response to moderate salinity reduction
10,000	8.40	0.17	0.50	0.50	0.34	0.07	Low-salinity brine	Evaluate response to further salinity reduction
7600	6.35	0.13	0.40	0.40	0.26	0.05	Best-performing low-salinity brine among those tested	Selected as carrier brine for AOS formulations and aqueous phase for N_2-WAG
5000	4.20	0.08	0.26	0.26	0.17	0.04	Lower-salinity brine	Evaluate the effect of further dilution below 7600 ppm
3000	2.50	0.05	0.16	0.16	0.11	0.02	Very-low-salinity brine	Evaluate recovery, pressure response, and clay/fines sensitivity
1000	0.80	0.02	0.05	0.05	0.04	0.01	Very-low-salinity endpoint	Evaluate response under the strongest dilution condition tested

The AOS utilized in this study is BIO-TERGE® AS-40 (Stepan Company Northbrook, IL, USA), an aqueous solution of Sodium C14–16 Olefin Sulfonate with 39 wt% of active ingredient. Unless otherwise stated, the nominal AOS concentrations reported in the coreflood program refer to the commercial product as received; therefore, 0.3, 0.5, and 1.0 wt% commercial product correspond to 0.117, 0.195, and 0.390 wt% active AOS, respectively. Independent air–solution surface-tension measurements in the 7600 ppm carrier brine at 70 °C gave a CMC breakpoint of 0.044 wt% on a commercial-product basis, equivalent to 0.017 wt% active AOS. The coreflood concentrations were therefore above the measured CMC, while 0.5 wt% is retained as the best-performing tested operating concentration because its selection was based on recovery, residual oil saturation, and pressure response rather than CMC alone.

Surface-Tension Measurement and CMC Determination

Surface tension of BIO-TERGE® AS-40 solutions prepared in 7600 ppm multicomponent brine was measured at 70 ± 0.2 °C using a KRÜSS Tensíío force tensiometer (KRÜSS Scientific, Hamburg, Germany) equipped with a KRÜSS PL01 standard platinum Wilhelmy plate and controlled with KRÜSS ADVANCE software (https://www.kruss-scientific.com/en/products-services/advance-software; accessed on 12 October 2026). Concentrations of commercial product in the range of 0, 0.0025, 0.005, 0.010, 0.020, 0.030, 0.050, 0.075, 0.100, 0.200, 0.300, 0.500, and 1.000 wt% were measured three times. Solutions were aged for 12 h after preparation, sonicated for 30 min, allowed to rest for 2 h, and equilibrated for 20–30 min at the measurement temperature. A reading was considered stabilized if a change in surface tension did not exceed 0.1 mN/m during a 5 min period. The critical micelle concentration (CMC) was determined from the intersection of linear fits of surface tension dependence on $\log_{10}$ (commercial product concentration) in the descending and plateau regions of 0.005–0.030 and 0.050–0.300 wt%, respectively.

2.3. Experimental Setup and Conditions

High-pressure coreflooding equipment was used for conducting this study. The equipment comprised injection pumps, fluid reservoirs, a core holder, pressure sensors,

fluid collection devices, a backpressure regulator, and a data acquisition system. Figure 1 illustrates the experimental procedure for the HSWF, LSWF, AOS-assisted CEOR, and N_2-WAG processes [13,15,19–21].

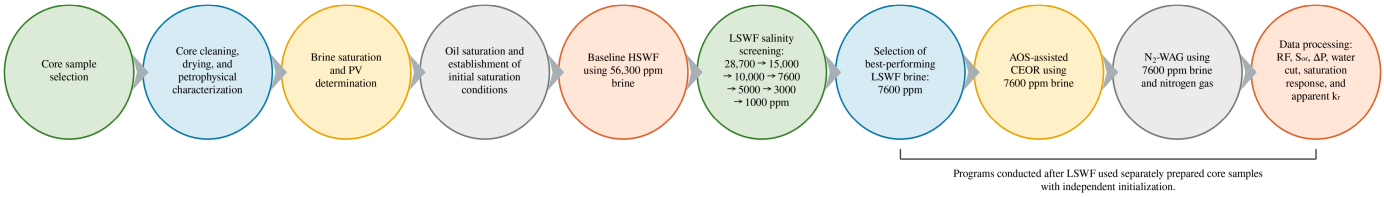


Figure 1. Experimental workflow for core-scale evaluation of high-salinity waterflooding, low-salinity waterflooding, AOS-assisted chemical EOR, and N_2-WAG programs.

The core samples were kept in the core holder and subjected to pressure and temperature conditions typical of the reservoir. The confining pressure was 5000 psi, and the backpressure was 4000 psi, while the temperature was set to 70 °C. In the primary HSWF, LSWF, AOS-assisted CEOR, and liquid WAG processes, an injection rate of 0.30 mL/min as used as a standard injection rate for comparative purposes based on recovery efficiency, residual oil saturation, differential pressure, and water cut. Rate-sensitivity tests described in Section 2.8 were conducted at 0.15, 0.30, and 0.60 mL/min.

2.4. Core Preparation and Initial Saturation Procedure

A matched-parent-core, independently initialized experimental scheme was employed. The original sandstone core samples were named C1 to C7. For the experimental work done after the LSWF research, other core samples of the same nominal size were cut from the remainder of the respective C1 to C7 core samples and were referred to as C1-AOS–C7-AOS and C1-WAG–C7-WAG. Each newly cut core sample was tested only after preparing it and bringing it to the required saturation state. HSWF, individual LSWF salinities, AOS-assisted CEOR concentrations, and N_2-WAG were not implemented in a cumulative manner within a single continuous flooding experiment. Thus, all treatment comparisons were performed on a matched-parent-core basis, while correspondence among C1–C7, C1-AOS–C7-AOS, and C1-WAG–C7-WAG was maintained throughout the experiments.

The core samples which needed preparation for analysis were first cleaned before being subjected to the required experiments through high-pressure washing with sterile water and solvent washing with toluene and methanol. Toluene was used to flush out the remaining crude oil, asphaltenes, and other hydrocarbon species, while methanol was used to flush out the formation-water salts and polar compounds. The total duration of the cleaning process was approximately 36–40 h for each core sample. The cleaned specimens were then dried under controlled conditions at 178–180 °C prior to petrophysical characterization and experimental initialization.

Since the process of solvent cleaning and heating could affect the natural wetting characteristics of clay-bearing sandstone, the samples could not be assumed to retain their natural wetting condition. Therefore, the samples were first subjected to the required initial wettability conditions and then tested for the contact angle using the captive-drop technique. The specimens were saturated with formation brine and put in an optical cell containing formation brine. Then crude oil drops were placed on the rock surface, and the contact angle was measured through the aqueous phase at multiple locations to verify the experimental starting wettability condition before flooding.

Subsequently, porosity and absolute permeability were measured. The core samples were then saturated with the selected brine, and the pore volume was calculated based on the difference in mass between the brine-saturated and dry core masses divided by

the corresponding brine density. Before crude-oil injection, the required core-specific initial water saturation was established, after which the corresponding initial oil saturation was achieved. The characteristics associated with C1–C7 as presented in Table 1 are for the original core set; the new core sets (C1-AOS–C7-AOS and C1-WAG–C7-WAG) were tested independently and showed petrophysical properties very similar to those of the original samples. Only after the core-specific petrophysical properties, wettability condition, and initial fluid saturations had been verified was the displacement test started. The entire experimental program took roughly nine months because specimen preparation and characterization included cleaning where necessary, controlled drying, petrophysical property measurement, wetting behavior evaluation, brine saturation, and establishment of the required water and oil saturations.

2.5. Displacement Experimental Program

The experimental program included four coreflood programs: baseline high-salinity waterflooding, low-salinity waterflooding, AOS-assisted chemical EOR and WAG. The purpose of these experiments was to investigate different techniques for controlling the capillary hysteresis effect and reducing the residual oil saturation in the sandstone cores. The entire experimental scheme is presented in Table 4.

Table 4. Experimental matrix for the HSWF, LSWF, CEOR, and WAG coreflooding tests.

Method	Injected Fluid/Process	Salinity/ Concentration	Injection Mode	Main Purpose	Measured Outputs
HSWF	High-salinity brine	56,300 ppm	Continuous brine injection	Baseline recovery and residual trapping	RF, S_{or}, ΔP, water cut, saturation response, normalized phase-flow indices
LSWF	Low-salinity brine	28,700; 15,000; 10,000; 7600; 5000; 3000; 1000 ppm	Continuous brine injection	Best-performing salinity and recovery response	RF, S_{or}, ΔP, water cut, best-performing salinity
CEOR	AOS surfactant and 7600 ppm best-performing low-salinity brine	0.3, 0.5, and 1.0 wt% AOS in 7600 ppm brine	Surfactant flooding followed by low-salinity brine chase	Surfactant-assisted displacement, reduction of capillary resistance, and oil mobilization	RF, S_{or}, ΔP, water cut, normalized phase-flow indices
WAG	Alternating 7600 ppm brine and nitrogen gas	7600 ppm brine + nitrogen gas	Cyclic water/gas injection: four cycles of 0.20 PV N_2 + 0.20 PV brine, followed by a 0.40 PV brine chase	Evaluate cyclic gas–brine saturation changes and saturation-history-dependent displacement behavior.	RF per cycle, cumulative RF, S_{or}, ΔP, water cut, cycle response

Note: For N_2-WAG, the slug volumes, the 1:1 gas-to-brine ratio, and the injection rate of 0.30 mL/min refer to in situ volumes at the test conditions (70 °C, approximately 4000 psi); the corresponding N_2 mass and standard-condition equivalents are given in Section 2.5.4.

For complete experimental traceability, the seven cores were assigned the permanent codes C1–C7.

2.5.1. Baseline High-Salinity Waterflooding

The baseline displacement test used 56,300 ppm high-salinity brine, injected into the core at a fixed rate of 0.30 mL/min to 2.0 PV. Produced oil and water volumes were recorded as a function of injected pore volume. Differential pressure during the injection process was monitored. The results of the baseline high-salinity waterflooding served as the reference point for between-test comparisons of recovery factor, residual oil saturation, pressure response, and water-cut behavior.

2.5.2. Screening of Low-Salinity Waterflooding

Low-salinity waterflooding tests were conducted with brines of decreasing salinity, including 28,700 ppm, 15,000 ppm, 10,000 ppm, 7600 ppm, 5000 ppm, 3000 ppm and 1000 ppm. Each displacement was conducted under identical temperature, pressure and injection rate conditions compared to those of the baseline. For each salinity, recovery factor was calculated from the produced oil volume, residual oil saturation was calculated from the individual initial oil saturation and recovered oil, and water cut and differential pressure were evaluated as functions of injected pore volume. The goal of the screening process was to determine the best-performing brine that would increase the oil recovery with minimal reduction of the injectivity. The best-performing salinity was defined as that providing the maximum recovery factor, minimum residual oil saturation and a stable pressure response.

2.5.3. AOS-Assisted Chemical EOR

The chemical EOR experiments involved an AOS surfactant solution, prepared in a 7600 ppm brine, which was identified as the best-performing low-salinity brine among the tested configurations. Commercial-product concentrations of 0.3, 0.5, and 1.0 wt% BIO-TERGE® AS-40 (39 wt% active matter), corresponding to 0.117, 0.195, and 0.390 wt% active AOS, respectively, were used with the individually prepared C1-AOS–C7-AOS core samples that were independently preconditioned before the tests. The effect of AOS concentration on recovery factor, residual oil saturation, and pressure behavior was investigated. After AOS injection, a chase with the same 7600 ppm low-salinity brine was performed, with comparisons made at 2.0 injected PV. The AOS experiments were aimed at evaluating the effect of the displacement process, enhanced by surfactant, after the completion of the salinity-screening stage. The best AOS concentration was selected from the tested ones based on the overall parameters of recovery factor, residual oil saturation, and pressure behavior.

In the case of the 0.5 wt% AOS treatment, a 0.50 PV surfactant slug prepared in 7600 ppm brine was injected at 0.30 mL/min, followed by a 1.50 PV chase with surfactant-free 7600 ppm brine, giving a total injected volume of 2.00 PV. Duplicate corefloods were also carried out for the 7600 ppm LSWF and 0.5 wt% AOS-assisted CEOR treatments using new core samples that matched the original parent cores. The duplicate experiments were conducted at 70 °C, with 4000 psi backpressure, 5000 psi confining pressure, and a liquid injection rate of 0.30 mL/min. Measured outputs included recovery factor, produced-fluid volumes, water cut, differential pressure, final residual oil saturation, and peak differential pressure.

2.5.4. WAG Injection

N_2-WAG tests were carried out as a separate program using individual C1-WAG to C7-WAG core samples. Each test started from the required initial oil–water saturation state and did not follow HSWF, LSWF, or AOS-assisted CEOR on the same physical core

sample. Each WAG specimen was prepared and characterized according to Section 2.4 before testing.

The WAG tests used alternating injections of nitrogen gas and the 7600 ppm brine identified as the best-performing low-salinity condition among those tested. A single WAG cycle involved injection of 0.20 PV of nitrogen and 0.20 PV of 7600 ppm low-salinity brine, representing a gas-to-brine injected-volume ratio of 1:1 and a total volume of 0.40 PV per cycle. This process was repeated four times, giving a total cyclic injection of 1.60 PV, comprising 0.80 PV nitrogen and 0.80 PV low-salinity brine. After the four WAG cycles, a 0.40 PV chase with the same 7600 ppm brine brought the total injected volume to 2.00 PV in each experiment. Including the final brine chase, the total injected nitrogen-to-brine volume ratio was 0.80:1.20.

For comparative analysis, the first WAG cycle therefore corresponded to a total injected volume of 0.40 PV. Across the complete WAG process, cumulative liquid and N_2 injection amounted to 1.20 and 0.80 PV, respectively. These volumes were used to construct equal-total-PV and equal-liquid-volume comparisons with the waterflood experiments.

The alternating gas–brine system generated drainage- and imbibition-type changes in saturation history, allowing evaluation of their effects on phase connectivity, oil mobilization, and displacement efficiency. Measured outputs included recovered oil and water volumes, outlet-gas response, and differential pressure. Pore volumes in the C1-WAG and C7-WAG samples were similar to those of their parent cores. Based on the individual pore volume of each WAG specimen, 0.20 PV of N_2 or brine corresponded to approximately 21.99–27.43 mL. At an injection rate of 0.30 mL/min, each 0.20 PV slug required approximately 73.3–91.4 min.

The N_2 slug volumes and the N_2 injection rate are expressed at the test conditions. N_2 was displaced from a transfer vessel located in the oven at the test temperature of 70 °C and pressurized to the injection pressure (approximately 4000 psi). Therefore, the slug volumes of 21.99–27.43 mL given above are in situ gas volumes, the 1:1 gas-to-brine ratio refers to in situ volumes, and the gas injection rate of 0.30 mL/min corresponds to the same in situ superficial velocity as that of the brine slugs (2.47×10^{-6} m/s). At 70 °C and approximately 4000 psi, the density of N_2 is approximately 239 kg/m^3 (compressibility factor of approximately 1.14) and its viscosity is approximately 0.026 cP, as calculated from the reference equation of state [35] and the viscosity correlation [36] for nitrogen. Accordingly, each 0.20 PV N_2 slug contained approximately 5.2–6.6 g of N_2, equivalent to approximately 4.4–5.5 L at standard conditions (101.325 kPa, 15.6 °C), and the in situ injection rate of 0.30 mL/min corresponded to a mass rate of approximately 0.072 g/min, or approximately 60 standard mL/min. The total of 0.80 PV of N_2 injected over the four cycles therefore corresponded to approximately 21–26 g of N_2, or approximately 17.7–22.1 L at standard conditions, per experiment.

Alternating N_2 and brine created repeated drainage- and imbibition-type saturation changes and a three-phase displacement history in which phase occupancy, trapping, and connectivity depended on the preceding saturation path. The WAG coreflood experiment was evaluated by measuring recovery, differential pressure, produced fluid, and outlet gas. Direct capillary-pressure hysteresis was determined in a separate drainage–imbibition experiment (Section 3.7). Thus, the WAG findings provide evidence of saturation-history-dependent three-phase flow behavior and are supported by the independently obtained $\boldsymbol{P_c - S_w}$ hysteresis data.

2.5.5. Additional Confirmation Experiments

Further confirmatory experiments were carried out to provide additional insights into the detrimental displacement effect that appeared when the salinity of the brine was

lower than the best-performing 7600 ppm condition. Confirmatory experiments focused on measuring produced solids and changes in the resolved pore volume. Measurements of effluent solids were made for the 7600, 3000, and 1000 ppm cases, while representative core sample C1 treated with 3000 ppm brine flooding was analyzed using pre- and post-flood X-ray micro-computed tomography (micro-CT). These confirmatory measurements were not part of the salinity screening test protocol and provided additional support for interpreting the increased pressure response and decreased oil production effect caused by low salinity conditions.

Gravimetric Effluent-Solids Analysis

Effluent solid content was measured for brines containing 7600, 3000, and 1000 ppm salt concentration. In each confirmation test, effluent samples were gathered as twenty sequential fractions, each consisting of 0.10 pore volume (PV) of injected volume within a 0–2.0 PV interval. Each fraction was processed separately without any mixing. Free oil was separated, and the volume of the aqueous effluent fraction was measured.

The aqueous phase was filtered through pre-weighed 47 mm hydrophilic polyethersulfone (PES) filters with a nominal pore size of 0.22 µm. The filter cake was washed with three small portions of deionized water to reduce the effects of dissolved salts. The filters were dried at 103–105 °C to constant weight in a drying oven, placed in a desiccator, and reweighed on the Sartorius Cubis III CUB66S-1S0-IC semi-micro balance. Oil-contaminated filters were not used for solids determination.

Every single filter had a mass of about 100 mg before being used. A blank correction of 0.030 mg was applied to every single filter. The blank-corrected mass of solid retained in filter j was calculated as:

$$M_{net,j} = (m_{final,j} - m_{initial,j}) - m_{blank}$$

where $M_{net,j}$ is the net retained-solid mass and all masses are expressed in mg. The corresponding solids concentration was calculated from

$$C_j = \frac{1000 \cdot M_{net,j}}{V_{aq,j}}$$

where $V_{aq,j}$ is the filtered aqueous effluent volume in mL and C_j is expressed in mg/L. Cumulative produced solids were obtained by summing $M_{net,j}$ over the collected fractions, whereas the run-level volume-weighted concentration was calculated as:

$$C_{VW} = \frac{1000 \cdot \sum_J M_{net,j}}{\sum_J V_{aq,j}}$$

Therefore, the concentration calculation considered the volume of aqueous effluent and not the injected volume or the total oil and water effluent volume. A total of 420 individual fraction filters were used across the three salinity treatments.

Single-Phase Permeability Confirmation

Permeability sensitivity was investigated by conducting discrete single-phase brine confirmation tests at salinity values of 7600, 3000, and 1000 ppm. This comparison of permeability values prior to and following exposure was conducted for the same brine concentration. Permeability tests were conducted at brine flow rates of 0.15, 0.30, and 0.45 mL/min, while maintaining a temperature of 70 °C, a backpressure of 4000 psi, and a confining pressure of 5000 psi.

Permeability retention was expressed as

$$R_k = \frac{k_f}{k_0}$$

where k_0 and k_f denote the initial and post-exposure permeability values, respectively. Permeability loss was calculated as

$$\textit{Permeability loss}(\%) = 100 \cdot \left(1 - \frac{k_f}{k_0}\right)$$

Linear Swelling Measurements

Linear swelling was measured in rock samples containing clay, which were individually exposed to brine solutions of 7600, 3000, and 1000 ppm for 24 h at 70 °C. In each saline solution, three replicates were analyzed using the dilatometric measurement technique, which utilizes an LVDT sensor with an accuracy of ±0.1 µm. The swelling strain was calculated as:

$$\varepsilon_L = 100 \cdot \frac{L_f - L_0}{L_0}$$

where L_0 and L_f are the initial and final specimen dimensions along the measurement direction. Three replicate tests were carried out for each salinity level, and the mean and sample standard deviation were calculated.

Measured results were considered strictly as linear swelling strains without conversion to volumetric clay expansion, pore volume changes, or porosity changes calculated from micro-CT measurements.

Pre- and Post-Flood Micro-CT Comparison

A representative C1 sample which had been flooded with 3000 ppm brine was subjected to analysis via X-ray micro-computed tomography (micro-CT) before and after flooding. Comparable areas of interest in the pre- and post-flood images were assessed using the same threshold for segmentation and process rule. The pore regions that were segmented are shown in the processed images in magenta.

From the scan export, the nominal voxel size is 1.8 µm. Hence, a qualitative assessment of changes in the spatial distribution and geometry of the resolved pore regions was performed before and after flooding. However, the nominal voxel size was not treated as an independently verified spatial resolution. Structures that are smaller than the imaging scale that is resolved were not assigned.

Micro-CT assessment was limited to the representative C1 sample only at 3000 ppm and was not used to make quantitative assessments of the porosity and connectivity changes in the entire core set. Mineral assignment was not made based on grayscale intensity alone.

2.6. Data Processing and Calculation Methods

Analysis of the measured coreflooding data was carried out to obtain values of the injected pore volumes, OOIP, recovery efficiency, residual oil saturation, water cut, differential pressure, saturation history, and normalized phase-flow indices. A consistent computational procedure was used for all the HSWF, LSWF, CEOR, and WAG tests to allow comparison of the displacing techniques. In the equations below, (i) refers to the core sample number, (j) refers to the measurement step or injected pore volume, (m) refers to the displacing technique, and (c) refers to the WAG cycle.

The pore volume of core (i) was calculated using Equation (1):

$$V_{p,i} = \frac{W_{sat,i} - W_{dry,i}}{\rho_w}, \quad (1)$$

where $\boldsymbol{V_{p,i}}$ is the pore volume of core specimen i, $\boldsymbol{W_{sat,i}}$ is the weight of core specimen i that is saturated with brine, $\boldsymbol{W_{dry,i}}$ is the dry weight of core specimen i, and $\boldsymbol{\rho_w}$ is the density of brine.

The value of original oil in place (OOIP) for core sample i was determined from Equation (2):

$$OOIP_i = V_{p,i} \cdot S_{oi,i} \quad (2)$$

where $\boldsymbol{S_{oi,i}}$ is the initial oil saturation of core specimen i.

While the injected pore volume at measurement stage j $\boldsymbol{PV_{inj,i,j}}$ was calculated as expressed in Equation (3):

$$PV_{inj,i,j} = \frac{V_{inj,i,j}}{V_{p,i}}, \quad (3)$$

where $\boldsymbol{V_{inj,i,j}}$ is the cumulative volume of injected fluid.

The recovery factor (RF) of core sample i at measurement stage j was obtained from Equation (4):

$$RF_{i,j} = \frac{N_{p,i,j}}{OOIP_i} \cdot 100, \quad (4)$$

where $\boldsymbol{N_{p,i,j}}$ is the cumulative volume of produced oil.

The oil saturation of core sample i at measurement stage j was computed via Equation (5):

$$S_{o,i,j} = S_{oi,i} - \frac{N_{p,i,j}}{V_{p,i}} \quad (5)$$

The residual oil saturation of core sample i was derived using Equation (6):

$$S_{or,i} = S_{oi,i} - \frac{N_{p,i,f}}{V_{p,i}}, \quad (6)$$

where $\boldsymbol{N_{p,i,f}}$ is the final cumulative volume of produced oil.

During the displacement of oil–water, the water saturation of core sample i at measurement stage j was calculated from the balance of saturation via Equation (7):

$$S_{w,i,j} = 1 - S_{o,i,j} \quad (7)$$

However, during the WAG experiments, because of gas presence, the saturation balance was written as in Equation (8):

$$S_{w,i,j} + S_{o,i,j} + S_{g,i,j} = 1, \quad (8)$$

where $\boldsymbol{S_{g,i,j}}$ is the gas saturation of core sample i at measurement step j.

By means of Equation (9), the water cut of core sample i at measurement step j $\boldsymbol{f_{w,i,j}}$, was determined:

$$f_{w,i,j} = \frac{q_{w,i,j}}{q_{w,i,j} + q_{o,i,j}} \cdot 100, \quad (9)$$

where $\boldsymbol{q_{o,i,j}}$ is the flow rate of produced oil, and $\boldsymbol{q_{w,i,j}}$ is the flow rate of water produced.

Using Equation (10), differential pressure ($\boldsymbol{\Delta P_{i,j}}$) across core sample i at measurement stage j was calculated:

$$\Delta P_{i,j} = P_{in,i,j} - P_{out,i,j}, \quad (10)$$

where $P_{in,i,j}$ is the inlet pressure, and $P_{out,i,j}$ is the outlet pressure.

Normalized oil and water phase-flow indices were calculated using Equations (11) and (12), respectively.$k_{ro,i,j}k_{rw,i,j}$

$$k_{ro,i,j} = \frac{q_{o,i,j} \cdot \mu_o \cdot L_i}{k_i \cdot A_i \cdot \Delta P_{i,j}}, \tag{11}$$

$$k_{rw,i,j} = \frac{q_{w,i,j} \cdot \mu_w \cdot L_i}{k_i \cdot A_i \cdot \Delta P_{i,j}}, \tag{12}$$

where $q_{o,i,j}$ and $q_{w,i,j}$ are the flow rates of oil and water, μ_o and μ_w are the viscosity values of oil and water, respectively. L_i is the length of core sample i, k_i is the absolute permeability, and A_i is the cross-sectional area of core sample i.

The calculated values of Equations (11) and (12) are the Darcy-normalized phase-flow indices that are obtained from the measured oil and water production rates, the overall differential pressure across the core, the absolute permeability, and the phase-viscosity values used in the data reduction. They should not be taken as independently measured constitutive relative-permeability functions.

In unsteady-state displacement, the two phases do not necessarily share the same phase-pressure gradients, because the capillary pressure and fluid saturations may vary along the core. In the present calculation, we apply the measured total core differential pressure to both the oil and water produced phases. We do not attempt to separate the phase-specific pressure gradient, capillary-pressure gradient, transient accumulation of fluids, capillary-end effects, or any local phase redistribution.

In addition, for the LSWF and AOS-assisted CEOR cases, any potential spatial or temporal change in aqueous-phase viscosity, interfacial tension, surfactant retention, and emulsion behavior has already been reflected in the measured rate and pressure. Even though the interfacial tension is not explicitly included in Equations (11) and (12), it can affect the capillary pressure, fluid configuration, phase connectivity, and displacement pressure, all of which have an indirect influence on the calculated normalized phase-flow index.

Thus, normalized oil and water phase-flow indices are used here only as a qualitative comparison of the effective phase-flow response, and they are not used as a rigorous steady-state relative-permeability curve or a direct constitutive relative-permeability input for reservoir simulation.

The average recovery factor for displacement technique m was quantified through Equation (13):

$$\overline{RF_m} = \frac{1}{n} \cdot \sum_{i=1}^{n} RF_{i,m} \tag{13}$$

The average residual oil saturation for displacement technique m was quantified through Equation (14):

$$\overline{S}_{or,m} = \frac{1}{n} \cdot \sum_{i=1}^{n} S_{or,i,m}, \tag{14}$$

where n, in Equations (13) and (14), is the number of core samples.

To establish the incremental recovery improvement (ΔRF_m) of technique m relative to the HSWF baseline, Equation (15) was used:

$$\Delta RF_m = \overline{RF_m} - \overline{RF}_{HSWF} \tag{15}$$

Equation (16) provided the cycle contribution to recovery within the WAG experiment:

$$\Delta RF_{WAG,c} = RF^f_{WAG,c} - RF^i_{WAG,c} \tag{16}$$

where $RF^{i}_{WAG,c}$ is the recovery factor at the beginning of cycle c, and $RF^{f}_{WAG,c}$ is the recovery factor at the end of cycle c during the WAG experiment.

The results were analyzed to evaluate: (1) oil recovery, (2) residual oil saturation, (3) pressure variation, (4) water-cut history, (5) saturation changes, and (6) normalized phase-flow indices under varying levels of salinity control, interfacial-tension reduction, and gas–water cyclic saturation reversal.

Order-of-Magnitude Capillary-Number Estimation

To provide a quantitative comparison of the balance between viscous and capillary forces, two complementary capillary-number estimates were calculated. The nominal flow-based capillary number was defined as:

$$u = \frac{q}{A} \tag{17}$$

$$N_c^{(q)} = \frac{\mu_d u}{\sigma} \tag{18}$$

where u is the superficial velocity, q is the volumetric injection rate, A is the cross-sectional area of the core, μ_d is the viscosity of the displacing phase, and σ is the oil–water interfacial tension.

The diameter of the core was 2 in., which corresponds to a cross-sectional area of 2.027×10^{-3} m^2. For a typical liquid injection rate of 0.30 mL/min, we found a superficial velocity of 2.47×10^{-6} m/s. The measured fluid-specific aqueous viscosities reported below were used for the HSWF, LSWF, AOS-assisted CEOR, and aqueous WAG-slug calculations.

A complementary pressure-gradient capillary-number estimate was calculated as:

$$N_c^{(\Delta P)} = \frac{k\Delta P}{L\sigma} \tag{19}$$

Here, k is the arithmetic mean absolute permeability of the seven cores, ΔP is the representative measured peak differential pressure, and L is the core length. The mean absolute permeability was 223.6 mD (or equivalent to 2.21×10^{-13} m^2), and L was 0.3048 m. Since absolute permeability is employed here instead of the saturation-dependent effective permeability of the displacing phase, $N_c^{(\Delta P)}$ is an upper-bound screening estimate rather than an accurate pore-scale capillary number.

The representative mean peak differential pressures used in the screening calculation were roughly 1.66 psi for HSWF, 1.29 psi for the best-performing LSWF, and 1.22 psi for 0.5 wt% AOS-assisted CEOR. The direct measurement of dynamic interfacial tension (IFT) was carried out separately at 70 °C between oil and water for the main fluid systems that were used for the analysis of capillary number. The plateau values of the interfacial tension were determined to be 24.7 ± 0.2 mN/m for crude oil against brine solution with 56,300 ppm HSWF, 22.5 ± 0.2 mN/m for crude oil against brine with 7600 ppm, and 2.65 ± 0.10 mN/m for crude oil against 0.5 wt% AOS in brine solution with 7600 ppm. The viscosities of the aqueous solutions at 70 °C were determined to be 0.470 ± 0.003, 0.438 ± 0.003, and 0.485 ± 0.005 cP, respectively. The experimental values of the above parameters were used in the calculation of the capillary number equation. The CMC characterization described above was obtained from air–solution surface-tension measurements and was not used as a substitute for oil–water interfacial tension in the capillary-number calculations.

Flow-based and pressure gradient capillary numbers were examined separately as complementary screening estimates. The flow rate and differential pressure were not combined through multiplication for a single definition.

We did not assign a single conventional capillary number to the entire N_2-WAG process because WAG involves three fluid phases, gas–oil, gas–water, and oil–water interfaces, different phase viscosities, gas trapping, and repeated saturation reversals. Instead, stage-wise flow-based estimates were made for comparison. The oil–water capillary number of the aqueous WAG slugs was calculated using the properties of the best-performing 7600 ppm brine, and an order-of-magnitude bound for the N_2 slugs was calculated using the N_2 viscosity at the test conditions [35,36] and an assumed gas–oil IFT range of 5–25 mN/m, because the gas–oil IFT was not measured.

2.7. Statistical Analysis, Variability, and Uncertainty

For each condition, the mean, sample standard deviation, and minimum–maximum range of the endpoint recovery factor, the residual oil saturation, and the peak differential pressure measured for each core sample were reported. We also report the 95% confidence interval for the mean in cases when specified. The sample standard deviation is calculated with n − 1 degrees of freedom, and the 95% confidence interval for the mean is calculated according to Equation (20):

$$CI_{95\%} = \overline{x} \pm t_{0.975,n-1}\frac{s}{\sqrt{n}} \quad (20)$$

where $\bar{x}$ is the sample mean, s is the sample standard deviation, and n is the number of experimental units contributing to the corresponding summary. For the seven-run coreflood summaries, $n = 7$ and $\boldsymbol{t_{0.975,6}} = 2.447$; for the triplicate swelling measurements, $n = 3$ and $\boldsymbol{t_{0.975,2}} = 4.303$. The twenty sequential effluent fractions produced in one run were considered to be repeats from the same run and not independent replicate corefloods.

The residual oil saturation is calculated individually for each core using its core-specific initial oil saturation and its core-specific final recovery factor as described in Equation (21):

$$S_{or,i} = S_{oi,i}\left(1 - \frac{RF_i}{100}\right) \quad (21)$$

where $\boldsymbol{S_{or,i}}$ is the final residual oil saturation, $\boldsymbol{S_{oi,i}}$ is the initial oil saturation, and $\boldsymbol{RF_i}$ is the final recovery factor expressed as % OOIP for core specimen i.

The differences in treatments were evaluated using the agreement between the C1–C7 parent-core source labels. In the comparison of post-LSWF results with freshly cut samples, agreement indicates the same parent-core origin and not re-measurements of the same sample. The difference in the recovery factor of treatment m from the HSWF reference was calculated using Equation (22):

$$\Delta RF_{i,m} = RF_{i,m} - RF_{i,HSWF} \quad (22)$$

Then the mean, sample standard deviation, range, and 95% confidence interval for these source-matched differences were calculated. Comparisons between treatments relative to the HSWF reference were performed on a parent-core-source-matched basis by considering the seven corresponding C1–C7 experimental pairs. The recovery-factor difference for each treatment was calculated separately as $\boldsymbol{\Delta RF_i = RF_{treatment,i} - RF_{HSWF,i}}$, where i denotes the corresponding parent-core source. Since the matched sample size was small ($n = 7$ pairs), a two-sided exact Wilcoxon signed-rank test was used for statistical inference. Three comparisons were considered: 7600 ppm LSWF versus HSWF, 0.5 wt% AOS-assisted CEOR versus HSWF, and N_2-WAG versus HSWF. To control the family-wise error rate for these three comparisons, the p values were adjusted using the Holm method. Matched differences, descriptive statistics, exact Wilcoxon p values, and Holm-adjusted p values are provided in Section 3.5. Matching refers to the same parent-core source and does not imply repeated flooding of the same physical specimen.

The main C1–C7 datasets include one independently initialized coreflood per parent-core-source/condition combination and, as such, represent primarily between-sample and between-test variability rather than technical repeatability. Technical repeatability was assessed separately using independently conducted duplicate corefloods under the 7600 ppm LSWF and 0.5 wt% AOS-assisted CEOR conditions. Each duplicate test used a new, independently prepared parent-core-matched specimen. The duplicate confirmation tests were analyzed separately from the main $n = 7$ treatment datasets and were not pooled into the C1–C7 statistical population.

2.8. Rate-Sensitivity Assessment

The rate sensitivity of the displacement endpoint and the effect of capillary end effects were investigated in a series of rate-sensitivity tests using independently prepared sandstone core specimens that match those used in the parent cores. Three liquid injection rates of 0.15, 0.30, and 0.60 mL/min corresponding to superficial velocities of 1.23×10^{-6}, 2.47×10^{-6}, and 4.93×10^{-6} m/s (0.35, 0.70, and 1.40 ft/day), respectively, were selected. Tests were performed using 56,300 ppm HSWF brine at 70 °C, 4000 psi backpressure and 5000 psi confining pressure, and 2.0 PV injection volume. To eliminate any flow rate effect from previous history, independent and identically matched core specimens were used at each injection rate. Porosity, permeability, initial fluid saturation, wettability conditioning, and pressure–temperature equilibrium were all performed using the same protocol as in the coreflood tests. The recovery, residual oil saturation, water cut, and differential pressure were then evaluated for the 2.0 PV endpoint condition. The complete rate-sensitivity dataset is provided in Table A1.

2.9. Direct Capillary-Hysteresis and Rock–Fluid Confirmation Measurements

To obtain the experimental validation of capillary-pressure hysteresis, an equilibrium drainage-imbibition $\boldsymbol{P_c - S_w}$ experiment was performed on one of the sandstone core specimens labeled C1-HYS, which was selected from the parent sample C1 that was used in the experimental procedure. The diameter and length of the specimen were found to be 38.10 mm, effective porosity to be 21.3%, pore volume to be 9.25 cm^3, and absolute permeability to be 316 mD. To perform the experiment, the same oil and 7600 ppm multicomponent brine at 70 °C were used as before. The densities of the brine and oil at the experimental temperature were 1.004 g/cm^3 and 0.824 g/cm^3, respectively.

The sample was subjected to primary drainage through centrifugal capillary-pressure equipment after preparation and brine saturation. The rotation of the centrifuge was gradually increased from 0 to 3000 rpm, which is equivalent to an equilibrium capillary pressure range of 0–8.12 psi depending on the geometry of the cell and fluid density contrast. The experiment was carried out until there were no changes in the produced volume for two 15 min readings.

After achieving the primary drainage endpoint, the saturation direction was reversed to obtain the main imbibition curve. The internal reversal that followed was begun at about $\boldsymbol{S_w} = 0.60$. Partial drainage reduced $\boldsymbol{S_w}$ to 0.43, followed by re-imbibition to increase $\boldsymbol{S_w}$ to 0.68. The paths generated by primary drainage, main imbibition, and internal reversal were used to study the effect of saturation history on the $\boldsymbol{P_c - S_w}$ relationship.

Complementary captive drop contact angle experiments were conducted at six spots, prior to and following the $\boldsymbol{P_c - S_w}$ cycle. Dynamic oil–water interfacial tension (IFT) was independently determined at 70 °C in crude oil mixed with brines containing HSWF 56,300 ppm, 7600 ppm, and BIO-TERGE® AS-40 0.5 wt% in 7600 ppm brine. The stabilized plateau values were obtained when the difference in IFT values was less than 0.05 mN/m during a 5 min time period. Fluid-specific aqueous viscosities at 70 °C were independently

determined using an SVM 3001 Stabinger viscometer (Anton Paar GmbH, Graz, Austria), with three fresh samples per formulation.

3. Results

3.1. Baseline High-Salinity Waterflooding Performance

The high-salinity waterflooding (HSWF) test used 56,300 ppm brine to establish a baseline for comparison with low-salinity waterflooding, AOS-assisted chemical EOR, and water-alternating-gas (WAG) procedures. Baseline displacement tests define the recovery and residual-oil endpoint under the applied forced-imbibition conditions. In porous media, residual oil after waterflooding is usually controlled by capillary trapping, pore-throat geometry, phase disconnection, saturation-history effects and relative-permeability hysteresis. Therefore, the baseline HSWF served as the recovery benchmark against which the other treatment endpoints were compared.

Table 5 presents the recovery factor and residual oil saturation for the baseline HSWF experiment. Across all runs, the average final recovery factor was 53.15% OOIP, while the mean residual oil saturation was 34.57% PV. This indicates that a substantial fraction of the oil remained after passage of the waterflood front under the applied baseline conditions.

Table 5. Baseline HSWF recovery endpoints for the original C1–C7 sandstone specimens.

Core ID	*RF*, % OOIP	S_{or}, % PV
C1	57.89	32
C2	52.05	35
C3	45.07	39
C4	47.22	38
C5	54.05	34
C6	59.74	31
C7	56	33
Mean ± SD (n = 7)	53.15 ± 5.42	34.57 ± 2.99

Comparison of the endpoints for the HSWF in Table 5 with the reference core property values in Table 1 shows that there was variability in recovery throughout the tested permeability range and across the reservoir intervals. The highest baseline recoveries of 57.89% and 59.74% OOIP correspond to the cores with the highest permeabilities of 320 and 380 mD, respectively (Balakhany X). In contrast, the lowest recoveries of 45.07% and 47.22% OOIP were found for the cores with the lowest permeabilities of 95 and 110 mD (Balakhany IX). This can be explained by stronger capillary constraints and reduced accessible oil connectivity in low-permeability specimens. The intermediate values of recovery factors were observed for the Pereriv B and Pereriv D core samples in accordance with their permeabilities.

Figure 2 shows the baseline HSWF displacement process through recovery factor, water cut, and differential pressure as functions of injected pore volume. These curves illustrate the transition from the initial oil-dominated regime to a water-dominated regime.

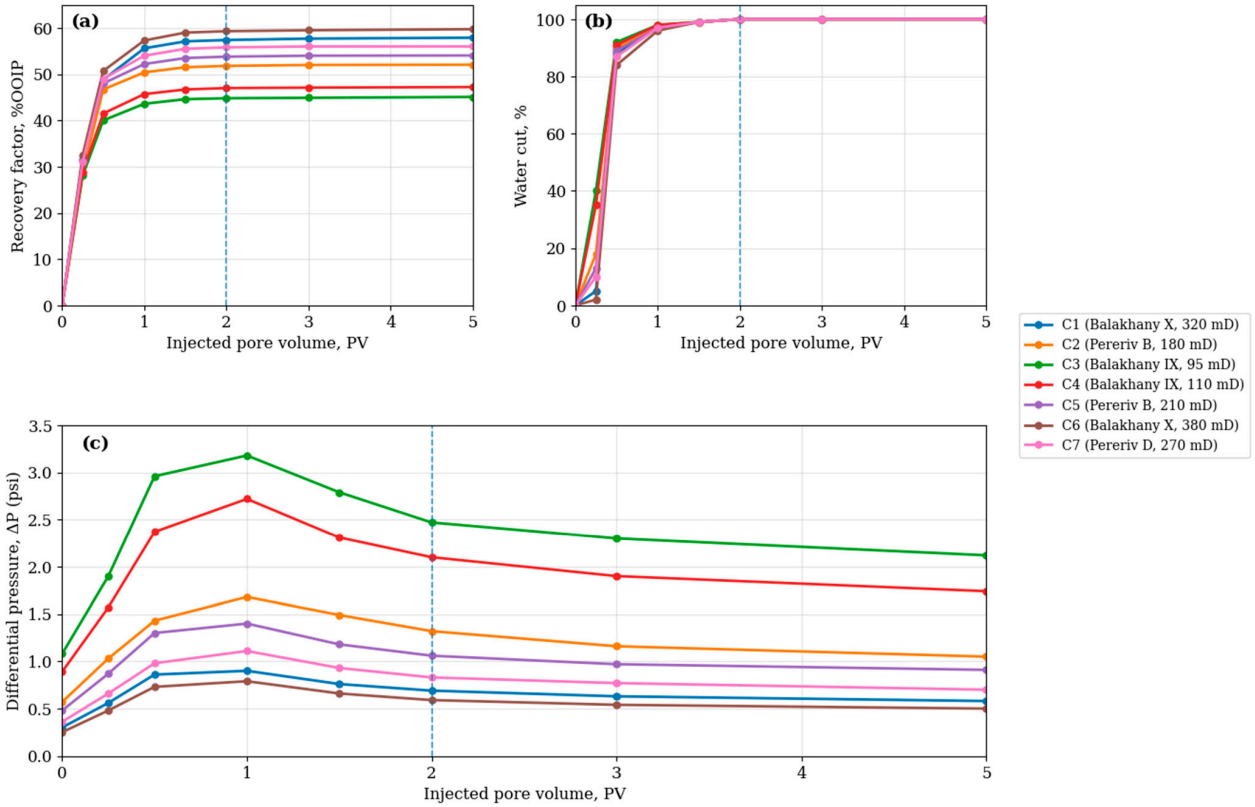


Figure 2. Baseline high-salinity waterflooding (HSWF) histories for the original C1–C7 sandstone specimens: (**a**) recovery factor, (**b**) water cut, and (**c**) differential pressure versus injected pore volume. The dashed line marks the common treatment-comparison endpoint at 2.0 PV.

The oil recovery curve in Figure 2a shows that oil recovery increased quickly during the initial period. This rapid initial oil production results from displacement of connected and mobile oil by the injected water. At later times, the oil-production rate and the slope of the recovery curve decrease as the response approaches the final recovery value. A recovery plateau is an indication of the continuous fall in oil production due to increased water injection with the existing level of residual oil under the applied waterflood conditions. This recovery plateau represents reduced accessible oil connectivity and capillary trapping, in which additionally injected water primarily follows the established water paths.

The water-cut data presented in Figure 2b support these observations. As seen earlier, the water cut was initially very low because most of the produced fluid was oil displaced from the connected pores of the cores by the injected brine. As the experiment was performed and brine began to continuously flow from the core inlet to the core outlet, the water cut increased rapidly. Once the water cut reached the maximum level, the injected water became predominant, and the produced fluid shifted toward a water-dominant flow regime. This shift is important in terms of capillary hysteresis, as it is the stage at which oil connectivity becomes progressively reduced during the imbibition of water.

The change in pressure drop shown in Figure 2c is consistent with the further change in flow regime. The initial increase in pressure drop is consistent with the two-phase flow conditions during the early displacement period since the flow of water into the oil-filled pores introduces two-phase flow resistance. In this regime, the two phases of oil and water occupy the pores simultaneously, and the effective phase mobility of oil and water is reduced, causing a higher flow resistance. As the experiment progressed and the water paths became continuous, the pressure drop leveled off and then declined slightly as continuous water pathways developed. This trend is consistent with the ex-

pected shift in phase-flow behavior as the water saturation increases and the oil saturation decreases; as the oil saturation decreases, the oil-phase mobility drops and the water-phase mobility increases.

Figure 3 provides a qualitative comparison of the phase-flow transition during baseline HSWF rather than a determination of intrinsic oil–water relative-permeability relationships. Because the curves are derived from unsteady-state production data and overall pressure-drop measurements, their magnitudes may be influenced by saturation-dependent phase continuity, fluid-storage effects, capillary-pressure profiles, phase interference, and capillary-end effects. Accordingly, the decrease in the normalized oil phase-flow index and the increase in the normalized water phase-flow index are interpreted as reflecting a shift in the relative contributions of the oil and water phases during displacement. The indices should not be considered steady-state relative-permeability endpoints or functions of water saturation alone.

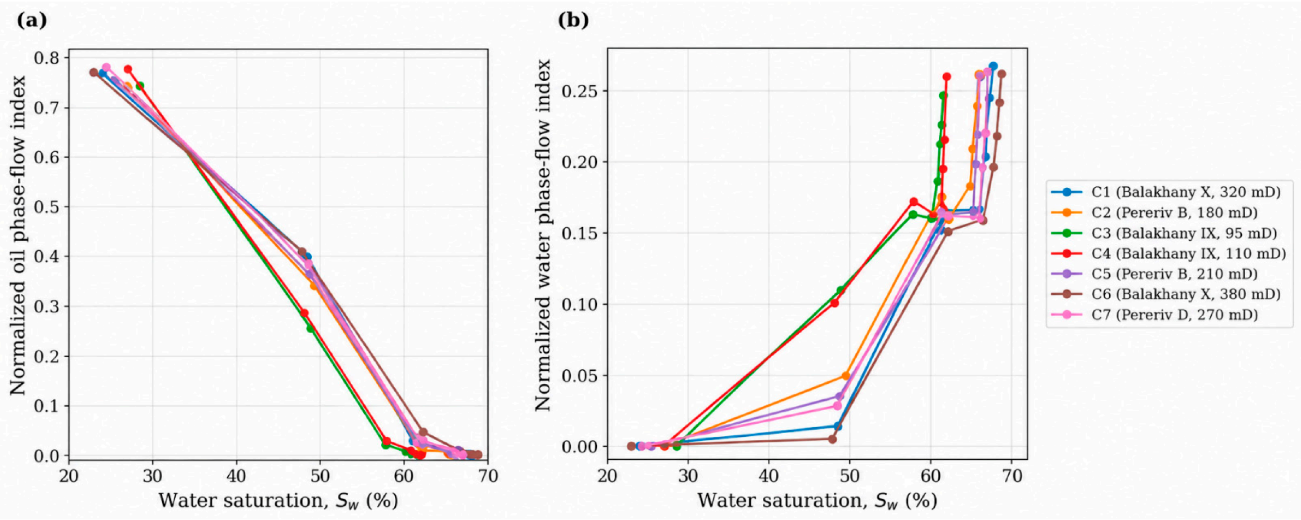


Figure 3. Baseline normalized phase-flow behavior for the original C1–C7 sandstone core samples: (**a**) normalized oil phase-flow index versus water saturation and (**b**) normalized water phase-flow index versus water saturation.

Figure 3 presents the normalized oil and water phase-flow indices for the baseline displacement experiment. These indices, obtained from unsteady-state performance and total differential pressure data, only function as qualitative measures of the relative contributions of the oil and water flow during the displacement process. They are not relative permeabilities.

Figure 3a shows that the normalized oil phase-flow index drops continuously with increasing water saturation. This trend is consistent with the progressive loss of oil connectivity during forced imbibition. The lower water saturation means that there is still some oil phase connectivity, and the mobility of the oil is higher. With increasing water saturation, the water occupies the connected pore system, making oil pathways less continuous and reducing oil mobility. The drop in the normalized oil phase-flow index corresponds to the displacement that is dependent on saturation history, although the current HSWF imbibition path alone cannot demonstrate drainage-imbibition relative permeability hysteresis.

Figure 3b shows the opposite trend for the normalized water phase-flow index. With increasing water saturation, the water phase becomes more connected and transports an increasing share of the total flow. This increase in water mobility explains the increase in water cut shown in Figure 2b. However, the increase in normalized water phase-flow index does not mean that the remaining oil is effectively displaced. When water becomes the

dominant flowing phase, the injected brine sweeps less oil. This phenomenon is the reason for the increase in the water cut coinciding with reaching the oil plateau.

The normalized phase-flow indices should be evaluated with these limitations in mind. Equations (11) and (12) apply Darcy's law to unsteady-state production data using the total differential pressure across the core; consequently, the indices combine the effects of phase mobility, capillary-pressure gradients, capillary end effects, and transient saturation redistribution. Even for HSWF, in which the composition of the injected brine remained constant, the indices in Figure 3 therefore reflect only the trend in the combined (co-flow) capacity of the oil and water phases to move under the imposed total pressure drop, and not the intrinsic relative permeability of either phase. Accordingly, Figure 3 is used only to identify the direction and timing of the transition from oil-dominated to water-dominated flow, and not to derive relative-permeability endpoints or curve shapes.

A combined analysis of Figures 2 and 3 indicates that the baseline HSWF experiment created a typical displacement process controlled by imbibition waterflood in a sandstone. The initial increase in the recovery is related to the displacement of mobile oil, while the further plateau is determined by reduced accessible oil connectivity and capillary trapping. Therefore, the final residual oil saturation of 34.57% pore volume (PV) describes a history-dependent residual endpoint, which is developed due to forced imbibition. This point is defined by the saturation history of the experiment since the oil was already established in the core and then displaced by high-salinity brine during forced imbibition, creating a residual oil state that depends on the imposed saturation path.

These data help explain why the baseline HSWF process does not achieve maximum oil recovery in these cores. Even though the high-salinity waterflooding treatment displaces a part of the mobile oil, it does not directly target capillary forces, wettability, interfacial tension, or saturation path. Thus, the remaining oil after the HSWF treatment is consistent with residual capillary trapping and phase disconnection under the applied displacement conditions. LSWF was investigated to study its impact on rock–brine–oil interactions and, hence, the resulting residual trapping behavior. CEOR was studied to investigate the impact of surfactant-reduced interfacial tension on oil mobilization, while WAG was used to cause gas–brine saturation reversals.

Therefore, the baseline HSWF results support three main conclusions. First, the sandstone cores show obvious residual oil capillary trapping after conventional waterflooding. Second, the recovery varies depending on the permeability and zone, meaning that pore structure influences the displacement efficiency of the baseline displacement process. Third, the plateau, the increase in the water cut, and normalized phase-flow trends are consistent with the transition of the baseline displacement process into a water-dominated regime while some oil remains trapped. These results provide the experimental baseline for evaluating the LSWF, CEOR, and WAG responses in terms of residual oil saturation and saturation-history effects.

3.2. Low-Salinity Waterflooding Optimization

Low-salinity waterflooding was assessed to evaluate the effects of salinity reduction on oil displacement performance and residual oil saturation in the tested sandstone cores. Unlike simply injecting the lowest possible salinity brine, the aim of this stage was to select the best-performing brine condition among those tested. Thus, a stepwise salinity screening process was performed using brines ranging from 56,300 to 1000 ppm. Additional confirmation experiments were carried out to examine the reduced displacement efficiency observed at 3000 and 1000 ppm.

Table 6 presents the summary of recovery factors and residual oil saturations obtained during the salinity screening tests.

Table 6. Salinity-screening endpoints. Values for 7600, 3000, and 1000 ppm are shown as mean ± SD of samples; values for all other data are from the original screen summaries.

TDS (ppm)	Basis	Final S_{or}, % PV	RF, % OOIP
56,300	Baseline	34.57	53.15
28,700	Original screening	33.2	55.0
15,000	Original screening	32.41	56.2
10,000	Original screening	30.78	58.4
7600	Current run data, $n = 7$	28.52 ± 3.36	61.31 ± 5.69
5000	Original screening	30.41	58.9
3000	Current run data, $n = 7$	33.56 ± 3.42	54.5 ± 5.96
1000	Current run data, $n = 7$	37.63 ± 3.50	49 ± 6.24

Table 6 shows a non-monotonic relationship between salinity reduction and oil recovery. A decrease in brine salinity from 56,300 ppm to 7600 ppm increased the average recovery factor from 53.15 ± 5.42% to 61.31 ± 5.69% OOIP and reduced the average residual oil saturation from 34.57 ± 2.99% to 28.52 ± 3.36% PV. This comparison indicates improved displacement performance as salinity was reduced from the HSWF reference to 7600 ppm. However, a further decrease in salinity below 7600 ppm could not maintain this recovery enhancement. At 5000 ppm, the average recovery factor dropped to 58.90% OOIP, and at 1000 ppm it decreased to 49.00 ± 6.24% OOIP, which is lower than in the baseline HSWF case. Thus, the best-performing brine among those tested was not the lowest-salinity brine, but the condition that provided the best balance between recovery and injectivity. The endpoint dependence on brine salinity is presented in Figure 4.

Figure 4a shows that oil recovery increased monotonically as brine salinity was decreased from 56,300 ppm to 7600 ppm. This trend is interpreted as a favorable low-salinity response in the tested sandstone cores. Since the sandstone reservoirs include minerals and clay components which are reactive, a decrease in brine salinity may alter ion exchange, surface charge and the behavior of the electrical double layer, thereby changing rock–brine–oil interactions. This leads to oil release from the mineral surfaces and makes displacement easier, as less oil will be trapped due to capillary forces. This interpretation is consistent with the mineralogical analysis presented in Table 2, according to which feldspar, illite/mica, illite-smectite, chlorite and kaolinite are capable of participating in the above-mentioned processes.

Figure 4b shows the corresponding drop in residual oil saturation from 34.57% PV at 56,300 ppm to 28.52% PV at 7600 ppm. The current investigation focuses not only on increasing recovery but also on reducing capillary-hysteresis-related oil trapping. In the baseline HSWF case, a significant part of the remaining oil was trapped as a result of the loss of oil-phase connectivity with the formation of disconnected oil ganglia which were retained by capillary trapping. Therefore, the lower value of S_{or} at 7600 ppm means that brine salinity decrease changed the displacement pathway and made the amount of the retained oil smaller than in the HSWF case. Thus, the LSWF response is consistent with a shift in the residual-trapping endpoint relative to the HSWF reference under the tested rock–brine–oil conditions.

The peak differential pressure shown in Figure 4c plays an important role when selecting the best-performing salinity among the tested conditions. Although decreasing salinity to 7600 ppm resulted in increased oil recovery, further salinity reduction increased differential pressure and decreased recovery. This phenomenon corresponds to the increased resistance to flow at low-salinity levels and is further substantiated by the additional tests

on particle migration, swelling, and permeability impairment at 3000 ppm and 1000 ppm. In a clay-containing sandstone formation, drastic lowering of ionic strength can promote destabilization of clay particles or mobilization of fines that partially occlude pore throats and decrease effective permeability. The combined effects of pressure, solids, swelling, and permeability indicate that the adverse rock–brine reactions contributed to the poor displacement efficiency obtained at concentrations of 3000 and 1000 ppm.

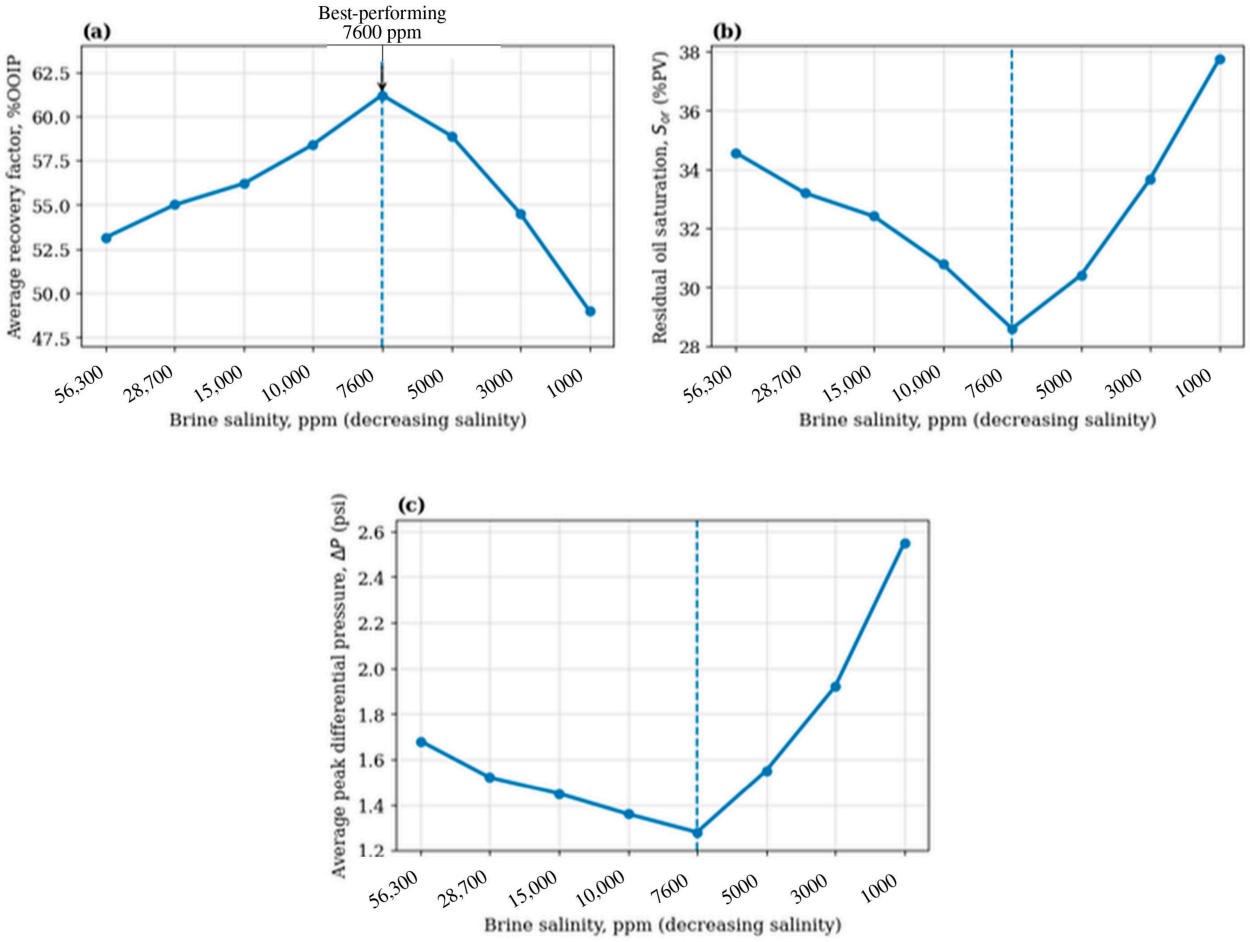


Figure 4. Low-salinity waterflooding salinity-screening response: (**a**) recovery factor, (**b**) residual oil saturation, and (**c**) peak differential pressure as functions of brine salinity.

For that reason, pressure response is an important criterion; recovery factor should not be used alone to choose the best-performing brine among the tested conditions. The dynamics of selected salinity cases are illustrated in Figure 5.

Figure 5a shows that the 7600 ppm brine achieved a higher recovery response than the 56,300 ppm HSWF reference. The difference between the two curves becomes noticeable after the initial stage of mobile oil displacement. This indicates that the 7600 ppm brine mobilized more trapped or bypassed oil than the HSWF process. The difference between the curves at higher injected volumes is consistent with a sustained low-salinity displacement effect after the initial displacement period.

The water-cut trajectory in Figure 5b supports the choice of 7600 ppm as the best-performing salinity among the tested conditions. Compared to the baseline HSWF case, the 7600 ppm LSWF produced a more favorable water-cut trajectory, which indicates better oil displacement prior to the formation of fully water-dominated flow. A smaller or delayed rise in water cut means that the injected brine contacted and displaced more oil before establishing a dominant water path. In terms of saturation-history-dependent displacement,

this behavior is consistent with a reduced tendency for early water bypassing and more sustained oil displacement during imbibition.

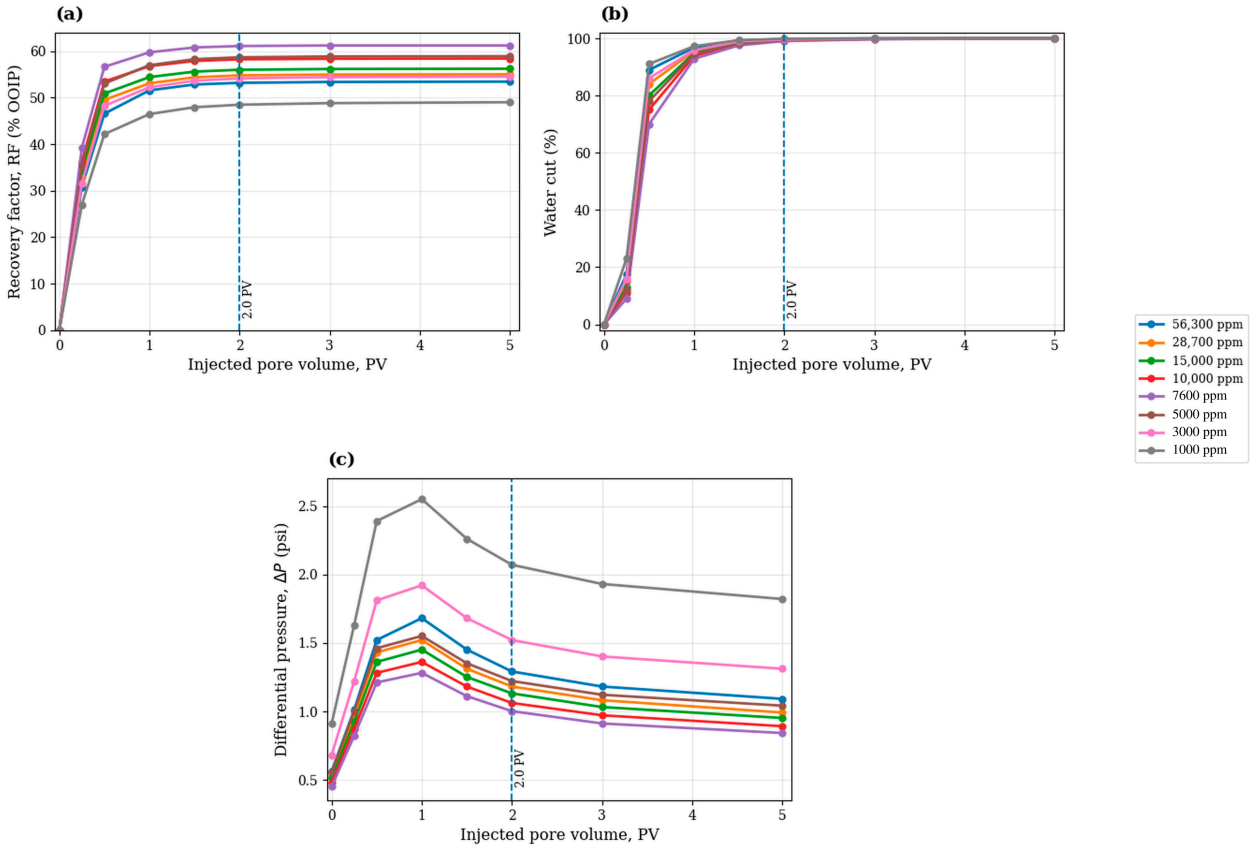


Figure 5. Dynamic LSWF displacement response for selected salinity cases: (**a**) recovery factor versus injected pore volume, (**b**) water cut versus injected pore volume, and (**c**) differential pressure versus injected pore volume.

Figure 5c shows that the 7600 ppm brine provided a stable pressure response in comparison with the low-salinity cases. This indicates that the 7600 ppm salinity enhanced the recovery with a relatively favorable pressure response. Pressure response is especially important for clay-containing sandstones since a sharp rise in pressure during low-salinity injection may indicate clay swelling, fines migration, or pore throat blocking. That is why the 7600 ppm brine was selected not only because of the highest recovery factor and lowest residual oil saturation, but also because of the most stable displacement pressure compared to the lower-salinity brines.

The link between the low-salinity response and capillary hysteresis can be interpreted through the influence of brine composition on the forces controlling oil trapping. During baseline waterflooding, the displacement process occurred along the forced imbibition path and stopped at a residual oil state defined by capillary trapping. Upon reduction of salinity to the best-performing salinity of 7600 ppm, the interactions between the rock, brine and oil changed in such a way that the residual trapping point became lower than the HSWF. This indicates that the residual oil saturation after imbibition depends not only on pore geometry but also on brine chemistry. In other words, the 7600 ppm LSWF produced a lower residual-oil endpoint than HSWF, consistent with brine-chemistry-dependent changes in oil-trapping conditions.

The non-monotonic behavior observed in this study is also important for field design. If only one low-salinity brine had been studied, the best-performing salinity range could have been missed. The results indicate that salinity reduction provides a favorable oper-

ating window, while too much dilution may lead to adverse displacement and injectivity responses. This issue is especially important for formations that contain illite-smectite, illite/mica, chlorite and kaolinite. As different minerals may behave in different ways upon reduction of ionic strength, selection of the best-performing salinity should consider both recovery and pressure response. In the current experiments, 7600 ppm provided the best trade-off between enhanced oil recovery, residual oil saturation, and stable injectivity.

The following descriptive statistics provide a quantification of this non-monotonic effect: the mean recovery factor and the mean residual oil saturation at 7600 ppm were 61.31 ± 5.69% OOIP and 28.52 ± 3.36% PV, respectively. For 3000 ppm, the respective values were 54.50 ± 5.96% OOIP and 33.56 ± 3.42% PV, whereas for 1000 ppm, the respective values were 49.00 ± 6.24% OOIP and 37.63 ± 3.50% PV. The mean peak differential pressure increased from 1.29 ± 0.36 psi at 7600 ppm to 1.95 ± 0.60 psi at 3000 ppm and to 2.55 ± 0.87 psi at 1000 ppm. These descriptive statistics represent the results obtained for the seven runs recorded for each salinity level. Specimen allocation for each run is described in Section 2.4. The 7600 ppm condition was also characterized by significantly lower particle production, swelling, and permeability impairment compared to the 3000 and 1000 ppm conditions, and a small but non-zero permeability loss was observed. Therefore, the favorable salinity range is specific to the tested sandstone–oil–brine system and cannot be considered a universal salinity threshold. Additional evidence on adverse effects at lower salinities is provided in Section Confirmation of the Adverse Low-Salinity Response.

Overall, the LSWF results show that salinity control modifies residual oil trapping associated with capillary hysteresis in the tested sandstone cores. The average recovery factor increased from 53.15% OOIP for HSWF to 61.31 ± 5.69% OOIP at 7600 ppm, indicating improved displacement efficiency under the best-performing low-salinity condition. However, the recovery reduction below 7600 ppm indicates that low salinity is not necessarily beneficial at any dilution level. Accordingly, 7600 ppm was selected as the best-performing LSWF brine and used as the carrier brine for the AOS-assisted CEOR and N_2-WAG programs.

Confirmation of the Adverse Low-Salinity Response

The blank-corrected gravimetric analysis shows an increase in particle generation with decreasing salinity (Table 7; Figure 6). The run-level volume-weighted concentration values obtained for particle generation for 7600, 3000, and 1000 ppm salinity conditions were 13.99 ± 4.02, 95.01 ± 24.98, and 225.00 ± 54.99 mg/L, respectively. The cumulative solids produced over 2.0 pore volumes (PV) were found to be 2.62 ± 0.77, 18.39 ± 4.92, and 44.66 ± 11.10 mg/run, respectively. The concentrations of the particles produced at 3000 and 1000 ppm salinity were about 6.8 and 16.1 times the average particle concentration at 7600 ppm salinity. These results quantify the particulate matter transported to the outlet but do not quantify the material retained within the rock.

Mean permeability retention ratios for brine sensitivity experiments were found to be 0.960 ± 0.015, 0.760 ± 0.055, and 0.520 ± 0.070 for salinity levels of 7600, 3000, and 1000 ppm, respectively. This implies permeability reductions of 4.00 ± 1.48%, 24.00 ± 5.48%, and 48.00 ± 7.00%, respectively (Table 7; Figure A1). The permeability response indicates decreasing flow capacity with decreasing salinity, consistent with the increased differential pressure observed in the oil-displacement tests. Permeability reduction was small but non-zero at 7600 ppm, whereas substantially greater impairment occurred at 3000 and 1000 ppm.

Independent triplicate swelling tests yielded average linear strains of 0.721 ± 0.124%, 2.885 ± 0.496%, and 6.182 ± 1.062% after 24 h at 70 °C with brine concentrations of 7600, 3000, and 1000 ppm, respectively (Table 7; Figure A1). These observations directly show

that specimen expansion during the swelling tests was salinity-dependent. An increased expansion with decreasing salinity points to swelling as one of the mechanisms responsible for pore-space restriction during low-salinity flooding. Nevertheless, measured bulk linear strain does not qualify as a measurement of porosity change in the confined coreflood specimen.

Table 7. Confirmation measurements and displacement endpoints at 7600, 3000, and 1000 ppm.

Metric and Population	7600 ppm	3000 ppm	1000 ppm
RF (% OOIP), 7 runs	61.31 ± 5.69	54.50 ± 5.96	49.00 ± 6.24
S_{or} (% PV), 7 runs	28.52 ± 3.36	33.56 ± 3.42	37.63 ± 3.50
Peak ΔP (psi), 7 runs	1.29 ± 0.36	1.95 ± 0.60	2.55 ± 0.87
Volume-weighted solids (mg/L), 7 runs	13.99 ± 4.02	95.01 ± 24.98	225.00 ± 54.99
Produced solids (mg/run), 7 runs	2.62 ± 0.77	18.39 ± 4.92	44.66 ± 11.10
Calculated k_f (mD), 7 records	215.95 ± 105.04	174.81 ± 92.69	122.50 ± 70.60
k_f/k_o, 7 records	0.960 ± 0.015	0.760 ± 0.055	0.520 ± 0.070
Permeability loss (%), 7 records	4.00 ± 1.48	24.00 ± 5.48	48.00 ± 7.00
Linear swelling (%), 3 specimens	0.721 ± 0.124	2.885 ± 0.496	6.182 ± 1.062
Mean blank (mg/filter), 7 blanks	0.0300	0.0300	0.0300
Blank sample SD (mg)	0.001291	0.001155	0.001155
Matched micro-CT observation	No matched pair presented	C1: reduced resolved pore regions	No matched pair presented

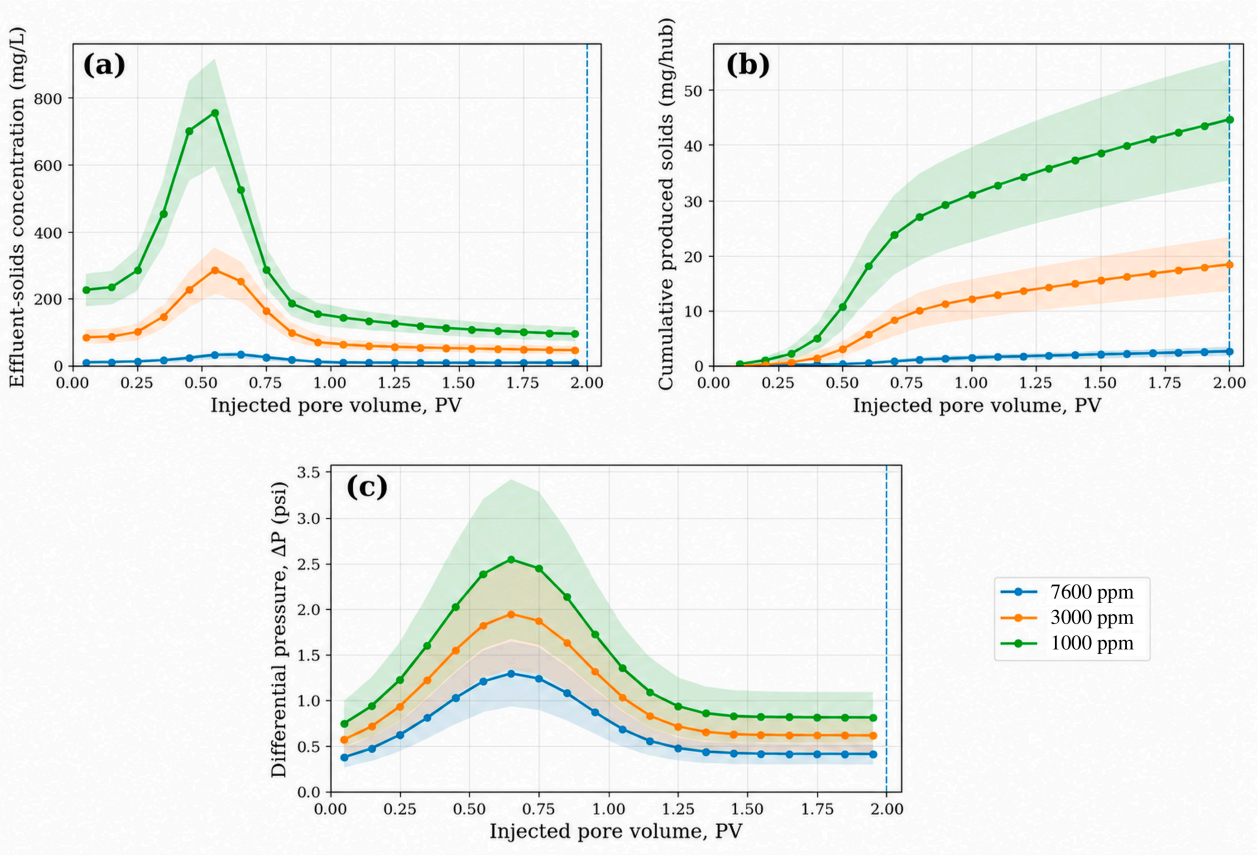


Figure 6. Confirmation response for salinity variation across 0–2.0 injected PV: (**a**) blank-corrected effluent solids concentration, (**b**) cumulative produced solids, and (**c**) differential pressure.

A micro-CT before/after comparison test was performed for the C1 specimen flooded with 3000 ppm brine concentration (Figure 7). The same segmentation rule was applied to the matched internal regions of interest. The post-flood micro-CT images show a decrease in resolved pore regions within parts of the sample. Such an observation supports local restriction of the resolved pore space following low-salinity flooding. With the nominal voxel size of 1.8 µm, the micro-CT images are taken as measurements on the scale of resolved pore geometry and not as identification of individual migrating fines or specific clay swelling.

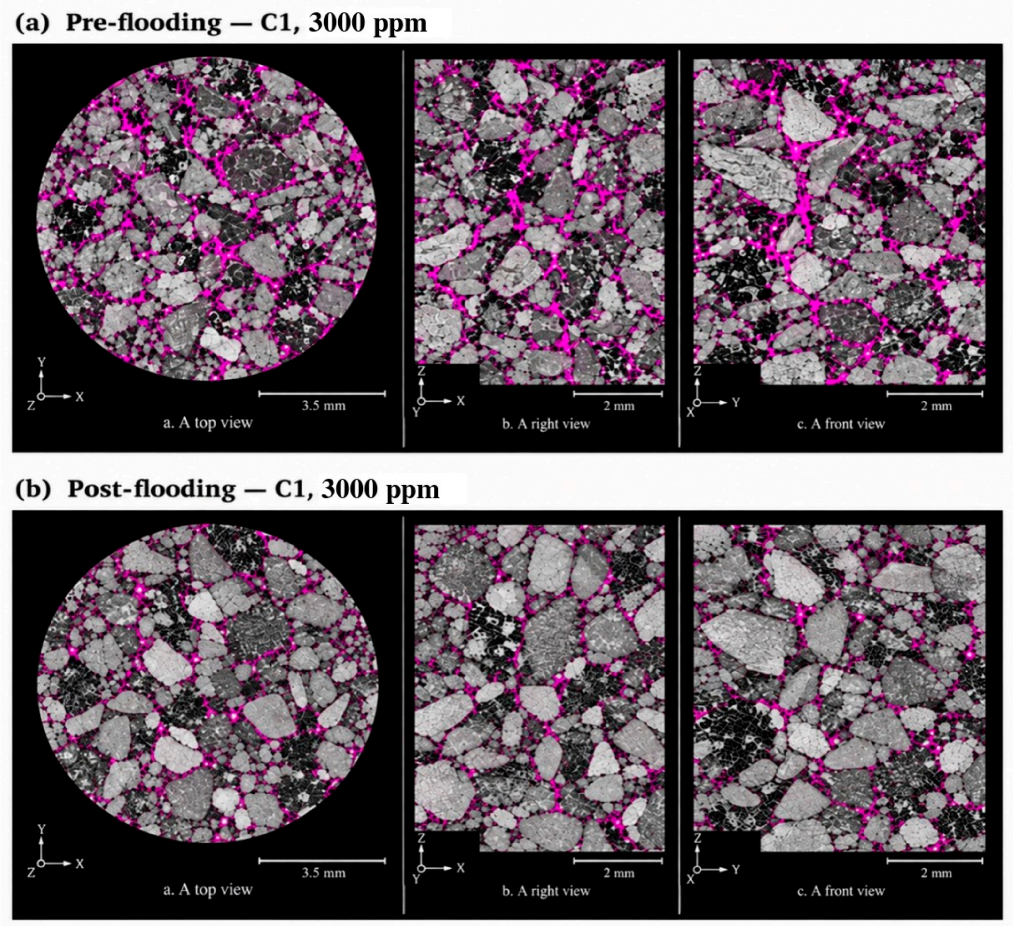


Figure 7. Micro-CT views of the representative C1 specimen before (**a**) and after (**b**) flooding with 3000 ppm brine. Magenta indicates the segmented pore regions; the grayscale background shows the micro-CT image.

In summary, the confirmation measurements support swelling and fines migration as contributing processes to the observed adverse low-salinity response. The swelling measurements indicate specimen expansion due to lower salinity. Gravimetric measurements demonstrated greater fines transport at the lower salinities. Permeability measurements showed reduced flow capacity. The representative micro-CT image provides visual evidence of local restriction of the resolved pore space. The concurrence of these responses, together with reduced recovery factors and increased differential pressures at 3000 and 1000 ppm, provides converging evidence beyond the differential-pressure response alone. Magenta indicates the segmented pore regions; the grayscale background shows the micro-CT image.

3.3. AOS-Assisted Chemical EOR Performance

After 7600 ppm was identified as the best-performing low-salinity brine, AOS-assisted chemical enhanced oil recovery (CEOR) was evaluated to determine whether interfacial-tension (IFT) reduction would promote residual-oil mobilization. The 7600 ppm low-salinity brine served as the carrier fluid for the surfactant solution. Alpha-olefin sulfonate (AOS) was selected as the surfactant, considering the prevalent application of anionic surfactants in sandstone chemical EOR studies because of their effectiveness in IFT reduction and displacement efficiency with appropriate formulation. In this study, AOS concentrations of 0.3, 0.5, and 1.0 wt% were screened to identify the best-performing concentration among those tested. Table 8 presents the endpoint results of the AOS concentration-screening experiment.

Table 8. AOS concentration-screening endpoints in 7600 ppm low-salinity brine.

Injected Fluid	Commercial AOS Product Concentration, wt%	Peak ΔP, psi	Final, S_{or} % PV	*RF*, % OOIP
The best-performing LSWF	0	1.29 ± 0.36	28.52 ± 3.36	61.31 ± 5.69
AOS-assisted CEOR	0.3	1.35 ± 0.21	24.84 ± 3.65	66.29 ± 5.94
AOS-assisted CEOR	0.5	1.22 ± 0.20	22.60 ± 4.00	69.30 ± 6.32
AOS-assisted CEOR	1.0	1.38 ± 0.22	23.44 ± 3.95	68.17 ± 6.29

Note: Nominal concentrations refer to BIO-TERGE® AS-40 as received (39 wt% active matter); 0.3, 0.5, and 1.0 wt% product correspond to 0.117, 0.195, and 0.390 wt% active AOS, respectively.

Measurements of air–solution surface tension in 7600 ppm brine at 70 °C showed a sharp and strong dependence of surface tension on concentration followed by a flat part of the curve. Surface tension dropped from 65.70 ± 0.10 mN/m for surfactant-free brine to 31.80 ± 0.10 mN/m at 0.030 wt% of commercial product and to 28.10 ± 0.10 mN/m at 0.050 wt%. The point where the descending and flat parts of the curve met gave the critical micelle concentration (CMC) of 0.044 wt% of commercial product, which is equal to 0.017 wt% of active AOS. At the three coreflood concentrations, surface tensions averaged 27.40 ± 0.10, 27.30 ± 0.10, and 27.23 ± 0.06 mN/m at 0.3, 0.5, and 1.0 wt%, respectively. Thus, all three concentrations were greater than the CMC determined experimentally. The full concentration–surface-tension profile and the CMC determination are presented in Figure A2.

AOS improved endpoint recovery relative to the 7600 ppm LSWF reference. On average, the recovery factor increased from 61.31 ± 5.69% OOIP without the use of AOS to 66.29 ± 5.94% OOIP at 0.3 wt% AOS, and reached the highest value of 69.30 ± 6.32% OOIP at 0.5 wt% AOS. As a result, the value of residual oil saturation at 0.5 wt% AOS was 22.60 ± 4.00% PV, compared with 28.52 ± 3.36% PV for the LSWF reference. The 0.5 wt% solution gave the minimum value of the peak differential pressure, 1.22 ± 0.20 psi. No additional improvement in the recovery factor was achieved by raising the concentration of AOS to 1.0 wt%. The average recovery became lower at 68.17 ± 6.29% OOIP, and the average residual oil saturation was 23.44 ± 3.95%.

Figure 8a shows that the recovery factor increases from 66.29 ± 5.94% OOIP under 0.3 wt% AOS to 69.30 ± 6.32% OOIP under 0.5 wt% AOS. Although 0.3 wt% surfactant produced a CEOR response, the higher recovery at 0.5 wt% indicates greater oil mobilization under the tested conditions. Mean coreflood recovery showed a rise from 66.29 ± 5.94% OOIP at 0.3 wt% to 69.30 ± 6.32% OOIP at 0.5 wt% commercial product. Both concentrations were above the CMC of the surfactant solution and fell into the air–solution surface tension plateau zone. Thus, the increased recovery at 0.5 wt% cannot be explained by any further

decrease in the measured air–solution surface tension. The coreflood results reveal that 0.5 wt% is the best-performing tested operating concentration. The dynamic measurements of oil–water interfacial tension (IFT) show that the IFT of the 0.5 wt% AOS formulation is noticeably lower than that for surfactant-free brines. However, the differences in coreflood performance of 0.5 and 1.0 wt% AOS formulations cannot be explained exclusively by IFT or CMC; other concentration-dependent effects may also contribute.

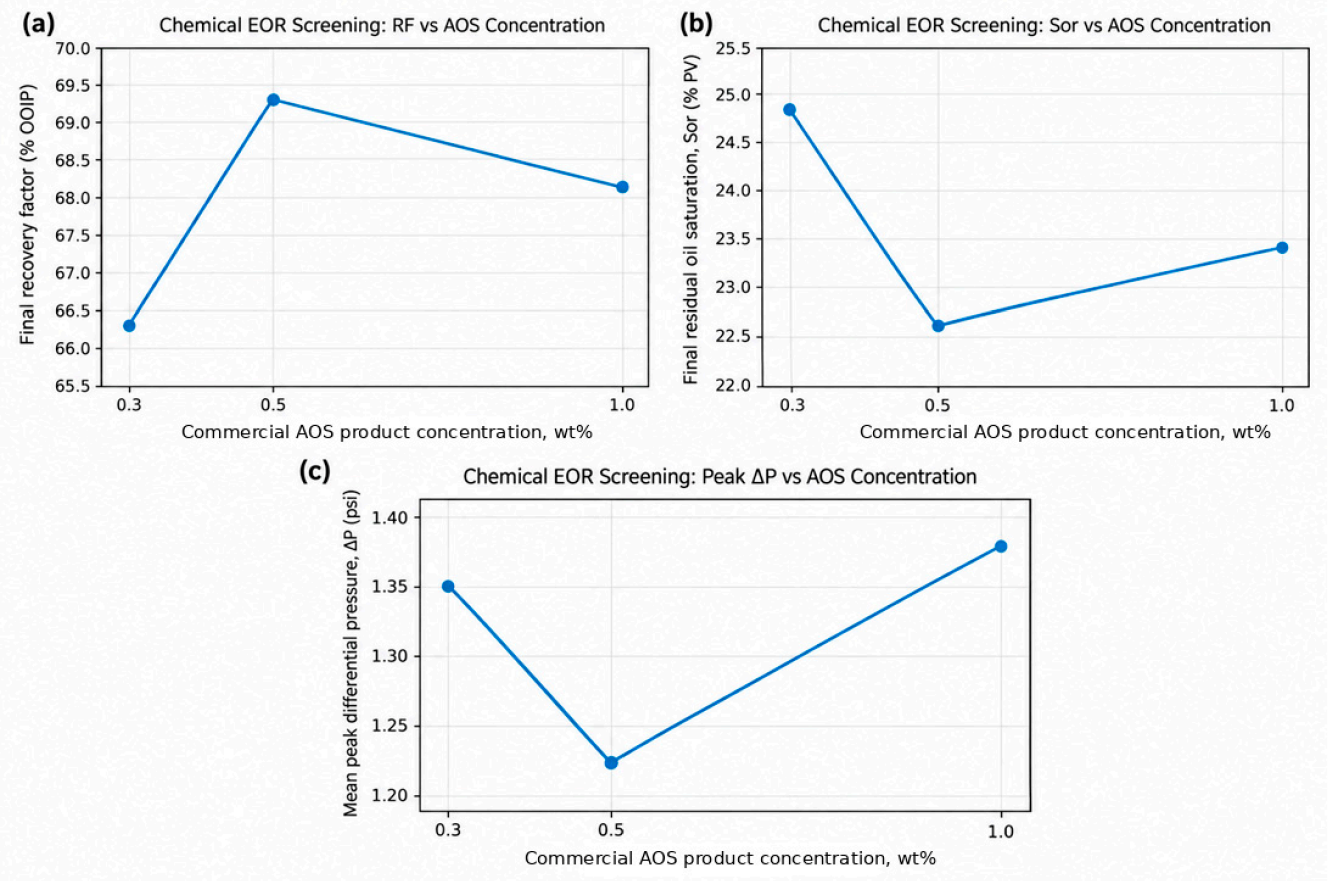


Figure 8. AOS concentration screening in the best-performing low-salinity brine: (**a**) final recovery factor versus AOS concentration, (**b**) final residual oil saturation versus AOS concentration, and (**c**) peak differential pressure versus AOS concentration.

Nevertheless, there was no obvious improvement in recovery when the AOS concentration was increased from 0.5 to 1.0 wt%. The average final recovery factor was reduced only marginally from 69.30 ± 6.32 to 68.17 ± 6.29% OOIP. Meanwhile, average residual oil saturation increased from 22.60 ± 4.00 to 23.44 ± 3.95% PV and average peak differential pressure increased from 1.22 ± 0.20 to 1.38 ± 0.22 psi. As the recovery factors for these two concentrations overlap in distribution, this observation is considered to indicate a lack of further recovery enhancement at 1.0 wt%, rather than indicating a significant degradation in recovery.

The CMC was found to be 0.044 wt% in the commercial formulation (0.017 wt% active AOS). Hence, the 0.3, 0.5, and 1.0 wt% coreflood mixtures are equivalent to about 6.8, 11.3, and 22.7 times the determined CMC, respectively. Among these three concentrations, there were no significant changes in the experimentally determined air–solution surface tension, which approached 27.40 ± 0.10, 27.30 ± 0.10, and 27.23 ± 0.06 mN/m. Therefore, the absence of additional recovery at 1.0 wt% is consistent with the diminishing change in the measured air–solution surface tension above the CMC; however, the specific cause of the coreflood response cannot be assigned from the CMC measurement alone.

In addition to possible IFT effects, possible surfactant self-assembly may also impact the solubilization of oil and overall properties of the bulk fluid. In particular, at higher surfactant concentration, possible increases in adsorption or retention, changes in viscosity of the surfactant solution, and formation of oil-in-water emulsions or larger surfactant-rich structures might lead to additional local flow resistance and the increase in differential pressure observed here. Note, however, that it is not suggested here that ordinary micelles would be capable of causing mechanical pore blockage. The dynamic IFT between the oil and water phases was determined separately at 70 °C for the main fluid mixtures; however, no tests were conducted to determine the micelle or aggregate size, solution rheology, phase behavior, emulsion droplet size and stability, surfactant retention, and effluent surfactant concentration. As a result, the above mechanisms can still be considered potential explanations of the differences between the 0.5 and 1.0 wt% coreflood results.

The measured CMC also clarifies the concentration regime in which the slightly lower performance at 1.0 wt% occurred. Because the CMC (0.044 wt% commercial product) was exceeded at all three coreflood concentrations, the CMC was not first reached at the highest concentration; rather, the additional surfactant supplied at 1.0 wt% was present predominantly in micellar form. Above the CMC, the monomer concentration, and therefore the equilibrium interfacial adsorption, remains approximately constant. This is reflected in the air–solution surface tension, which changed by only 0.07 mN/m between 0.5 and 1.0 wt% (27.30 ± 0.10 versus 27.23 ± 0.06 mN/m). A corresponding saturation of the oil–water IFT reduction above the CMC is therefore expected, although the oil–water IFT was measured only for the 0.5 wt% formulation. Consequently, increasing the concentration from 0.5 to 1.0 wt% would not be expected to produce a substantial further reduction in IFT or a corresponding increase in capillary number, which is consistent with the absence of additional recovery. A higher micellar concentration may instead enhance oil solubilization, emulsification, and the formation of larger surfactant-rich aggregates. Individual micelles are of nanometer scale and therefore several orders of magnitude smaller than the micrometer-scale pore throats of the 95–380 mD sandstones, so that direct pore-throat blockage by micelles is not plausible. Emulsion droplets, in contrast, can be comparable in size to pore throats and can increase flow resistance through the Jamin effect. The moderate increase in the mean peak differential pressure from 1.22 ± 0.20 to 1.38 ± 0.22 psi (approximately 13%) is compatible with a limited contribution from emulsion- or retention-related flow resistance, but not with severe emulsion blockage, which would be expected to cause a pronounced and persistent pressure increase. Because emulsion droplet size, effluent emulsion content, phase behavior, and surfactant retention were not measured, these mechanisms remain plausible interpretations rather than demonstrated causes of the slightly lower performance at 1.0 wt%.

Figure 8b shows that the mean final residual oil saturation was lowest at 0.5 wt% AOS among the tested concentrations. The mean final residual oil saturation S_{or} decreased from 24.84 ± 3.65% PV at 0.3 wt% to 22.60 ± 4.00% PV at 0.5 wt% AOS; thus, 0.5 wt% AOS produced the lowest residual oil saturation among the tested concentrations. At 1.0 wt%, residual oil saturation S_{or} increased slightly to 23.44 ± 3.95% PV. This slight increase coincides with the trend of recovery. Residual oil saturation is an endpoint indicator of oil remaining after displacement. The lower value at 0.5 wt% AOS is consistent with reduced residual trapping compared with the other tested concentrations.

As shown in Figure 8c, the 0.5 wt% AOS solution resulted in a lower mean peak differential pressure (1.22 ± 0.20 psi) compared to 1.35 ± 0.21 psi and 1.38 ± 0.22 psi observed at 0.3 wt% and 1.0 wt%, respectively. Although a higher mean pressure at 1.0 wt% is consistent with local increases in flow resistance, this alone cannot be used to determine the specific cause of the increase in resistance. Retention, viscosity effects

and emulsions/aggregates are potential sources of such increased resistance. As none of these effects was directly measured, it is considered an indication of less favorable flow response, but not proof of a specific mechanism. Thus, 0.5 wt% AOS was chosen as the best-performing operating concentration from among those tested.

Figure 9 below compares normalized phase-flow indices for HSWF, 7600 ppm LSWF, and AOS-assisted CEOR. The differences between the curves represent the relative response to the treatments of the flow rates and pressures of oil and water phases and cannot be viewed as proof of any change in intrinsic relative permeability. A more careful interpretation of the normalized phase-flow indices in Figure 9 is necessary compared to that for the baseline HSWF case. The observed differences between HSWF, the best-performing LSWF and the AOS-assisted CEOR curves are the result of the rate–pressure response of the two phases during each treatment, and they are not a unique indicator of a change in the intrinsic relative permeability. For example, in the LSWF case, the calculated rate and pressure responses could be a result of salinity-dependent rock–brine–oil interactions, capillary-pressure changes and/or fines effects. In the CEOR case, a combination of factors including interfacial tension change, surfactant retention, aqueous phase viscosity, emulsification, phase connectivity and saturation redistribution could all influence the resulting flow rates and the differential pressure. Despite the characterization of the viscosity of the aqueous phase and the dynamic IFT between the oil and water phases at 70 °C, the local pressure gradients in the corresponding phases or the interfacial properties were not determined in the core while displacement was taking place. Thus, Figure 9 is used only for comparing the effective phase-flow behavior and does not represent the measurement of intrinsic relative permeability curves. A higher normalized oil phase-flow index indicates a higher normalized oil-flow rate contribution under the corresponding experimental conditions, whereas the later rise in the normalized water phase-flow index indicates a later onset of water-dominated production. These trends are viewed along with recovery factor, water-cut, residual oil saturation and differential pressure, and should not be taken as independent measures of the intrinsic oil and water relative-permeability functions.

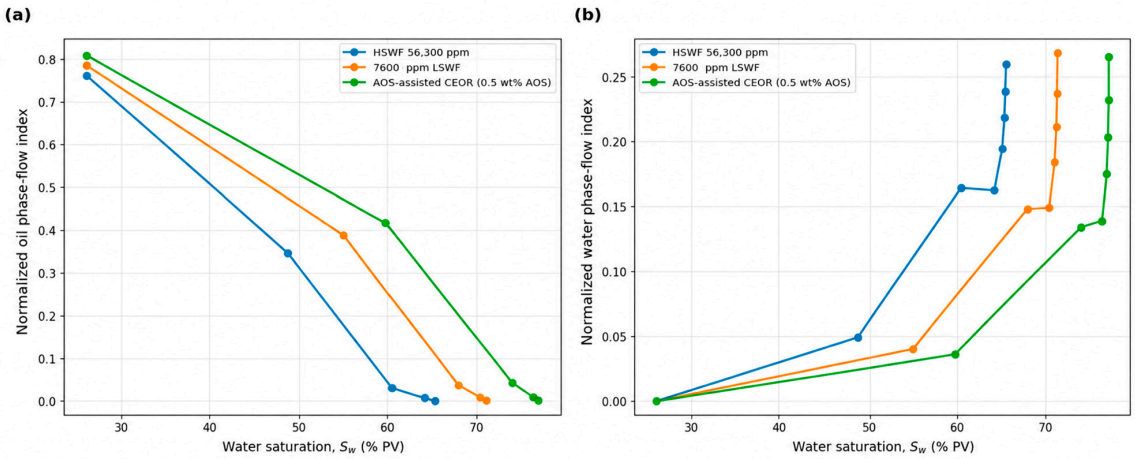


Figure 9. Normalized phase-flow-index comparison for HSWF, the best-performing LSWF, and AOS-assisted CEOR: (**a**) normalized oil phase-flow index versus water saturation and (**b**) normalized water phase-flow index versus water saturation.

Figure 9a shows that the normalized oil phase-flow index for CEOR is generally higher than that for HSWF and 7600 ppm LSWF across a wide range of water saturation. This indicates a higher normalized oil-flow contribution during CEOR as water saturation increases. In the HSWF case, the drop in the normalized oil phase-flow index occurs faster due to the earlier disconnection of the oil phase under forced imbibition. The best-

performing LSWF shows an intermediate response, while the largest normalized oil-flow contribution is observed for CEOR. The increased normalized oil-phase flow index noted for CEOR indicates a larger normalized oil-flow contribution under the tested conditions. This pattern is consistent with the increased recovery factor, decreased residual oil saturation, and water cut behavior independently measured. Since the normalized phase flow index is not a constitutive relative permeability measurement, it cannot be used by itself to claim increased mobility of the oil or to establish a certain pore-scale mechanism.

Figure 9b shows the corresponding normalized water phase-flow behavior. In the baseline HSWF case, the value of the normalized water phase-flow index rapidly increases with the water saturation, which is consistent with the early development of the water-dominated pathways. The best-performing LSWF case shows some improvement, but the CEOR results show the largest delay in the increase in the normalized water phase-flow index. In practical terms, water-dominated flow develops later in the CEOR case than in HSWF or LSWF. This is relevant because the early development of the water-dominated flow can be associated with bypassing of oil and fast accumulation of residual trapping.

The delayed normalized water phase-flow response is consistent with the normalized oil phase-flow trend and qualitatively agrees with the later transition toward water-dominated production during CEOR. This comparison is interpreted together with recovery factor, residual oil saturation, water cut, and differential pressure, rather than independently as mechanistic proof.

The results obtained for oil–water phase-flow behavior suggest that the CEOR displacement process differed from HSWF and LSWF throughout the flood, rather than only at the residual-oil endpoint. This result is consistent with the decrease in oil–water interfacial tension as well as oil mobilization observed during the surfactant-enhanced flooding process. However, since no data regarding relative-permeability hysteresis were obtained during the CEOR corefloods, Figure 9 must be considered as evidence of comparative flow behavior.

For the LSWF and CEOR cases, the limitations of this Darcy-based data reduction are more pronounced than for HSWF. During LSWF, salinity-dependent rock–brine interactions can change the flow capacity of the rock itself; even at 7600 ppm, a small permeability reduction of $4.00 \pm 1.48\%$ was measured (Section Confirmation of the Adverse Low-Salinity Response), so that the absolute permeability used for normalization is not strictly constant. During CEOR, the aqueous phase changes from the surfactant slug to the surfactant-free chase brine; the oil–water IFT is reduced by approximately one order of magnitude (from 22.5 ± 0.2 to 2.65 ± 0.10 mN/m) where surfactant is present, and dilution, retention, and possible emulsification can alter the effective aqueous-phase viscosity in situ. Equations (11) and (12), however, assign a single viscosity to each phase and the overall core pressure drop to each data point, and they do not account for the IFT-dependent capillary-pressure gradient. The normalized phase-flow indices in Figure 9 therefore reflect only the trend in the combined (co-flow) capacity of the oil and water phases under each treatment and should not be regarded as the intrinsic relative permeabilities of the individual phases. Their differences are used only qualitatively and only in conjunction with the independently measured recovery factor, residual oil saturation, water cut, and differential pressure.

As shown in Figure 10a, the CEOR recovery curve remains above the HSWF and 7600 ppm LSWF baselines throughout the principal displacement process. The recovery factor increases significantly during the initial period of surfactant injection and reaches the plateau level much higher than in the HSWF and 7600 ppm LSWF cases. Already at 0.5 PV of injection, CEOR shows a higher recovery factor than LSWF and HSWF; thus, the surfactant response is consistent with improved oil mobilization during surfactant-assisted flooding. The CEOR curve reaches $69.30 \pm 6.32\%$ OOIP of total oil, while the 7600 ppm

LSWF and HSWF are 61.31 ± 5.69% and 53.15 ± 5.42% OOIP, respectively. These data show greater oil recovery for AOS-assisted CEOR than for the 7600 ppm LSWF reference.

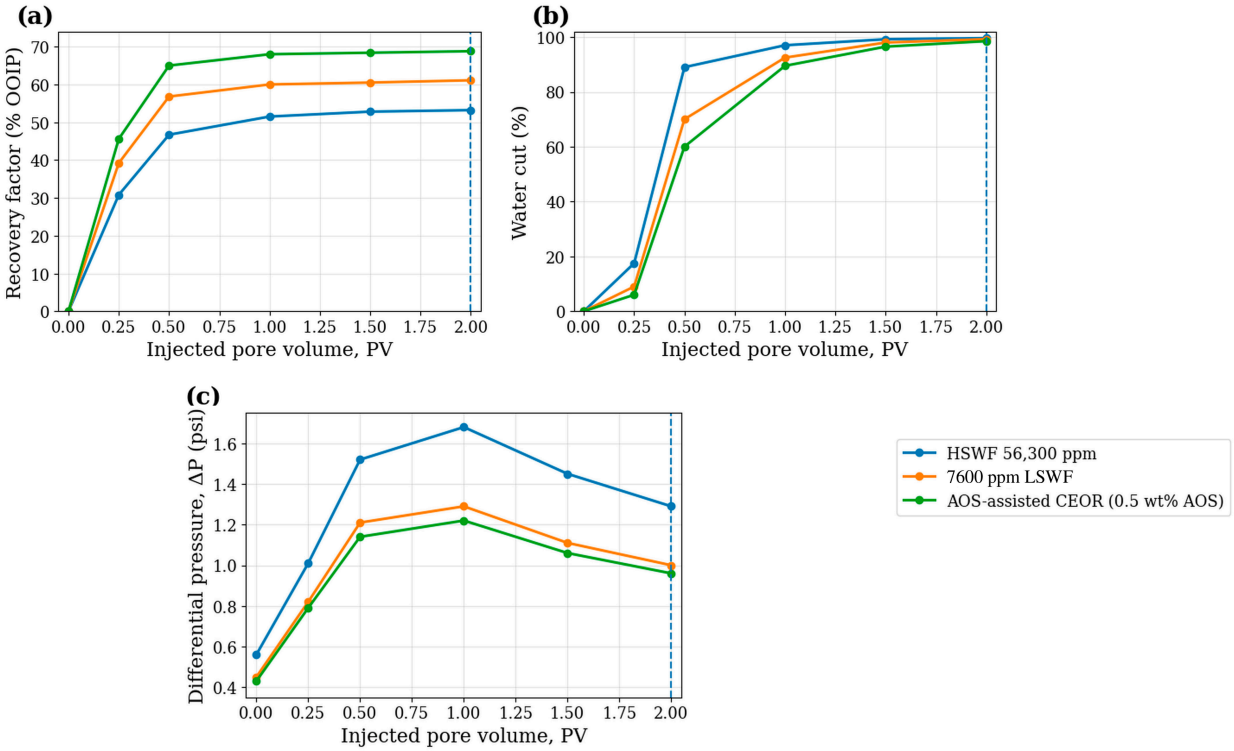


Figure 10. HSWF, 7600 ppm LSWF, and AOS-assisted CEOR histories: (**a**) recovery factor, (**b**) water cut, and (**c**) differential pressure versus injected pore volume.

The vertical dashed lines indicate the common comparison endpoint of 2.0 injected PV.

The recovery-curve shapes also provide useful comparative information. The recovery curve of HSWF rapidly approaches an early plateau, which is consistent with increasing residual oil trapping in the conventional waterflood. The recovery curve of 7600 ppm LSWF moves up because of the best-performing salinity, which affects the rock–brine–oil interactions and thus reduces some portion of residual oil trapping. The CEOR recovery curve shifts up again because of the surfactant, which reduces interfacial and capillary resistance. Consequently, the difference between the three recovery curves is consistent with distinct displacement mechanisms: baseline imbibition trapping for HSWF, salinity-modified rock–fluid interactions in LSWF, and IFT-reduced trapping for CEOR.

As shown in Figure 10b, the water-cut behavior shows clear differences between the three techniques. The baseline case of HSWF shows the earliest transition to high water cut, indicating rapid establishment of water-dominated flow paths. The 7600 ppm LSWF case slightly delays this transition, while the CEOR case shows the most favorable water-cut behavior. At the same injected pore volumes, CEOR provides the lowest water cut level during the early and intermediate stages of the displacement process, indicating additional oil production before complete establishment of water-dominated flow paths.

This behavior is consistent with reduced capillary trapping during CEOR. During the forced imbibition, oil becomes increasingly disconnected as the water saturation increases. As soon as this disconnection is achieved, the water cut starts increasing fast and the oil production decreases. In the case of CEOR, the direct reduction in the oil–water interfacial tension is attributed to reduced capillary resistance and improved oil mobilization during surfactant-based flooding. In this experiment, there is no direct determination of oil

connectivity on a pore scale during flooding. Accordingly, oil production remains more effective before reaching the final water-dominated stage of the process.

Figure 10c shows that the differential-pressure response for CEOR is lower than that for baseline HSWF and marginally lower than that for the best-performing LSWF for most of the displacement process.

The baseline case reaches the maximum pressure level, which is consistent with the strong two-phase flow resistance during the water invasion into oil-filled pores. The best-performing LSWF case reduces the pressure response as compared with HSWF, while the 0.5 wt% AOS case shows the lowest mean peak differential pressure among the tested AOS concentrations. This indicates that the best-performing surfactant concentration improved oil mobilization without an unfavorable increase in flow resistance. The lowered pressure response is consistent with the reduced oil–water interfacial tension, improved phase redistribution and reduced capillary resistance to oil flow through pore throats.

From the mechanistic point of view, the effect of CEOR differs from that of LSWF on the capillary trapping phenomenon. Low-salinity waterflooding can modify the rock–brine–oil interactions and, consequently, may change the wettability-related endpoint of the imbibition. In turn, surfactant flooding reduces the interfacial tension between oil and water and, therefore, the capillary pressure needed to mobilize the trapped oil. According to the capillary-number concept, a lower IFT increases the ratio of viscous to capillary forces. As quantified in Section 4.2, however, the increase achieved with 0.5 wt% AOS was approximately one order of magnitude and remained below the level required for substantial mobilization of disconnected residual oil in sandstones. The CEOR benefit is therefore attributed mainly to reduced capillary trapping during the displacement of initially continuous oil rather than to the remobilization of established residual-oil ganglia.

Thus, the improvements obtained in this study by using CEOR may be interpreted as a reduction in the strength of capillary trapping caused by hysteresis. The best-performing AOS concentration was 0.5 wt%, which is practically relevant for the tested system. The lower concentration of the surfactant may not provide sufficient reduction of interfacial tension and oil mobilization, while the higher one may not improve recovery and may increase the costs and other problems related to chemicals.

Therefore, the best-performing surfactant design is not the most concentrated, but the one providing the most favorable combination of oil mobilization and recovery improvements and injectivity. For this experiment, 0.5 wt% AOS in 7600 ppm brine provides this combination.

To sum up, AOS-assisted CEOR shows an additional benefit of surfactant flooding after the optimization of salinity. The final recovery factor increases from 61.31 $\pm$ 5.69% OOIP for 7600 ppm LSWF to 69.30 $\pm$ 6.32% OOIP for CEOR, while the residual oil saturation decreases from 28.52 $\pm$ 3.36% PV to 22.60 $\pm$ 4.00% PV. The dynamic behavior of recovery, water cut, pressure and normalized phase-flow indices is consistent with the mechanism of improvement of displacement efficiency by reduction of IFT-related capillary trapping and better oil mobility during the imbibition. Thus, the CEOR with AOS is the second method of hysteresis control in this study that can be compared with the N_2-WAG experiments discussed in the following section.

3.4. WAG Performance and Cyclic Hysteresis Behavior (Results)

The N_2-WAG data were obtained from separate coreflood tests using new specimens subjected to the required sample preparation procedure and restoration of their wetting characteristics and core-specific water and oil saturations. Accordingly, the WAG recovery curve starts from the beginning of the N_2-WAG experiment and is not an extension of the HSWF, LSWF, or AOS-assisted CEOR recovery curves. The mean cumulative recovery

factors were 53.89 ± 4.93%, 66.63 ± 5.77%, 70.64 ± 5.95%, and 72.39 ± 6.03% OOIP at Cycles 1, 2, 3, and 4, respectively, and rose to 73.06 ± 6.23% OOIP at the end of the low-salinity brine injection. These values indicate the cumulative recovery of oil in the N_2-WAG experiments and do not represent incremental recovery following any preceding CEOR treatment.

Each N_2-WAG run was executed with a 1:1 gas-to-liquid ratio using alternating slugs of 7600 ppm low-salinity brine and nitrogen gas. A total of four complete WAG cycles were carried out, each comprising a 0.20 PV nitrogen slug followed by a 0.20 PV brine slug, followed after four cycles by a 0.40 PV low-salinity-brine chase to achieve a total injection of 2.00 PV. Throughout the process, produced oil, produced water, outlet-gas response, and differential pressure were measured. The injection of alternating gas and water slugs resulted in repeated changes in both the phase occupancy and the saturation direction during drainage and imbibition processes within the N_2-WAG coreflood experiment. Details on the procedure and conditions used during the experiment are given in the methodology section.

Cycle-wise cumulative recovery and stage-wise recovery responses obtained from N_2-WAG experiments are shown in Figure 11. On average, for the seven experiments performed, the cumulative recovery factors were 53.89 ± 4.93%, 66.63 ± 5.77%, 70.64 ± 5.95%, and 72.39 ± 6.03% OOIP after Cycles 1–4, respectively, and rose to 73.06 ± 6.23% OOIP after the final low-salinity brine chase. The stage-wise recovery contributions for Cycles 1–4 were 53.89 ± 4.93, 12.74 ± 0.87, 4.01 ± 0.20, and 1.74 ± 0.10%, and in the final chase, the contribution was 0.67 ± 0.35%. The residual oil saturation at the end of the experiment was 19.82 ± 4.01% PV. The relatively large contribution seen in Cycle 1 is associated with oil displacement from an independently set initial state and cannot be considered incremental recovery following HSWF, LSWF, or AOS-assisted CEOR.

To separate the strong early N_2-WAG response from the contribution of later saturation-history effects, Cycle 1 was compared with the waterflood histories at equal cumulative injected volume. The N_2-WAG cycle achieved a 0.40 PV total recovery of 53.89 ± 4.93% OOIP, compared to 40.23 ± 4.10% for the corresponding HSWF and 49.63 ± 4.89% for the 7600 ppm LSWF. The waterflood values at 0.40 PV were obtained by interpolating each core recovery value individually from the measured recovery curves between adjacent data points. Therefore, Cycle 1 exceeded the HSWF and 7600 ppm LSWF cases by 13.66% and 4.26%, respectively, at the 0.40 PV injection volume. Because Cycle 1 started from the specified initial oil–water saturation state and consisted of 0.20 PV N_2 followed by 0.20 PV brine, the large early recovery is attributed mainly to immiscible gas drainage and redistribution together with brine displacement.

Another comparison was made on the basis of cumulative injected liquid volume. The HSWF and 7600 ppm LSWF reached 51.96 ± 5.30% and 60.40 ± 5.95% OOIP, respectively, at 1.20 PV liquid injection. The final N_2-WAG response reached 73.06 ± 6.23% OOIP at 1.20 PV liquid injection together with 0.80 PV injected N_2. This comparison is normalized on the basis of cumulative liquid volume but not on displacement history or equal total injected volume. Therefore, the interpretation of the later WAG response considers saturation hysteresis control through saturation reversals, three-phase redistribution, gas trapping, and altered flow paths; Cycle 1 recovery is not considered evidence of hysteresis control alone.

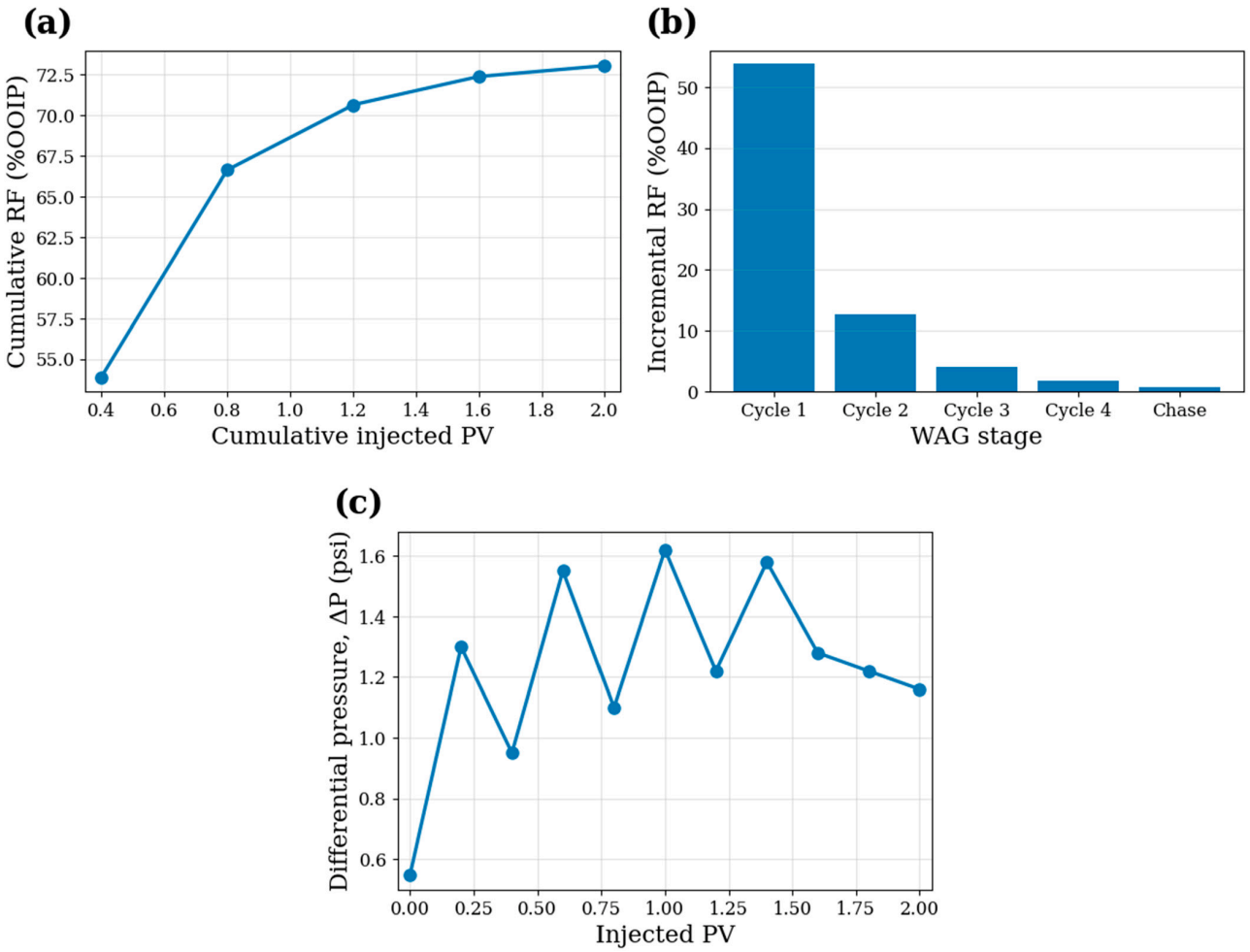


Figure 11. WAG cyclic displacement behavior: (**a**) cumulative recovery factor versus injected pore volume, (**b**) incremental recovery factor per WAG stage, and (**c**) differential pressure versus injected pore volume.

The contribution from stage-wise recovery was substantially reduced after the first two cycles, from 12.74 ± 0.87% in Cycle 2 to 4.01 ± 0.20% and 1.74 ± 0.10% in Cycles 3 and 4, respectively, and then to 0.67 ± 0.35% during the last brine flood. The decline in stage-wise recovery contribution occurred while cumulative recovery continued to increase, reaching 73.06 ± 6.23% OOIP at 2.0 PV.

Figure 11c depicts the differential pressure behavior recorded during the cyclic N_2-WAG test. The differential-pressure curve exhibits recurring oscillations throughout the cyclic process rather than a monotonic response. These oscillations reflect repeated changes in hydraulic resistance during the WAG stages. The pressure increases and decreases cannot be attributed solely to gas- or brine-dominated flow because gas compressibility, saturation-dependent mobility, and three-phase interference also contribute. The pressure response should therefore be interpreted together with the injection sequence. The cyclic variation in differential pressure is indicative of cyclic variations in hydraulic resistance and phase occupancy associated with alternating N_2–brine injection. Along with the cyclic recovery response, these results support a three-phase displacement scenario that depends on the history of saturation.

Table 9 summarizes the residual-oil-saturation responses for all seven N_2-WAG runs. The mean residual oil saturation decreased from 34.03 ± 2.65% PV after Cycle 1 to 24.59 ± 3.54%, 21.61 ± 3.76%, and 20.32 ± 3.86% PV after Cycles 2–4, respectively, and reached 19.82 ± 4.01% PV after the final low-salinity-brine chase. Breakthrough of

nitrogen was measured at about 0.281 pore volumes injected cumulatively within the first brine slug cycle. The measurement is consistent with gas communication through the outlet during Cycle 1 and implies that the significant early recovery includes immiscible gas displacement.

Table 9. WAG cycle recovery and residual oil saturation response.

Cycle	Injection Medium	Cumulative Injected PV	Stage *RF* Contribution, %	Cumulative, *RF* % OOIP	Remaining, S_{or} Mean ± SD (% PV)
1	Slug of N_2 and LSWF	0.4	53.89 ± 4.93	53.89 ± 4.93	34.03 ± 2.65
2		0.8	12.74 ± 0.87	66.63 ± 5.77	24.59 ± 3.54
3		1.2	4.01 ± 0.20	70.64 ± 5.95	21.61 ± 3.76
4		1.6	1.74 ± 0.10	72.39 ± 6.03	20.32 ± 3.86
Final Chase	7600 ppm brine	2.0	0.67 ± 0.35	73.06 ± 6.23	19.82 ± 4.01

Figure 11 shows the recovery and differential-pressure responses during N_2-WAG. The recovery graph shows that the maximum increase occurred in the earlier WAG cycles, followed by smaller increments at later stages.

3.5. Comparative Evaluation of All Displacement Methods

The displacement processes were compared at a standardized endpoint of 2.0 PV injected. The average values of recovery factors recorded were 53.15 ± 5.42% OOIP for HSWF, 61.31 ± 5.69% OOIP for 7600 ppm LSWF, 69.30 ± 6.32% OOIP for 0.5 wt% AOS-assisted CEOR and 73.06 ± 6.23% OOIP for N_2-WAG. The corresponding average residual oil saturations were 34.57 ± 2.99%, 28.52 ± 3.36%, 22.60 ± 4.00% and 19.82 ± 4.01% PV, respectively.

The values presented in Table 10 are the recovery-factor endpoints and the parent-core-matched differences relative to HSWF for the four different treatments. Listing the C1–C7 values separately makes the basis of the paired analysis clearer and helps distinguish the spread of the matched treatment differences from the spread of the treatment endpoints themselves.

Table 10. Final average recovery factor and residual oil saturation for all displacement methods.

Method	Final, *RF* Mean ± SD (% OOIP)	Final, S_{or} Mean ± SD (% PV)	Endpoint Difference from HSWF, %
HSWF	53.15 ± 5.42	34.57 ± 2.99	-
LSWF	61.31 ± 5.69	28.52 ± 3.36	8.17
CEOR	69.30 ± 6.32	22.60 ± 4.00	16.15
WAG	73.06 ± 6.23	19.82 ± 4.01	19.91

The core-level analyses suggest that the relatively small standard deviations of the matched treatment differences are largely due to the consistency of the within-source treatment effects rather than to exceptionally low variability of the treatment endpoints themselves. The mean paired recovery-factor differences were 8.17 ± 0.33 percentage points for 7600 ppm LSWF, 16.15 ± 0.94 percentage points for 0.5 wt% AOS-assisted CEOR, and 19.91 ± 0.85 percentage points for N_2-WAG. The corresponding 95% confidence intervals were 7.86–8.48, 15.28–17.03, and 19.13–20.70 percentage points, respectively. For the two-

sided exact Wilcoxon signed-rank tests applied to the seven parent-core-source-matched pairs, the unadjusted p value was 0.015625 for each of the three prespecified comparisons with HSWF. After Holm adjustment for three comparisons, the adjusted p value was 0.046875 for each comparison. Therefore, the statistical analysis is based on the seven individual matched differences rather than on simple differences between treatment means.

Experimental repeatability was further examined using independent duplicate coreflloods for the 7600 ppm LSWF and 0.5 wt% AOS-assisted CEOR conditions (Table 11).

Table 11. Independent duplicate coreflood repeatability results for the selected 7600 ppm LSWF and 0.5 wt% AOS-assisted CEOR conditions.

Condition	Duplicate Run	Final RF (%OOIP)	Final S_{or} (% PV)	Peak ΔP (psi)
7600 ppm LSWF	Duplicate A	66.10	25.76	1.00
7600 ppm LSWF	Duplicate B	66.48	25.48	0.97
0.5 wt% AOS-assisted CEOR	Duplicate A	69.75	22.99	1.20
0.5 wt% AOS-assisted CEOR	Duplicate B	70.20	22.65	1.23

The duplicate coreflood tests showed remarkable consistency under both selected operating conditions. For 7600 ppm LSWF, the final recovery factors were 66.10% and 66.48% OOIP, representing an absolute difference between runs of 0.38 percentage points. The final residual oil saturations were 25.76% and 25.48% PV, whereas the peak differential pressures were 1.00 and 0.97 psi. For 0.5 wt% AOS-assisted CEOR, the final recovery factors were 69.75% and 70.20% OOIP, representing an absolute difference between runs of 0.45 percentage points. The final residual oil saturations were 22.99% and 22.65% PV, whereas the peak differential pressures were 1.20 and 1.23 psi, respectively. Close agreement was also evident in the recovery-factor and differential-pressure histories for each duplicate pair.

Each treatment was made up of seven experiments performed independently, each using parent-core-matched samples. The differences from HSWF shown below are those between treatments at the endpoint; they are not cumulative recovery gains obtained through an HSWF–LSWF–CEOR–WAG sequence. All four treatments were tested at the same total injection volume of 2.0 PV.

The differences from HSWF using the mean of the unrounded values are 8.17% for 7600 ppm LSWF, 16.15% for 0.5 wt% AOS-assisted CEOR, and 19.91% for N_2-WAG. The endpoint difference between N_2-WAG and AOS-assisted CEOR is 3.76%.

Figure 12 shows an overall comparison of the four displacement treatments. To compare displacement responses on a common injected-volume basis, HSWF, 7600 ppm LSWF, 0.5 wt% AOS-assisted CEOR, and N_2-WAG were evaluated over the same 0–2.0 PV range (Figure 12c). This ensures comparison at equal cumulative injected pore volume. The recovery profiles differed during the main displacement stage and converged toward their respective endpoints. HSWF approached its recovery plateau earlier, whereas the 7600 ppm LSWF, AOS-assisted CEOR, and N_2-WAG profiles remained higher at the same injected PV. The recovery profile of CEOR was higher than those of HSWF and LSWF at approximately 0.5 PV. The common-PV comparison removes differences in total injected volume but does not remove the effect of specimen heterogeneity. In addition to the common 2.0 PV endpoint comparison, the N_2-WAG Cycle 1 response at 0.40 PV was compared with the corresponding HSWF and 7600 ppm LSWF histories. This comparison helps distinguish the strong early WAG displacement from effects associated with subsequent cyclic changes in saturation history.

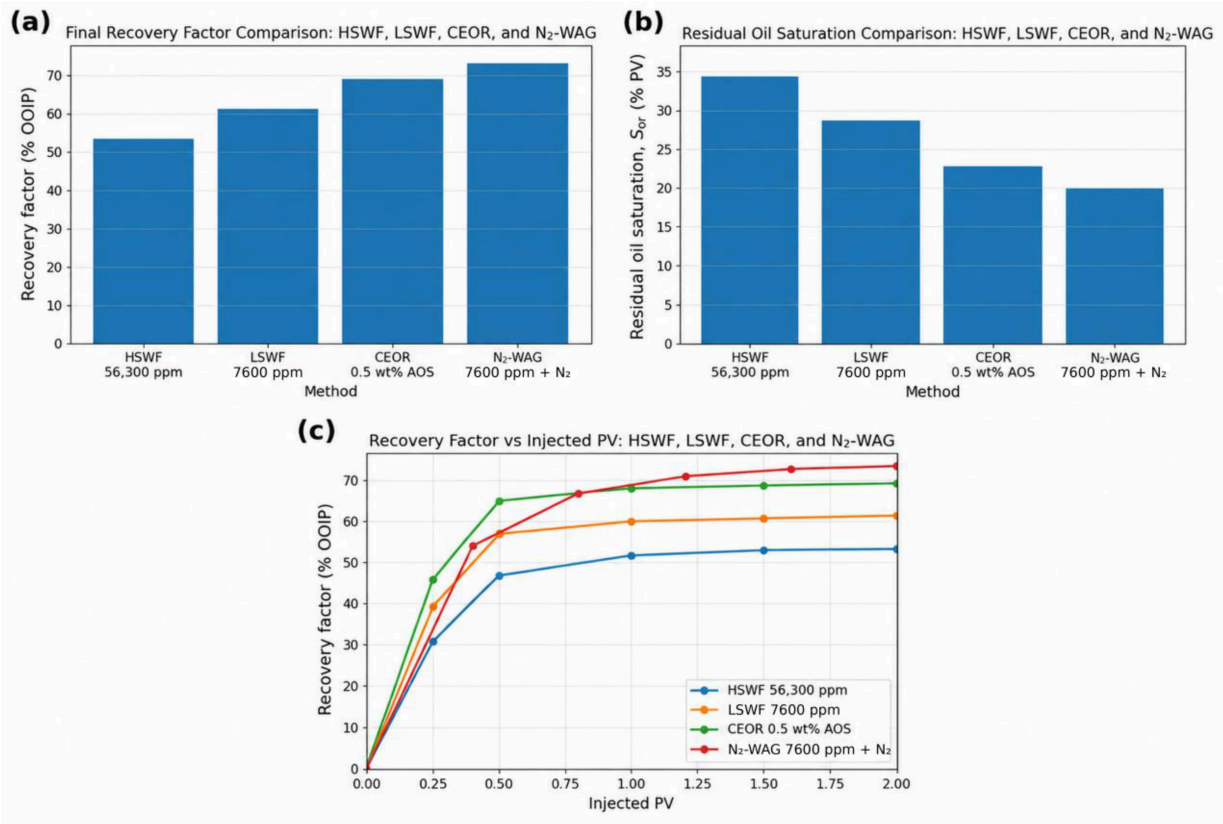


Figure 12. Overall comparison of displacement methods: (**a**) final recovery factor, (**b**) final residual oil saturation, and (**c**) recovery factor versus injected pore volume for HSWF, the best-performing tested LSWF, AOS-assisted CEOR, and WAG.

To directly address equivalent-basis comparisons, recovery performance was tested using equivalent total fluid volume injection, equivalent cumulative fluid volume, and the equivalent 2.00 PV treatment point, as shown in Table 12.

Table 12. Equal-total-PV, equal-liquid-volume, and common-endpoint recovery comparison for HSWF, 7600 ppm LSWF, and N_2-WAG.

Comparison Basis	HSWF, % OOIP	7600 ppm LSWF, % OOIP	N_2-WAG, % OOIP
0.40 PV total injected	40.23 ± 4.10	49.63 ± 4.89	53.89 ± 4.93
1.20 PV cumulative liquid	51.96 ± 5.30	60.40 ± 5.95	73.06 ± 6.23 *
2.00 PV treatment endpoint	53.15 ± 5.42	61.31 ± 5.69	73.06 ± 6.23

* For N_2-WAG, 1.20 PV of cumulative liquid injection was accompanied by 0.80 PV of N_2 injection, giving a total injected volume of 2.00 PV. This comparison uses equal liquid volumes, not equal total injected volumes.

Under the equal-liquid-volume comparison, the N_2-WAG test showed a cumulative liquid volume of 1.20 PV with 0.80 PV of N_2. Hence, this comparison assumes equal liquid volumes, but not equal total injection volumes or history. The HSWF and 7600 ppm LSWF recovery values at 0.40 and 1.20 PV were obtained by linear interpolation between adjacent measured points on each individual core's recovery curve.

3.6. Rate Sensitivity and Capillary-End-Effect Assessment

The experiments show that increasing the liquid injection rate produced only small changes in the displacement endpoint relative to the reference rate of 0.30 mL/min. On average, the recovery factor was 50.20% OOIP at 0.15 mL/min, 51.67% OOIP at 0.30 mL/min, and 52.00% OOIP at 0.60 mL/min, whereas the corresponding average residual oil saturation was 36.42%, 35.34%, and 35.09% PV, respectively. At the same time, the average differential pressure changed from 0.84 psi at 0.15 mL/min to 1.60 psi at 0.30 mL/min and 3.10 psi at 0.60 mL/min. Mean endpoint water cut remained similar at 97.97%, 97.43%, and 97.23%, respectively. Increasing the rate from 0.30 to 0.60 mL/min increased the mean recovery factor by 0.33% and reduced the mean residual oil saturation by 0.25%, despite the doubling of differential pressure. Hence, endpoint sensitivity was limited, suggesting that the reference rate of 0.30 mL/min was not strongly affected by rate-dependent capillary-end effects within the tested range. The complete results and rate-dependent responses are provided in Table A1 and Figure A3.

3.7. Direct Capillary-Pressure Hysteresis and Rock–Fluid Response

The $P_c - S_w$ curve generated for the C1-parent sandstone system through the $P_c - S_w$ experiment demonstrates clear evidence of the existence of the path-dependent nature of the capillary pressure. The primary drainage and primary imbibition branches are not coincident in the observed saturation range. At S_w = 0.60, the interpolated capillary pressures for primary drainage and main imbibition are 2.12 psi and 0.90 psi, respectively, with a branch separation of 1.21 psi. At S_w = 0.50, the drainage–imbibition separation is 1.22 psi. The finite area under the primary branches for S_w = 0.26–0.82 is about 0.61 psi·S_w.

The internal hysteresis created through the starting point of the main imbibition route at S_w = 0.60 formed a unique scanning path. The partial drainage process decreased S_w to 0.43, and then the re-imbibition continued to S_w = 0.68 without following any of the primary routes. The non-simultaneous nature of the primary routes and the scanning path formed due to hysteresis directly demonstrates the history dependence of the $P_c - S_w$ relationship in the studied C1-parent sandstone–brine–oil system. Since this verification test was performed on one particular core from the parent cores, the $P_c - S_w$ loop is not a generalized hysteresis function for all seven parent cores.

Additional contact-angle measurements using the captive-drop method revealed a slight change following the Pc cycle. Measurements at six locations showed that the mean contact angle decreased from 89.5 ± 1.9° before the cycle to 83.8 ± 1.5° after the cycle, with a mean paired difference of −5.7 ± 2.9° (Table A2, Appendix A). These results provide supporting evidence of a slight wettability change but are not used alone to establish capillary hysteresis.

Additional measurements of the dynamic oil–water interfacial tension were performed on the two principal fluids at the experimental temperatures. The stabilized interfacial tensions were 24.7 ± 0.2 mN/m for the 56,300 ppm HSWF brine, 22.5 ± 0.2 mN/m for the 7600 ppm brine, and 2.65 ± 0.10 mN/m for 0.5 wt% AOS in 7600 ppm brine. Hence, the AOS formulation showed a one-order-of-magnitude lower oil–water IFT compared to both surfactant-free brines.

As the interfacial tension (IFT) measurement results were incorporated into the revised capillary number model in combination with fluid-specific viscosities, the flow-based capillary number grew from 4.81×10^{-8} under the 7600 ppm LSWF injection conditions to 4.52×10^{-7} under the 0.5 wt% AOS-assisted CEOR, constituting approximately a 9.4-fold increase. Similarly, the pressure-gradient form of the capillary number increased from 2.87×10^{-7} to 2.30×10^{-6}, which is about an 8.0-fold increase. However, the flow-based capillary numbers of HSWF and LSWF stayed within the 10^{-8} range.

4. Discussion

4.1. Interpretation of Displacement Responses

These independent studies examine the impact of fluid formulation and injection strategy on capillary trapping and displacement processes that depend on saturation state. In all the experiments conducted under the varied conditions, a lower residual oil saturation was observed for the 7600 ppm LSWF, 0.5 wt% AOS-assisted CEOR, and N_2-WAG treatments compared with the HSWF reference, with N_2-WAG showing the lowest recorded mean residual-oil saturation. The differences in these treatment-dependent endpoints can be attributed to differences in displacement environment and saturation history but should not be interpreted as a sequential HSWF–LSWF–CEOR–WAG process.

The HSWF served to create a benchmark for displacement and residual trapping for comparison with the other treatments. Brine injection with a 56,300 ppm concentration resulted in the occurrence of forced-imbibition-type displacement, whereby the recovery first increases before eventually leveling out (Figure 2a). Such behavior has been attributed to the gradual decrease in the connected mobile oil phase and an increased tendency for residual capillary trapping. The parallel increase in water cut (Figure 2b) and the observed changes in the normalized phase-flow response (Figure 3) further indicate the transition toward water-dominated flow and the HSWF residual-oil endpoint.

The HSWF residual trapping state holds significance for the hysteretic approach owing to the fact that the multiphase flow may be dependent on the saturation history. According to the hysteretic approach, the same saturation point may have different phase-flow responses based on how the same saturation point is achieved in terms of drainage, imbibition, or scanning process. The HSWF experiment involves a core material having a relatively higher oil saturation level, followed by displacement of 56,300 ppm of brine to form a type of forced imbibition residual state. The mean value of 34.57 $\pm$ 2.99% PV for residual oil saturation forms the basis for the comparison with other treatment methods.

In the LSWF experiments, changes in brine salinity influenced the displacement response relative to HSWF. The results are shown in Table 6 and Figure 4, which demonstrate that with the salinity decrease from 56,300 ppm to the best-performing tested value of 7600 ppm, there is an increase in the average recovery factor from 53.15 $\pm$ 5.42% to 61.31 $\pm$ 5.69% OOIP and a decrease in the mean residual oil saturation from 34.57 $\pm$ 2.99% to 28.52 $\pm$ 3.36% PV. Thus, the residual-oil endpoint was sensitive to both pore structure and brine composition under the tested conditions. The improved response at 7600 ppm is consistent with the salinity dependence of mineral–brine–oil interactions in the feldspar-clay rocks.

A hysteresis-based interpretation suggests that the LSWF response reflects a shift in residual trapping during imbibition compared to the reference HSWF curve. There are various explanations of how low salinity can influence residual oil trapping, such as changes in wettability conditions due to the salinity effect on electrostatic surface charge, film-forming properties, and so on. These factors have an impact on oil connectivity but were not observed directly during this investigation. Figure 5a shows the best low-salinity response at 7600 ppm. The higher LSWF recovery factor and lower residual oil saturation relative to HSWF are consistent with reduced residual trapping.

The salinity effect on recovery and pressure drop was evaluated to identify the best-performing condition. However, contrary to expectations, the dependence of these indicators on salinity value showed non-monotonic behavior. With dilution below the best-performing tested salinity of 7600 ppm, particularly 3000 and 1000 ppm, recovery decreased along with rising differential pressure. Experimental data confirmed that deteriorated reservoir properties coincided with higher sensitivity to fluid flow. The concentration of solid particles in the effluent increased sharply upon further dilution. Further dilutions increased linear swelling, but the single-phase brine tests demonstrated lower permeability

retention values. Comparison of micro-CT scan images taken prior to and after flooding revealed that the number of resolved pores in the area of interest was reduced at 3000 ppm. These observations suggest that swelling and fines migration contribute to pore-throat restriction under low-salinity conditions.

Displacement problems addressed by AOS-assisted CEOR were different from those addressed by LSWF. While salinity-dependent rock–brine–oil interactions affected the LSWF results, improved performance of AOS-assisted CEOR was due to reduction of interfacial and capillary resistance to oil mobilization. Among the tested surfactant concentrations, the best results were achieved with 0.5 wt% AOS. This surfactant mixture reached a mean final recovery of 69.30 ± 6.32% OOIP and a mean residual oil saturation of 22.60 ± 4.00% PV (Table 8 and Figure 8). Compared with the 7600 ppm LSWF reference, the lower residual-oil endpoint of this additional mobilization, in the presence of a surfactant, was consistent with an additional mobilization effect.

Figure 9 provides an additional qualitative comparison based on the normalized phase-flow indices. The CEOR case shows a larger normalized oil-flow contribution over part of the investigated water-saturation range and a later transition toward water-dominated flow than HSWF and 7600 ppm LSWF. These indices are calculated from unsteady-state production and differential-pressure data and therefore should be interpreted only together with recovery factor, residual oil saturation, water cut, and differential pressure. They are not constitutive relative-permeability curves and are not used as evidence of intrinsic phase-mobility enhancement.

The dynamic displacement responses give additional support to the CEOR interpretation. The recovery for the 0.5 wt% AOS-assisted CEOR experiment (in Figure 10a) is higher than for the HSWF and 7600 ppm LSWF experiments for most of the displacement and ends at the highest endpoint value. The associated water cut in Figure 10b gives an indication of the contribution of oil production in the early stages of the experiment before it becomes predominantly water. Figure 10c indicates that the selected 0.5 wt% AOS treatment achieved a higher recovery without an associated increase in differential pressure.

Of the examined methods, N_2-WAG was the most explicit method for repeated changes in saturation history. Alternating between gas injection and brine injection formed a cyclic process with repeated instances of drainage and imbibition. The N_2-WAG sequence generated a series of drainage- and imbibition-type reversals. Mechanisms underlying gas trapping, flow path diversion, and oil connectivity modification appear logically consistent with the cyclic production response, decreasing residual oil saturation, and cyclic differential pressure dynamics.

Quantitative cycle-wise information is provided in Table 9 and in Figure 11. The mean cumulative recovery increased from 53.89 ± 4.93% OOIP for Cycle 1 to 66.63 ± 5.77% OOIP, 70.64 ± 5.95% OOIP, and 72.39 ± 6.03% OOIP for Cycles 2–4, respectively. After the final low-salinity-brine chase, recovery reached 73.06 ± 6.23% OOIP. The stage-wise recovery contribution decreased with each subsequent cycle. The oscillation of differential pressure for alternating injection of gas and brine is also visible in Figure 11c, indicating variations in hydraulic resistance and saturation-dependent flow behavior.

The decline in the stage-wise contribution can be examined more specifically by relating each increment to the oil that remained in place at the beginning of the corresponding stage. On the basis of the mean values in Table 9, Cycle 2 recovered approximately 27.6% of the oil remaining after Cycle 1, whereas Cycles 3 and 4 and the final brine chase recovered approximately 12.0%, 5.9%, and 2.4% of the oil remaining at the beginning of each stage, respectively. Hence, the displacement efficiency of successive stages decreased considerably faster than the volume of oil remaining in the core, and the mean residual oil saturation approached an apparent limit of approximately 20% PV (from 34.03 ± 2.65% PV after

Cycle 1 to 19.82 ± 4.01% PV after the final chase). This indicates that the marginal effect of the later cycles was limited primarily by the decreasing fraction of oil that remained hydraulically connected and displaceable, rather than by the total amount of oil left in the core.

Two pore-scale processes are consistent with this trend. First, the repeated drainage–imbibition reversals progressively ruptured the continuity of the oil phase. At the beginning of Cycle 1, the oil was continuous at the restored initial saturation, and the injected N_2, as the non-wetting and much less viscous phase, displaced oil along the larger connected pores. Each subsequent brine slug re-invaded the pore throats and disconnected part of the remaining oil into isolated ganglia and thin layers [1,37], so that every further reversal reduced the fraction of oil connected to the outlet. Once disconnected, an oil ganglion can be remobilized only when the local viscous pressure drop across it exceeds the capillary pressure difference that retains it. Because the capillary numbers of both the aqueous and the gas slugs were on the order of 10^{-9}–10^{-8} (Section 4.2; Table 13), well below the critical range for mobilizing discontinuous oil, the capillary retention of the disconnected oil increasingly dominated the response of the later cycles. Second, gas trapping accumulated during the brine half-cycles. When brine re-invades gas-occupied pores, part of the gas is trapped as a disconnected residual phase; the trapped gas saturation increases with the maximum gas saturation previously reached but approaches a limiting value [38]. In the early cycles, newly trapped gas occupied the larger pores, reduced the aqueous-phase mobility, and diverted the subsequent brine and gas toward oil-bearing pores that had not yet been swept, which contributed to the comparatively large increment of Cycle 2 [5,6,37]. As the trapped gas saturation approached its limiting value, the later cycles produced progressively smaller changes in pore occupancy, and the injected N_2, which had broken through at approximately 0.281 PV, increasingly flowed along the established gas pathways and contacted less oil. Together, the progressive depletion of the continuous, flowable oil phase and the approach of gas trapping to its limit explain the decline of the stage-wise contribution from 12.74 ± 0.87% in Cycle 2 to 1.74 ± 0.10% in Cycle 4 and 0.67 ± 0.35% in the final chase.

Table 13. Capillary number screening performed using experimentally determined oil–water IFT and fluid-specific aqueous viscosity values at 70 °C.

Treatment	$N_c^{(\Delta P)}$	$N_c^{(q)}$	Measured Oil–Water IFT, Mean ± SD (mN/m)	Representative Peak ΔP (psi)	μ_d at 70 °C (cP)
HSWF, 56,300 ppm	3.36×10^{-7}	4.70×10^{-8}	24.7 ± 0.2	1.66	0.470 ± 0.003
The best-performing LSWF, 7600 ppm	2.87×10^{-7}	4.81×10^{-8}	22.5 ± 0.2	1.29	0.438 ± 0.003
0.5 wt% AOS-assisted CEOR	2.30×10^{-6}	4.52×10^{-7}	2.65 ± 0.10	1.22	0.485 ± 0.005
N_2-WAG aqueous-slug reference	Not assigned	4.81×10^{-8}	22.5 ± 0.2	Cyclic	0.438 ± 0.003
N_2-WAG gas-slug bound	Not assigned	2.6×10^{-9}–1.3×10^{-8}	5–25 (assumed gas–oil range)	Cyclic	0.026 (N_2)

Note: Capillary numbers were calculated from Equations (17)–(19) using u = 2.47×10^{-6} m/s, k = 2.21×10^{-13} m^2, and L = 0.3048 m. For the N_2 slugs, μ_d is the N_2 viscosity at 70 °C and approximately 4000 psi, calculated from [35,36]; the gas–oil IFT was not measured, and a range of 5–25 mN/m was assumed to obtain an order-of-magnitude bound.

These interpretations are consistent with the measured recovery, residual-oil-saturation, gas-breakthrough, and differential-pressure responses. However, the gas saturation, trapped gas saturation, and pore-scale phase distribution were not measured during the corefloods; therefore, the relative contributions of oil-phase disconnection and gas trapping could not be quantified separately.

Among the tested cases, N_2-WAG yielded the lowest average residual oil saturation, 19.82 ± 4.01% PV, as opposed to 22.60 ± 4.00% PV in 0.5 wt% AOS-assisted CEOR. The lower residual oil endpoint seen for N_2-WAG can be attributed to the effects of the gas–brine displacement, saturation-history changes, phase redistribution, gas trapping, and flow path changes.

The equal-PV comparison indicates that the large recovery in Cycle 1 cannot be entirely explained by the effect of cyclic hysteresis. At 0.40 PV total injected volume, N_2-WAG already gave higher recovery than the corresponding HSWF and 7600 ppm LSWF, implying an important contribution of early displacement via the N_2–brine combination. Gas breakthrough measurements in Cycle 1 support the involvement of gas displacement at the early stage of the process. Thus, the understanding of subsequent cycles should involve saturation cycling, three-phase redistribution, gas entrapment, and flow path alteration instead of hysteresis control only.

Figure 12 illustrates the differences among treatments at the common end point of 2.0 PV. The mean recovery factor showed an increasing trend, while the mean residual oil saturation demonstrated a decreasing tendency in the following order: HSWF, 7600 ppm LSWF, 0.5 wt% AOS-assisted CEOR, and N_2-WAG. These differences are consistent with treatment-related effects of brine salinity, surfactant-induced displacement process, and cyclic gas–brine injection.

The repeatability-confirmation experiments help distinguish between two sources of experimental variability in this study. The standard deviations observed for the primary treatment endpoints reflect variations attributable to independently prepared specimens matched to the parent core, together with run-to-run experimental variability. On the other hand, the duplicate tests allow repeatability to be evaluated under fixed treatment conditions. The absolute differences in final recovery between duplicate runs were 0.38 and 0.45 percentage points for the 7600 ppm LSWF and 0.5 wt% AOS-assisted CEOR conditions, respectively, together with similarly small differences in peak differential pressure. Therefore, the narrow distributions of the matched parent-core treatment differences should not be interpreted as instrument precision or as technical repeatability by themselves.

An advantage of the current study is the comparison of multiple displacement methods within a common core-scale approach focused on residual oil trapping and the influence of history of saturation. While LSWF, surfactant flooding, and WAG represent well-known EOR techniques, the corresponding responses were evaluated using a common set of data on recovery, residual oil saturation, water cut, differential pressure, and phase flow. This approach enables comparison of the responses without implying a sequential HSWF–LSWF–CEOR–WAG application.

Another important observation is that the maximum recovery of LSWF took place at 7600 ppm rather than the lowest value of salinity studied, whereas 0.5 wt% AOS worked better than 1.0 wt% of the same compound. The differential-pressure responses further show that recovery should be considered together with changes in hydraulic resistance and process stability. In particular, the lower recovery at the lowest salinities correlated with the production of more solids, swelling, reduction in permeability, and an increase in the differential pressure, whereas the cyclic behavior of the N_2-WAG differential pressure responded to the alternating resistance changes due to gas–brine injection. These results suggest that the proper approach is to optimize, not necessarily increase, treatment intensity,

because differential pressure is a diagnostic response rather than a direct measure of the capillary-hysteresis function.

4.1.1. Evidentiary Scope and Limitations

Capillary trapping and the influence of saturation history in this study were interpreted using the responses related to the recovery factor, residual oil saturation, water cut, differential pressure, normalized phase-flow indices, and injection histories. Relative to HSWF, higher recoveries and lower residual oil saturations were observed for 7600 ppm LSWF, 0.5 wt% AOS-assisted CEOR, and N_2-WAG.

Further confirmation of the non-monotonic salinity trend for the low-salinity experiments was obtained with additional measurements of effluent-solids production, linear swelling, and single-phase brine-permeability retention. These data, together with pre-/post-flood micro-CT observations from one specimen at 3000 ppm, support the interpretation of higher differential pressure and lower recovery at the lower salinities. The data presented for 3000 ppm and 1000 ppm suggest that swelling and fines migration could contribute to pore-space restriction and subsequent hydraulic impairment. However, the quantity and distribution of retained fines, as well as the relative contribution of swelling and deposition, were not individually assessed, and the results of micro-CT analysis were based on only one specimen at 3000 ppm rather than the complete experimental population.

Other mechanistic explanations remain interpretative because the corresponding measurements were not conducted during flooding. The measurements made prior to flooding verified the restored initial wettability condition but cannot demonstrate dynamic wettability changes during LSWF, CEOR and N_2-WAG. In the case of the AOS system in 7600 ppm brine, the CMC was independently determined through the measurement of the air–solution surface tension. However, the following factors were not investigated during the coreflood studies: interfacial tension dynamics, retention behavior, effluent surfactant concentrations, solution rheology, phase equilibrium, micelle/aggregate size distribution, and three-phase pore-scale fluid distribution. Therefore, while the determined CMC identifies the concentration domain, it does not by itself confirm the oil–water interfacial process during CEOR. Hence, the LSWF response is consistent with salinity-dependent rock–brine–oil interactions, the CEOR response with reduced interfacial and capillary resistance, and the N_2-WAG response with repeated saturation-history modification and gas trapping.

Future work should combine the current coreflood approach with pre- and post-wetting contact angle measurement, interfacial tension measurement, drainage–imbibition capillary pressure and relative permeability scans, effluent-ion analysis, surfactant retention, and gas trapping, along with pore imaging studies. Such measurements will enable the separation of the individual effects of wetting changes, interfacial effects, geochemistry, fines transport, swelling, and three-phase saturation history.

4.1.2. Interpretation of the Non-Monotonic Salinity Response

The relationship between the salinity and the displacement performance followed a non-monotonic behavior. A reduction in the salinity value down to 7600 ppm contributed to an improvement in the displacement process, but at the same time, any additional reduction in the salinity to 5000–1000 ppm resulted in a lower recovery factor and higher residual oil saturation. This effect became especially noticeable at 3000 and 1000 ppm salinity.

The reduction in recovery and increase in differential pressure at the lower salinities suggest increasing impairment rather than simply the absence of a low-salinity benefit. The validation results support this interpretation. For the two lower salinities, effluent solid formation increased significantly, single-phase permeability retention was reduced, and linear swelling was greater for the two lower salinities compared to the 7600 ppm salinity. Moreover, the representative micro-CT imaging analysis before and after flooding of the core specimen at 3000 ppm showed a decrease in the resolved pore regions in the selected region of interest. Based on these findings, swelling and migration of fines are processes that could contribute to the restriction of pore throats under more diluted conditions.

One possible explanation is that a higher degree of dilution made the clay-containing sandstone more susceptible to the interaction between brine and minerals, causing expansion of the clay and mobilization of particles. These mobilized particles may partly obstruct the pores and decrease the permeability of the formation. This may offset the favorable displacement response observed at moderate salt concentrations. However, there are no data on the individual role of swelling, detachment, retention, and deposition of fines, and the micro-CT analysis is limited to C1 at 3000 ppm. Dynamic changes in wettability and ion exchange processes were also not measured directly and should therefore be treated as interpretations rather than experimentally validated processes.

Thus, 7600 ppm should be considered the best-performing salinity under the test conditions for the particular sandstone–crude oil–brine system. It cannot be viewed as the universal low-salinity limit or the optimal value for applicable rock-fluid systems.

4.2. Quantitative Capillary-Number Evaluation

The recalculated capillary number screening values are given in Table 13. The purpose of these computations is to quantify the change in the ratio of viscous to capillary forces associated with each treatment, based on the experimentally measured IFT and aqueous viscosity values, and to compare the resulting values with the critical capillary-number range reported for sandstones.

The recalculated capillary numbers are shown in Table 13. Based on directly measured values of oil–water interfacial tension (IFT), as well as aqueous viscosities of the tested fluids at 70 °C, the flow-based capillary numbers are 4.70×10^{-8} for HSWF, 4.81×10^{-8} for the best-performing tested 7600 ppm LSWF, and 4.52×10^{-7} for the 0.5 wt% AOS-assisted CEOR process. Thus, the HSWF and 7600 ppm LSWF cases remain in the same 10^{-8} order of magnitude, with only a small difference between them. The improvement in LSWF recovery therefore does not appear to result from a substantial change in the viscous-to-capillary force ratio. Instead, it is consistent with salinity-dependent changes in rock–brine–oil interactions and displacement behavior.

In turn, the corresponding pressure-gradient screening factors for HSWF, 7600 ppm LSWF, and AOS-assisted CEOR were 3.36×10^{-7}, 2.87×10^{-7}, and 2.30×10^{-6}, respectively. Compared to the 7600 ppm LSWF case, the AOS-assisted CEOR showed a 9.4-fold higher capillary number based on the flow rates and an 8.0-fold higher pressure-gradient screening factor. The increase is consistent with the experimentally measured reduction of oil–water interfacial tension to 2.65 ± 0.10 mN/m, not with an increase in either injection rate or differential pressure.

These calculations are retained as quantitative screening support and should not be considered proof of the existence of a universal critical capillary number limit. In the pressure gradient equation, absolute permeability is used in lieu of the saturation-dependent effective permeability, while in the flow equation, the superficial velocity is used; thus, both are to be considered as comparative values only, and not as pore-scale constitutive capillary numbers. More accurate results would require saturation-dependent effective phase permeabilities.

Although no universal critical value exists, comparison with the capillary desaturation behavior reported for sandstones provides a quantitative reference for assessing whether the CEOR treatment raised the capillary number sufficiently to mobilize capillary-trapped oil. For water-wet sandstones, the residual oil saturation remains approximately constant below a critical capillary number that is typically reported in the range of approximately 10^{-6}–10^{-5}, depending on the definition used [39]. Using the pressure-gradient form, Chatzis and Morrow reported that the mobilization of discontinuous residual oil began at approximately 2×10^{-5} and that its complete removal required approximately 1.5×10^{-3}. The flow-based capillary number of the 0.5 wt% AOS treatment (4.52×10^{-7}) remains below the lower limit of the reported critical range. The pressure-gradient value (2.30×10^{-6}), which is an upper-bound estimate because absolute rather than effective permeability is used, reaches only the lower part of this range; it is approximately one order of magnitude below the onset value reported by Chatzis and Morrow and almost three orders of magnitude below the value required for complete desaturation. Therefore, the AOS formulation increased the capillary number by approximately one order of magnitude relative to the 7600 ppm LSWF, but it did not raise it to a level at which substantial viscous mobilization of disconnected residual-oil ganglia would be expected. This result is consistent with the measured oil–water IFT of 2.65 ± 0.10 mN/m, which is far above the ultralow values commonly targeted in surfactant flooding [14].

The approximately 8.0-percentage-point higher mean recovery of CEOR relative to the 7600 ppm LSWF must therefore be explained by processes that do not require the critical capillary number to be exceeded. First, each CEOR experiment started from the restored initial oil saturation, so that the surfactant acted on initially continuous oil during the primary displacement rather than on an established residual saturation; Chatzis and Morrow showed that the capillary numbers required to displace continuous oil are lower than those required to mobilize discontinuous residual oil. A lower IFT during the displacement can therefore reduce the extent of oil disconnection and capillary trapping behind the displacement front. Second, the restored rock–fluid system was close to neutral wettability, as indicated by the contact angle of $89.5 \pm 1.9^{\circ}$ measured on the representative C1-HYS specimen (Section 3.7). For mixed-wet rock, the capillary desaturation curve has been shown to lack a distinct low-capillary-number plateau, with the remaining oil saturation decreasing gradually as the capillary number increases; a similar behavior can be expected for the near-neutral wettability of the present system. Third, the 2.0 PV endpoints represent remaining rather than ultimate residual oil saturations, as recovery continued to increase slightly between 1.8 and 2.0 PV in the duplicate runs (by 0.10–0.18 percentage points; Table A3). Additional surfactant-specific effects, such as wettability modification, solubilization, and emulsification, may also contribute but were not quantified. Consequently, the capillary-number analysis supports the interpretation that AOS-assisted CEOR reduced capillary trapping during displacement, but it does not support the interpretation that CEOR overcame the capillary confinement of an already trapped residual-oil phase.

No unified capillary number can be associated with the N_2-WAG process because of the existence of three fluid phases, multiple interfaces, gas trapping, and multiple saturation changes. As a reference, the aqueous WAG slug was assigned a flow-based

oil–water capillary number similar to that of the 7600 ppm LSWF case, i.e., 4.81×10^{-8}, because the same brine viscosity, measured oil–water interfacial tension, and liquid superficial velocity were used. Accordingly, the overall N_2-WAG response is interpreted mainly in terms of three-phase saturation history, trapped phase(s), flow reorientation, and displacement cycling.

For completeness, an order-of-magnitude bound was also estimated for the N_2 slugs (Table 13). At 70 °C and approximately 4000 psi, the N_2 viscosity is approximately 0.026 cP [35,36], i.e., approximately 17 times lower than that of the 7600 ppm brine. Because the gas–oil IFT was not measured, a deliberately wide range of 5–25 mN/m was assumed; with the in situ superficial velocity of 2.47×10^{-6} m/s, this gives a flow-based gas–oil capillary number of approximately 2.6×10^{-9} to 1.3×10^{-8}. Thus, both the aqueous and the gas slugs of the N_2-WAG process operated at capillary numbers at least one order of magnitude below the lower limit of the critical range discussed above. The N_2-WAG recovery therefore cannot be attributed to viscous mobilization of capillary-trapped oil; it is interpreted in terms of saturation-history changes, phase redistribution, and gas trapping, as discussed above for the WAG cycles.

5. Conclusions

In the current study, HSWF, low-salinity flooding, AOS-assisted CEOR, and N_2-WAG were compared for their influence on oil displacement and saturation-history dependence in sandstone cores. The obtained data indicate that not only pore architecture, but also brine salinity, surfactant-assisted displacement, and applied saturation history influenced the final displacement response.

Waterflooding with high-salinity brine (56,300 ppm) set the reference displacement scenario, resulting in a mean OOIP recovery of 53.15 ± 5.42% and a mean residual oil saturation of 34.57 ± 2.99% PV. A plateau in recovery with a trend of increasing water cut was consistent with depletion of the connected mobile-oil fraction and formation of the residual-trapping endpoint under forced-imbibition conditions. Waterflooding with low salinities showed a non-monotonic effect, with 7600 ppm as the best-performing salinity among those tested, achieving 61.31 ± 5.69% OOIP recovery and 28.52 ± 3.36% PV residual oil saturation. Further dilution to 3000 ppm and 1000 ppm led to a drop in recovery and an increase in differential pressure. This, together with the associated increase in effluent-solids production and swelling, loss of single-phase brine permeability, and representative micro-CT evidence of pore-space constriction, supports swelling and fines migration as contributing processes.

The best performance among the tested BIO-TERGE® AS-40 concentrations occurred at 0.5 wt% on a commercial-product basis (0.195 wt% active AOS) in a brine of 7600 ppm, where a recovery factor of 69.30 ± 6.32% OOIP was obtained with a residual oil saturation of 22.60 ± 4.00% PV. Individual air–solution surface-tension tests carried out at 70 °C gave a critical micelle concentration (CMC) of 0.044 wt% commercial product (0.017 wt% active AOS), suggesting that all three coreflood concentrations were above the obtained CMC value. Increasing the commercial-product concentration to 1.0 wt% did not provide additional recovery. The oil–water capillary number increased approximately 9.4-fold relative to that of the 7600 ppm LSWF but remained below the level required for substantial mobilization of disconnected residual oil in sandstones; the CEOR benefit is therefore attributed mainly to reduced capillary trapping during the displacement of initially continuous oil.

The highest mean recovery and the lowest mean residual oil saturation were recorded for the N_2-WAG treatment, at 73.06 ± 6.23% OOIP and 19.82 ± 4.01% PV, respectively. Recovery increased through each WAG cycle and the final low-salinity-brine chase, while the stage-wise recovery contribution became progressively smaller. The cyclic differential-

pressure response and recovery trend are consistent with repeated saturation-history changes, gas trapping, flow diversion, and three-phase redistribution during alternating gas–brine injection. However, the higher Cycle 1 recovery was not considered an indication of hysteresis control by itself. An equal-PV comparison indicated a significant early displacement contribution from the initial N_2–brine injection sequence, while N_2 breakthrough indicated gas connectivity to the outlet in Cycle 1. The later cyclic behavior is a result of the cumulative impact of saturation history changes, three-phase redistribution, gas trapping, and flow path modifications. The progressively smaller stage-wise contributions are consistent with the depletion of the hydraulically connected oil and with the approach of the trapped gas saturation to a limiting value over successive cycles.

Additional duplicate coreflood tests performed under the 7600 ppm LSWF and 0.5 wt% AOS-assisted CEOR conditions confirmed reproducible endpoint and pressure behavior under the selected operating conditions, with final-recovery differences of 0.38 and 0.45 percentage points, respectively.

At the common 2.0 PV endpoint, the treatments showed increasing mean recovery and decreasing mean residual oil saturation in the order HSWF, 7600 ppm LSWF, 0.5 wt% AOS-assisted CEOR, and N_2-WAG. This ordering denotes a between-treatment comparison rather than a sequential HSWF–LSWF–CEOR–WAG process. Hence, the key contribution of this research is the between-treatment comparison of different displacement processes within a common core-scale framework in terms of residual trapping and saturation-history effects. Any future research would need to expand on the current confirmations by including drainage–imbibition hysteresis P_cS_w and relative permeability testing for multiple cores under treatments, more reversals in scanning, surfactant retention and phase behavior, gas trapping analysis, further pore-scale visualization, and reservoir-scale modeling.

Author Contributions: Conceptualization, I.A. and B.G.; methodology, I.A., B.G. and N.A.; software, N.A.; validation, I.A., B.G., N.A. and R.S.; formal analysis, N.A. and B.G.; investigation, N.A.; resources, I.A. and B.G.; data curation, N.A.; writing—original draft preparation, N.A.; writing—review and editing, I.A., B.G. and R.S.; visualization, N.A.; supervision, I.A. and B.G.; project administration, I.A. All authors have read and agreed to the published version of the manuscript.

Funding: This research received no external funding.

Data Availability Statement: All data generated or analyzed during this study are included in this published article.

Acknowledgments: The authors gratefully acknowledge the support provided by the laboratory staff for their assistance during the core flooding experiments and data acquisition.

Conflicts of Interest: The authors declare no conflicts of interest.:

Abbreviations

The following abbreviations are used in this manuscript:

AOS	Alpha-olefin sulfonate
API	American Petroleum Institute gravity
BPR	Backpressure regulator
CEOR	Chemical enhanced oil recovery
DI	Deionized
EOR	Enhanced oil recovery
HSWF	High-salinity waterflooding
IFT	Interfacial tension
LSWF	Low-salinity waterflooding
OOIP	Original oil in place
PV	Pore volume

RF	Recovery factor
TDS	Total dissolved solids
WAG	Water-alternating-gas injection
wt%	Weight percent
Bal. IX, Bal. X	Balakhany 9th, Balakhany10th reservoir zone, respectively
Per. B, Per. D	Pereriv B, Pereriv D reservoir zone
CMC	Critical micelle concentration

Nomenclature

Symbol	Definition	Unit
A	Core cross-sectional area	m^2
k	Absolute permeability	m^2 or mD
L	Core length	m
m_d	Dry core mass	g
m_s	Brine-saturated core mass	g
n	Number of experimental units	–
N_c	Capillary number	–
P_{in}	Core inlet pressure	psi
P_{out}	Core outlet pressure	psi
ΔP	Differential pressure across the core	psi
q	Volumetric flow rate	m^3/s or mL/min
q_o	Produced oil flow rate	m^3/s
q_w	Produced water flow rate	m^3/s
RF_i	Recovery factor of core specimen i	% OOIP
$S_{oi,i}$	Initial oil saturation of core specimen i	fraction or % PV
$S_{or,i}$	Final residual oil saturation of core specimen i	fraction or % PV
$S_{w,i,j}$	Water saturation of core specimen i at measurement step j	fraction
$S_{g,i,j}$	Gas saturation of core specimen i at measurement step j	fraction
u	Superficial velocity	m/s
$V_{p,i}$	Pore volume of core specimen i	cm^3 or m^3
$V_{inj,i,j}$	Cumulative injected-fluid volume at measurement step j	cm^3 or m^3
$V_{o,p,i,j}$	Cumulative produced-oil volume at measurement step j	cm^3 or m^3
$OOIP_i$	Original oil in place of core specimen i	cm^3 or m^3
μ_o	Oil viscosity	Pa·s or cP
μ_w	Aqueous-phase viscosity	Pa·s or cP
μ_d	Viscosity of the displacing phase	Pa·s or cP
ρ_b	Brine density	g/cm^3 or kg/m^3
σ	Oil–water interfacial tension	N/m or mN/m
$k_{ro,i,j}$	Normalized oil phase-flow index	–
$k_{rw,i,j}$	Normalized water phase-flow index	–
i	Core-specimen index	–
j	Measurement-step or injected-PV index	–
m	Displacement-treatment index	–
c	WAG-cycle index	–

Appendix A

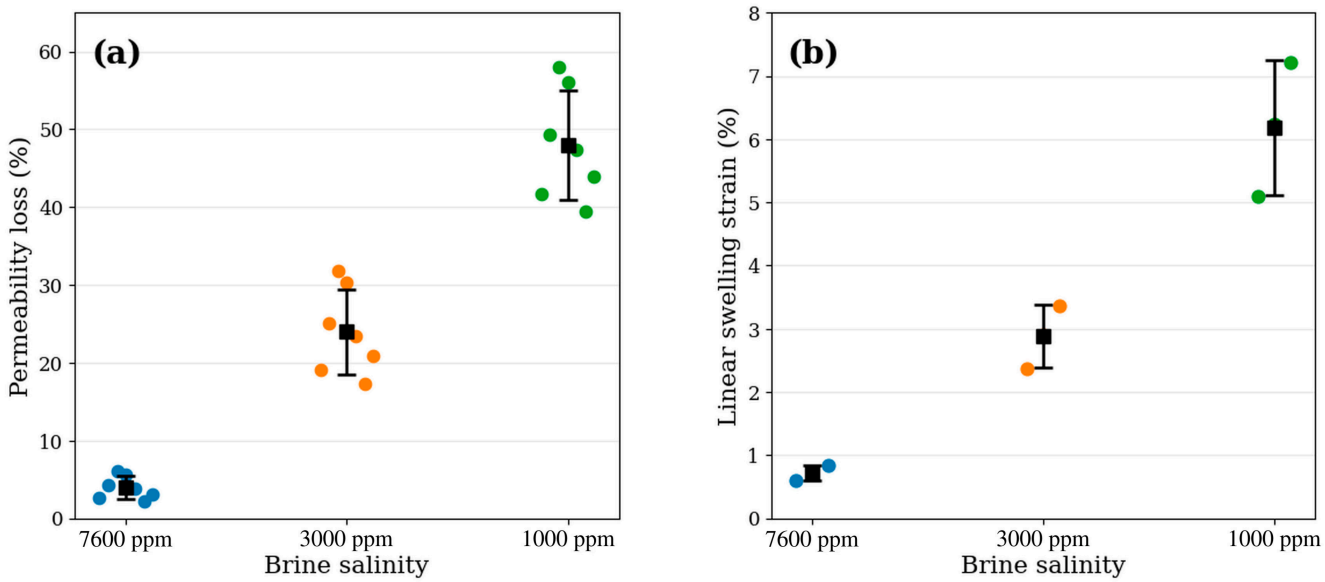


Figure A1. Permeability loss and linear swelling at different brine salinities: (**a**) permeability loss and (**b**) linear swelling strain for 7600, 3000, and 1000 ppm brines.

Colored points represent observations from the experiment, while black points with error bars show the average ± standard deviation for the sample. Permeability loss data are obtained from seven observations for each salinity, but swelling strain data are from three independent observations for each salinity after 24 h at 70 °C.

The vertical dashed line indicates the measured CMC of 0.044 wt% commercial product, equivalent to 0.017 wt% active AOS.

Table A1. Rate sensitivity coreflood results at 0.15, 0.30, and 0.60 mL/min using separately initialized parent-core-matched core specimens.

Core ID	Brine, ppm	Rate, mL/min	Velocity, ft/day	Injected PV	Time, min	ΔP at 2.0 PV, psi	Cum. Oil, cm^3	RF, %OOIP	S_{or}, %PV	Water Cut, %
C1-RS-015	56,300	0.15	0.350	2.0	1770.9	0.62	56.83	56.30	33.21	97.4
C1-RS-030	56,300	0.30	0.699	2.0	885.5	1.21	58.44	57.89	32.00	96.8
C1-RS-060	56,300	0.60	1.399	2.0	442.7	2.37	58.75	58.20	31.77	96.6
C2-RS-015	56,300	0.15	0.350	2.0	1466.1	0.82	40.70	50.70	35.99	98.0
C2-RS-030	56,300	0.30	0.699	2.0	733.1	1.58	41.78	52.05	35.00	97.5
C2-RS-060	56,300	0.60	1.399	2.0	366.5	3.06	42.06	52.40	34.75	97.3
C3-RS-015	56,300	0.15	0.350	2.0	1565.1	1.07	36.34	43.60	40.04	98.5
C3-RS-030	56,300	0.30	0.699	2.0	782.5	2.02	37.56	45.07	39.00	98.0
C3-RS-060	56,300	0.60	1.399	2.0	391.3	3.88	37.84	45.40	38.77	97.8

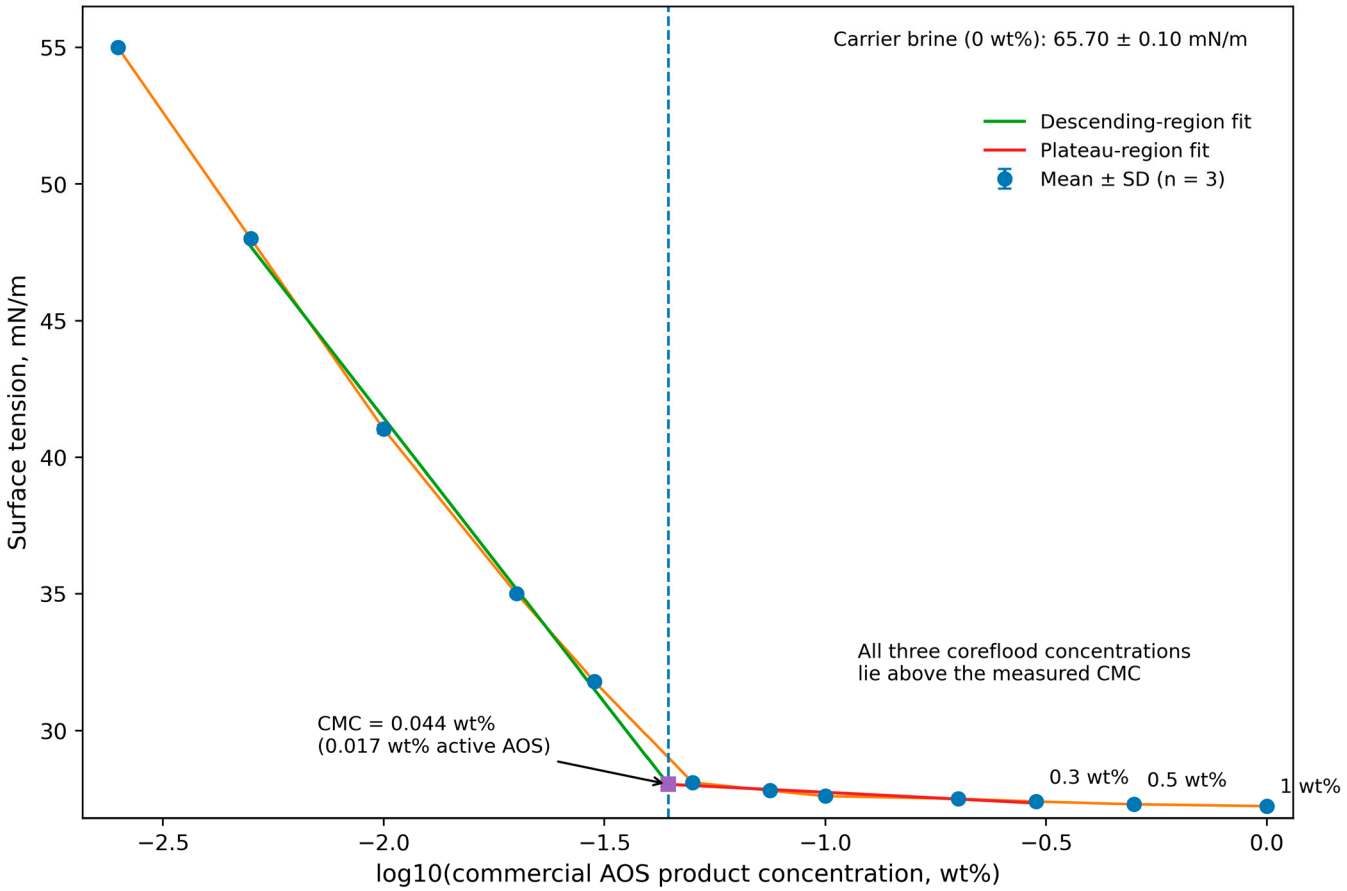


Figure A2. Air–solution surface tension of BIO-TERGE® AS-40 in 7600 ppm brine at 70 °C. The CMC was determined as 0.044 wt% commercial product (0.017 wt% active AOS) from the intersection of the descending and plateau regions; data are shown as mean ± SD (n = 3).

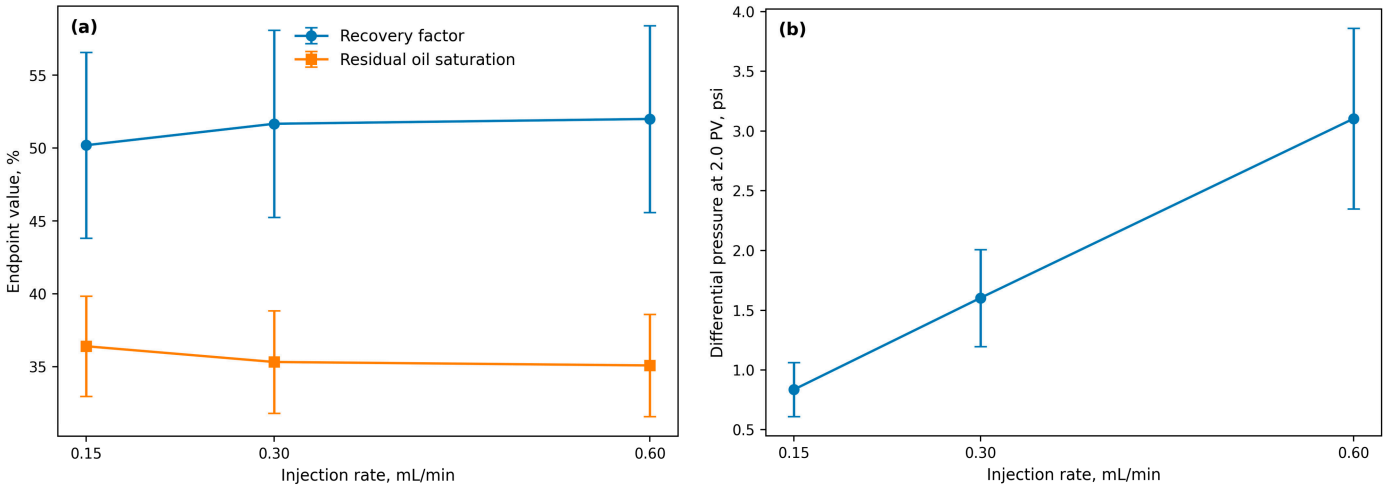


Figure A3. Rate-sensitivity of the HSWF displacement endpoints at 0.15, 0.30, and 0.60 mL/min: (**a**) recovery factor and residual oil saturation and (**b**) differential pressure at 2.0 PV. Data are shown as mean ± SD (n = 3).

Table A2. Summary of direct Pc–Sw hysteresis indicators and complementary contact-angle and oil–water IFT measurements used in the confirmation experiments.

Measurement	Result
Pc separation at Sw = 0.60	1.21 psi
Pc separation at Sw = 0.50	1.22 psi
Pc–Sw loop-area metric, Sw = 0.26–0.82	0.61 psi·Sw
Scanning reversal point	Sw = 0.60; Pc = 0.90 psi
Minimum Sw during scanning drainage	0.43
Scanning re-imbibition endpoint	0.68
Contact angle before Pc cycle	89.5 ± 1.9°
Contact angle after Pc cycle	83.8 ± 1.5°
Mean paired contact-angle change	−5.7 ± 2.9°
HSWF oil–water IFT at 70 °C	24.7 ± 0.2 mN/m
7600 ppm oil–water IFT at 70 °C	22.5 ± 0.2 mN/m
0.5 wt% AOS oil–water IFT at 70 °C	2.65 ± 0.10 mN/m

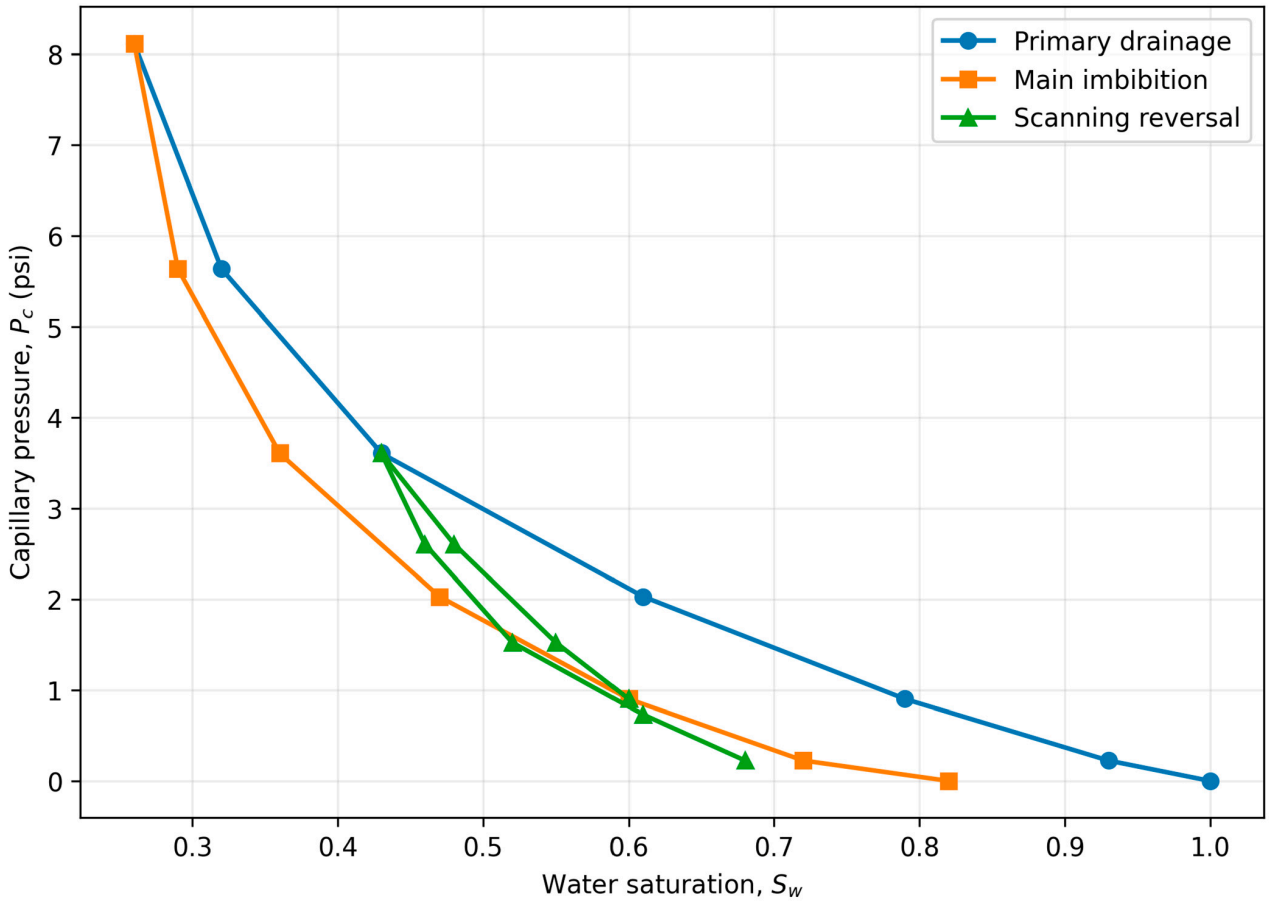


Figure A4. Equilibrium $P_c - S_w$ response of the representative C1-parent-matched sandstone specimen in the 7600 ppm brine–crude-oil system at 70 °C, showing the primary drainage branch, main imbibition branch, and reversal-generated internal scanning path.

Table A3. Measured recovery-factor and differential-pressure histories for the independent duplicate corefloods.

Injected PV	Recovery Factor (% OOIP)				Differential Pressure (psi)			
	LSWF A	LSWF B	AOS A	AOS B	LSWF A	LSWF B	AOS A	AOS B
0.00	0.00	0.00	0.00	0.00	0.00	0.00	0.00	0.00
0.20	28.50	28.80	32.00	32.30	0.58	0.60	0.69	0.71
0.40	47.80	48.10	52.50	52.90	0.91	0.89	1.14	1.17
0.60	57.20	57.50	61.80	62.10	1.00	0.97	1.20	1.23
0.80	61.70	61.90	66.00	66.30	0.93	0.92	1.10	1.12
1.00	63.80	64.00	68.00	68.30	0.86	0.85	0.98	1.00
1.20	64.90	65.20	68.80	69.10	0.80	0.79	0.88	0.90
1.40	65.50	65.80	69.20	69.55	0.75	0.74	0.81	0.83
1.60	65.80	66.10	69.45	69.82	0.71	0.70	0.76	0.78
1.80	66.00	66.30	69.62	70.05	0.68	0.67	0.72	0.74
2.00	66.10	66.48	69.75	70.20	0.66	0.65	0.69	0.70

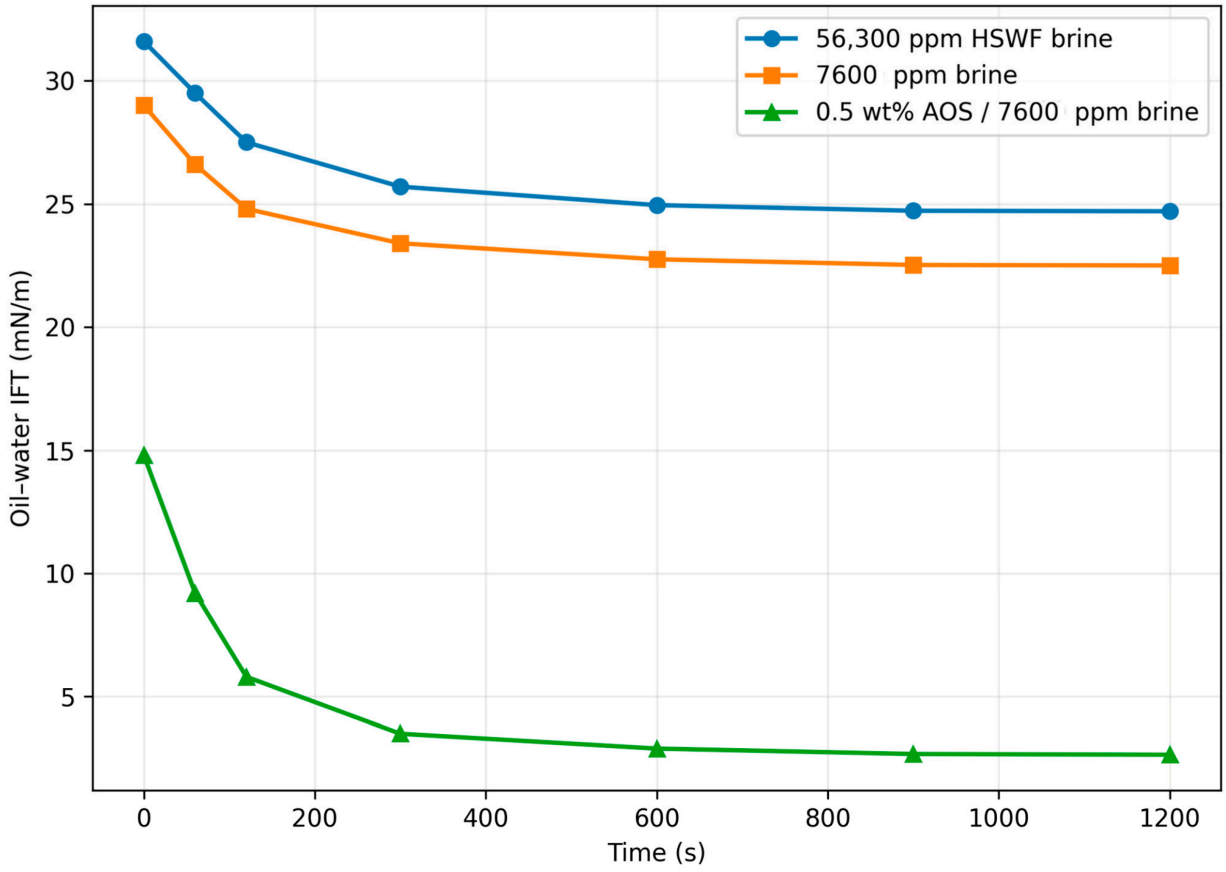


Figure A5. Time-dependent dynamic oil–water interfacial-tension response at 70 °C for crude oil against 56,300 ppm HSWF brine, 7600 ppm brine, and 0.5 wt% AOS in 7600 ppm brine.

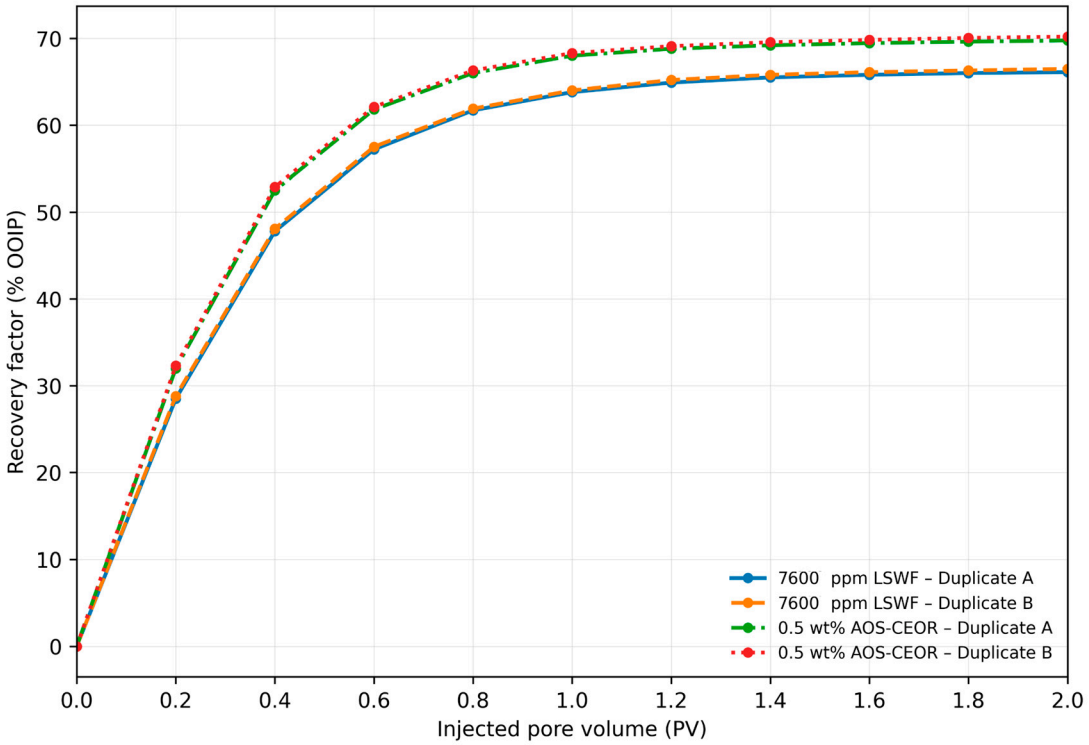


Figure A6. Recovery-factor histories for independent duplicate corefloods conducted under the 7600 ppm LSWF and 0.5 wt% AOS-assisted CEOR conditions. Each duplicate run used a fresh, independently prepared parent-core-matched specimen.

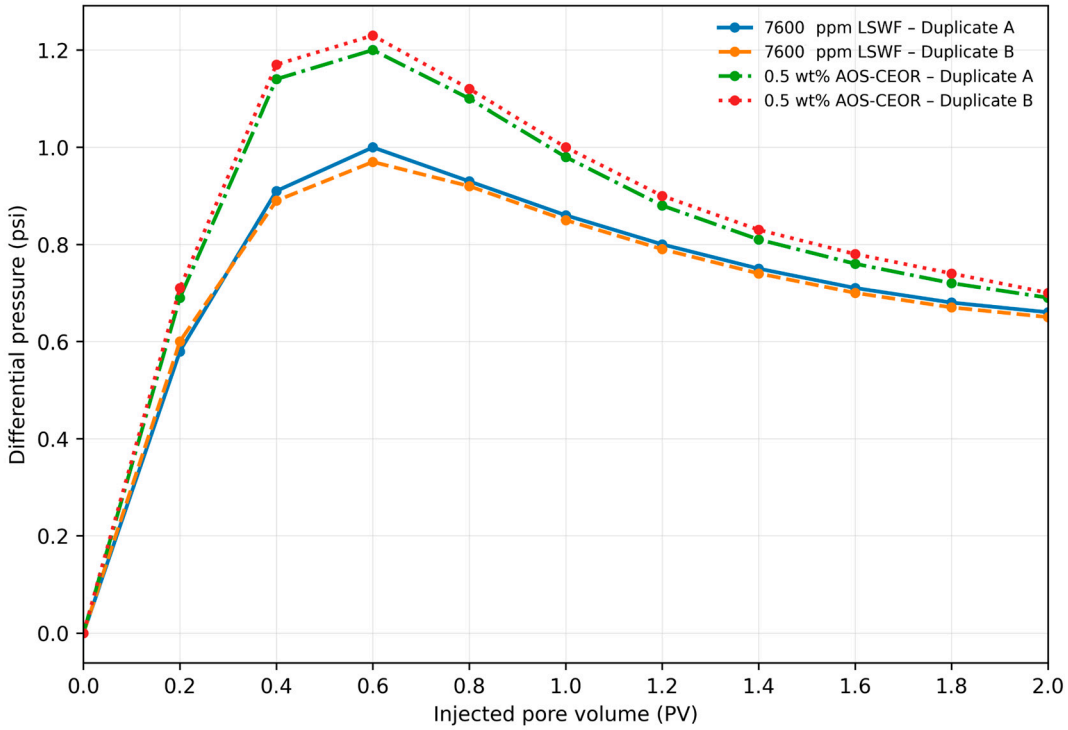


Figure A7. Differential-pressure histories for independent duplicate corefloods conducted under the 7600 ppm LSWF and 0.5 wt% AOS-assisted CEOR conditions.

References

1. Joekar-Niasar, V.; Doster, F.; Armstrong, R.T.; Wildenschild, D.; Celia, M.A. Trapping and hysteresis in two-phase flow in porous media: A pore-network study. *Water Resour. Res.* **2013**, *49*, 4244–4256. [CrossRef]
2. Elhaj, M.A.; Hossain, M.E.; Imtiaz, S.A.; Naterer, G.F. Hysteresis of wettability in porous media: A review. *J. Pet. Explor. Prod. Technol.* **2020**, *10*, 1897–1905. [CrossRef] [PubMed]
3. Lan, Y.; Guo, P.; Liu, Y.; Wang, S.; Cao, S.; Zhang, J.; Sun, W.; Qi, D.; Ji, Q. State of the Art on Relative Permeability Hysteresis in Porous Media: Petroleum Engineering Application. *Appl. Sci.* **2024**, *14*, 4639. [CrossRef]
4. Fatemi, S.M.; Sohrabi, M. Relative permeabilities hysteresis for oil/water, gas/water and gas/oil systems in mixed-wet rocks. *J. Pet. Sci. Eng.* **2018**, *161*, 559–581. [CrossRef]
5. Shahverdi, H.R.; Sohrabi Sedeh, M. An improved three-phase relative permeability and hysteresis model for the simulation of a water-alternating-gas injection. *SPE J.* **2013**, *18*, 841–850. [CrossRef]
6. Afzali, S.; Rezaei, N.; Zendehboudi, S. A comprehensive review on enhanced oil recovery by water alternating gas (WAG) injection. *Fuel* **2018**, *227*, 218–246. [CrossRef]
7. Morrow, N.R.; Buckley, J.S. Improved oil recovery by low-salinity waterflooding. *J. Pet. Technol.* **2011**, *63*, 106–112. [CrossRef]
8. Liu, F.; Wang, M. Review of low salinity waterflooding mechanisms: Wettability alteration and its impact on oil recovery. *Fuel* **2020**, *267*, 117112. [CrossRef]
9. Lyu, C.; Zhong, L.; Ning, Z.; Chen, M.; Cole, D.R. Review on underlying mechanisms of low salinity waterflooding: Comparisons between sandstone and carbonate. *Energy Fuels* **2022**, *36*, 2407–2423. [CrossRef]
10. Nasralla, R.A.; Nasr-El-Din, H.A. Double-layer expansion: Is it a primary mechanism of improved oil recovery by low-salinity waterflooding? *SPE Reserv. Eval. Eng.* **2014**, *17*, 49–59. [CrossRef]
11. Dang, C.; Nghiem, L.; Nguyen, N.; Chen, Z.; Nguyen, Q. Mechanistic modeling of low-salinity water flooding. *J. Pet. Sci. Eng.* **2016**, *146*, 191–209. [CrossRef]
12. Johannessen, A.M.; Spildo, K. Enhanced oil recovery by combining surfactant with low salinity injection. *Energy Fuels* **2013**, *27*, 5738–5749. [CrossRef]
13. Tavassoli, S.; Kazemi, A.; Korrani, N.; Pope, G.A. Low-salinity surfactant flooding—A multimechanistic enhanced-oil-recovery method. *SPE J.* **2016**, *21*, 744–760. [CrossRef]
14. Massarweh, O.; Abushaikha, A.S. The use of surfactants in enhanced oil recovery: A review of recent advances. *Energy Rep.* **2020**, *6*, 3150–3178. [CrossRef]
15. Araz, A.; Kamyabi, F. Experimental study of combined low salinity and surfactant flooding effect on oil recovery. *Oil Gas. Sci. Technol.* **2021**, *76*, 4. [CrossRef]
16. Shakeel, M.; Samanova, A.; Pourafshary, P.; Hashmet, M.R. Optimization of Low Salinity Water/Surfactant Flooding Design for Oil-Wet Carbonate Reservoirs by Introducing a Negative Salinity Gradient. *Energies* **2022**, *15*, 9400. [CrossRef]
17. Li, Q.; Li, Q.; Cao, H.; Wu, J.; Wang, F.; Wang, Y. The Crack Propagation Behaviour of CO_2 Fracturing Fluid in Unconventional Low Permeability Reservoirs: Factor Analysis and Mechanism Revelation. *Processes* **2025**, *13*, 159. [CrossRef]
18. Wang, L.; Zheng, A.; Lu, W.; Shen, T.; Wang, W.; Wei, L.; Chang, Z.; Li, Q. Analysis of Fracturing Expansion Law of Shale Reservoir by Supercritical CO_2 Fracturing and Mechanism Revealing. *Energies* **2024**, *17*, 3865. [CrossRef]
19. Kumar, S.; Mandal, A. A comprehensive review on chemically enhanced water alternating gas/CO2 injection for enhanced oil recovery. *J. Pet. Sci. Eng.* **2017**, *157*, 696–715. [CrossRef]
20. Kong, D.; Gao, Y.; Sarma, H.; Li, Y.; Guo, H.; Zhu, W. Experimental Investigation of Immiscible Water-Alternating-Gas Injection in Ultra-High Water-Cut Stage Reservoir. *Adv. Geo-Energy Res.* **2021**, *5*, 139–152. [CrossRef]
21. Fang, P.; Zhang, Q.; Zhou, C.; Yang, Z.; Yu, H.; Du, M.; Chen, X.; Song, Y.; Wang, S.; Gao, Y.; et al. Chemical-Assisted CO_2 Water-Alternating-Gas Injection for Enhanced Sweep Efficiency in CO_2 EOR. *Molecules* **2024**, *29*, 3978. [CrossRef] [PubMed]
22. Yousef, A.A.; Al-Saleh, S.; Al-Kaabi, A.; Al-Jawfi, M. Laboratory investigation of the impact of injection-water salinity and ionic content on oil recovery from carbonate reservoirs. *SPE Reserv. Eval. Eng.* **2011**, *14*, 578–593. [CrossRef]
23. Villero-Mandon, J.; Askar, N.; Pourafshary, P.; Riazi, M. Importance of Fluid/Fluid Interactions in Enhancing Oil Recovery by Optimizing Low-Salinity Waterflooding in Sandstones. *Energies* **2024**, *17*, 3315. [CrossRef]
24. Seo, K.; Kim, B.; Liu, Q.; Lee, K.S. Simulation of Low-Salinity Water-Alternating Impure CO2 Process for Enhanced Oil Recovery and CO2 Sequestration in Carbonate Reservoirs. *Energies* **2025**, *18*, 1297. [CrossRef]
25. Seong, Y.; Kim, B.; Liu, Q.; Wang, L.; Lee, K.S. Synergistic Effects of Dimethyl Ether and LSW in a CO2 WAG Process for Enhanced Oil Recovery and CO2 Sequestration. *Energies* **2025**, *18*, 6104. [CrossRef]
26. Sarma, H.K.; Awolayo, A.N.; Olayiwola, S.O.; Fakir, S.H.; Belhaj, A.F. Injectivity, Potential Wettability Alteration, and Mineral Dissolution in Low-Salinity Waterflood Applications: The Role of Salinity, Surfactants, Polymers, Nanomaterials, and Mineral Dissolution. *Processes* **2025**, *13*, 2636. [CrossRef]
27. Sarma, H.K.; Awolayo, A.N.; Olayiwola, S.O.; Fakir, S.H.; Belhaj, A.F. Experimental Investigation of Surfactant-Assisted Low-Salinity Brine Flooding in Oil-Wet Carbonate Reservoirs for Enhanced Oil Recovery. *Processes* **2026**, *14*, 1054. [CrossRef]

28. Nuetor, F.D.; Oladele, D.A.; Babalola, F.K.; Boukadi, F.H. Salinity Effects on Surfactant Flooding Performance in Associated Gas Reservoirs: A Simulation-Guided Evaluation of Transport, Adsorption, and Oil Recovery. *Processes* **2026**, *14*, 1851. [CrossRef]
29. Li, Q.; Wang, Y.; Wang, F.; Ning, X.; Chuanbao, Z.; Zhang, J.; Zhang, C. Factor analysis and mechanism disclosure of supercritical CO_2 filtration behavior in tight shale reservoirs. *Environ. Sci. Pollut. Res.* **2022**, *29*, 17682–17694. [CrossRef] [PubMed]
30. Li, Q.; Li, Q.; Wang, F.; Xu, N.; Wang, Y.; Bai, B. Settling behavior and mechanism analysis of kaolinite as a fracture proppant of hydrocarbon reservoirs in CO_2 fracturing fluid. *Colloids Surf. A Physicochem. Eng. Asp.* **2025**, *724*, 137463. [CrossRef]
31. Li, Q.; You, D.; Li, Q.; Wang, F.; Wang, Y.; Yang, Y. Analysis of Sedimentation Behavior and Influencing Factors of Solid Particles in CO_2 Fracturing Fluid. *Processes* **2025**, *13*, 4049. [CrossRef]
32. Li, Q.; Wang, Y.; Wang, F.; Li, Q.; Kobina, F.; Bai, H.; Yuan, L. Effect of a Modified Silicone as a Thickener on Rheology of Liquid CO_2 and Its Fracturing Capacity. *Polymers* **2019**, *11*, 540. [CrossRef] [PubMed]
33. Span, R.; Lemmon, E.W.; Jacobsen, R.T.; Wagner, W.; Yokozeki, A. A Reference Equation of State for the Thermodynamic Properties of Nitrogen for Temperatures from 63.151 to 1000 K and Pressures to 2200 MPa. *J. Phys. Chem. Ref. Data* **2000**, *29*, 1361–1433. [CrossRef]
34. Lemmon, E.W.; Jacobsen, R.T. Viscosity and Thermal Conductivity Equations for Nitrogen, Oxygen, Argon, and Air. *Int. J. Thermophys.* **2004**, *25*, 21–69. [CrossRef]
35. Sohrabi, M.; Tehrani, D.H.; Danesh, A.; Henderson, G.D. Visualization of Oil Recovery by Water-Alternating-Gas Injection Using High-Pressure Micromodels. *SPE J.* **2004**, *9*, 290–301. [CrossRef]
36. Land, C.S. Calculation of Imbibition Relative Permeability for Two- and Three-Phase Flow from Rock Properties. *SPE J.* **1968**, *8*, 149–156. [CrossRef]
37. Guo, H.; Song, K.; Hilfer, R. A Brief Review of Capillary Number and its Use in Capillary Desaturation Curves. *Transp. Porous Media* **2022**, *144*, 3–31. [CrossRef]
38. Chatzis, I.; Morrow, N.R. Correlation of Capillary Number Relationships for Sandstone. *SPE J.* **1984**, *24*, 555–562. [CrossRef]
39. Abeysinghe, K.P.; Fjelde, I.; Lohne, A. Displacement of Oil by Surfactant Flooding in Mixed-Wet Condition. In Proceedings of the International Symposium of the Society of Core Analysts, Aberdeen, UK, 27–30 August 2012. Paper SCA2012-23.

Disclaimer/Publisher's Note: The statements, opinions and data contained in all publications are solely those of the individual author(s) and contributor(s) and not of MDPI and/or the editor(s). MDPI and/or the editor(s) disclaim responsibility for any injury to people or property resulting from any ideas, methods, instructions or products referred to in the content.